UNIVERSITÀ
DEGLI STUDI
FIRENZE

Scuola di
Scienze Matematiche,
Fisiche e Naturali

Corso di laurea in
Scienze Fisiche e
Astrofisiche

Measurement of the Equation of State of superfluid Fermi gases of ^{6}Li atoms.

Misura dell'equazione di stato di gas fermionici superfluidi di atomi di ^{6}Li.

Relatore: Dott. Giacomo Roati

Correlatore: Prof. Massimo Inguscio

Candidato: Andrea Amico

Anno accademico 2013-2014

Contents

Introduction

Ultracold atomic Fermi gases are emerging as an ideal test-bed for many-body theories of strongly correlated fermions, opening a new way to study condensed matter problems with unprecedented clearness and effectiveness [1]. One of the key points is represented by the short-range nature of the inter-particle interactions. In fact, due to the ultra-low temperature, the scattering is purely s-wave and it can be described by an unique parameter, the scattering length a. Close to a Fano-Feshbach resonance, the scattering amplitude between fermions can be tuned at will, allowing the observation of pair condensation and superfluidity in these Fermi systems. This opens up the possibility to explore the so called BEC-BCS crossover, i.e. the transition from a Bose-Einstein condensate (BEC) of tightly bound dimers to a Bardeen-Cooper-Schrieffer (BCS) superfluid of long-range Cooper pairs [1]. The concept of the BEC-BCS crossover was introduced by Leggett in the eighties [2], to connect the two paradigmatic and, at first sight, clearly distinct theories of superfluidity: the Bose-Einstein condensation of weakly interacting bosons and the Bardeen-Cooper-Schrieffer superfluidity of long-range fermionic pairs. The (experimental) study of strongly-interacting fermions across the BEC-BCS crossover is becoming nowadays even more relevant, since Fermi gases in this regime are expected to share several properties with high-Tc superconductors.

Ultracold Fermi gases are not only the coldest strongly-correlated matter in the universe but they are also much thinner than the air we breath, with typical densities n of the order of 10^{13} atoms/cm^3. This affects deeply the thermodynamics of the system that depends essentially on three length scales, the mean inter-particle distance $n^{-1/3}$, the de Broglie wavelength λ_{dB}, and the scattering length a. The energy scales associated to these three quantities are then the Fermi energy E_F, the thermal energy k_BT (being k_B the Boltzmann constant), and finally the bound state energy $E_b \sim a^{-2}$. For example, the pressure n for a homogeneous gas can be written as $P = P(n, T, a)$ that, by using just dimensional analysis becomes:

$$P = \frac{2}{5} n E_F \times F\left(\frac{T}{T_F}, \frac{1}{k_F a}\right), \tag{1}$$

where T_F and k_F are the Fermi temperature and the Fermi wavevector, respectively, and F is a universal function. The same kind of relation holds for all other thermodynamic quantities. Right on top of the Fano-Feshbach resonance, the scattering length diverges, meaning that the interactions reach the maximum value allowed

by quantum mechanics (unitary regime). In this case, the system enters a region of even larger degree of universality. In fact, here the system loses completely the dependence on the scattering length, and the thermodynamics of this *unitary* Fermi gas can be described only by $n^{-1/3}$ and λ_{dB}. This means that we can write dimensionless quantities such as P/P_0, E/E_0 (where the 0 subscript indicates the corresponding ideal Fermi gas quantity) that will be linked in an universal way to T/T_F, or equivalently to the phase-space density $n\lambda_{dB}^3$. Any dimensionless thermodynamic quantities must depend universally on any other similar ones, i.e. the thermodynamics of the unitary Fermi gas becomes universal! Another consequence is that, quite remarkably (and also surprisingly), the thermodynamic quantities (pressure, energy, entropy...) of such strongly-correlated fermionic system are proportional to those of a non-interacting gas, with the proportionality factor given by a universal function of T/T_F. In the unitary regime the equation of state (EoS) becomes particularly simple, and it connects quantities that can be experimentally measured, such as the atomic density and eventually the temperature. The universal regime is not peculiar of ultracold Fermi gases with resonant interactions. For instance, neutron matter is characterised by a scattering length between neutrons much larger that the mean inter-neutron distance (18.6 fm versus 1 fm). The same behaviour in the thermodynamics is then expected, connecting together a supercold cloud of fermionic atoms trapped in a ultra-high vacuum cell with the crust of a neutron star!

The knowledge of the EoS is particularly important: it quantitatively describes the key properties of the systems, revealing the presence of phase-transitions (for example to a superfluid regime). Signatures of superfluidity in strongly-correlated atomic fermionic systems have been provided so far only by the observation of vortices, or through the study of the dynamics through obstacles [1]. The measurement of the EoS is an elegant and direct measurement of such an intriguing phase-transition, connecting even more the physics of degenerate atomic gases to the one of ordinary materials (Helium or superconductors).

The work of this thesis fits exactly in this context, reporting on the experimental measurement of the equation of state of a unitary Fermi gas of ^{6}Li atoms. The EoS has been extracted from the analysis of the in-situ density profiles of the fermionic clouds. My thesis includes both an experimental (design and implementation of optical set-ups and data acquisition) and a more computational part (code writing and data analysis). In more details, my work has been focussed in the following 4 main topics:

- I have developed a Matlab code to perform the Abel deconvolution technique to reconstruct the 3D density profiles of a strongly Fermi gas. Together with the local density approximation (LDA), these are the key ingredient to extract the equation of state of the system. I have verified the correct working of the code by implementing it on artificial density profiles.

- I have built and successively characterised the absorption imaging set-up to obtain the experimental density profiles of the cloud. In particular, I have de-

signed and realised a compact optical system with the best operative conditions (magnification, intensity, focussing) to obtain clear, reliable and not-diffracted in-situ images of the atoms (optical resolution of about 1.5μm). I have also placed on the experimental set-up the new ultra-sensitive EMCCD camera, adapting the pre-existing acquisition program to our purposes.

- I have participated to the production of the unitary Fermi gases in the laboratory, finding the optimum parameters to get the data (images of the cloud) that I have then analysed with my code.

- I have measured the EoS of the unitary Fermi gas, revealing the transition to the superfluid regime, both in the compressibility and in the specific heat, C_V. In the high temperature regime ($T/T_F \geq 1$) the measured value of C_V approaches the classical limit $3/2Nk_B$ while, lowering the temperature and approaching $T_C/T_F \sim 0.14$, I have observed a clear peak in C_V for $T = T_C$. This feature is the characteristic evidence of a second order phase transition, the analogous of the famous λ transition observed both in bosonic superfluids (^{4}He) and in superconductors. I have determined the critical temperature T_C/T_F directly from the analysis of the density profiles using the code I have developed. The value I have found (T_C/T_F=0.14 (3)) is in good agreement with recent measurements [3][4][5] and with Monte Carlo calculations [6][7][8]. In the high temperature regime ($T/T_F \geq 1$), I have also fitted the density profiles with the virial expansion, obtaining the temperature of the strongly interacting "normal" gas. I have extracted the sign and the modulus of the b_4 virial coefficient: also in this case, the estimated value of b_4 is in qualitative agreement with the one available in literature [3][5][9]. I want to stress that this analysis is particularly relevant, since in our system it is the only way to determine the temperature of the gas due to the strong interactions, that do not allow the standard momentum distribution analysis.

This thesis is divided in 5 Chapters:

1. In Chapter 1, I introduce the basic concepts of the thermodynamics of the ideal Fermi gas: these results are used in the rest of the thesis to validate our experimental procedure to extract the equation of state of a superfluid Fermi gas. Then, I present the main results of the scattering theory in the case of ultracold atoms. I show how the inter-particle interactions can be experimentally tuned via Fano-Feshbach resonances, allowing the study of the so-called BEC-BCS crossover, where the thermodynamics of the system becomes "universal" . At the end of the chapter, I show how, in this limit, the thermodynamics relations are connected by universal functions.

2. In Chapter 2, I link the thermodynamic quantities to the atomic density profiles and the trapping potential. In particular, I introduce the concept of local

density approximation, fundamental to relate the physics of trapped atoms to the one of many homogeneous systems. I also describe the Abel deconvolution method used to reconstruct the 3D density profiles from the 2D integrate images that are typically obtained in the experiments.

3. In Chapter 3, I describe the experimental apparatus to produce superfluid gases of ^{6}Li atoms, focussing on the imaging set-up and on the description of the trapping potentials.

4. In Chapter 4, I first present the results on the equation of state for a non-interacting, ideal gas of ^{6}Li atoms. The second part of this Chapter is instead dedicated to the study of the strongly interacting gas. In the high temperature limit ($T/T_F \geq 1$) I make use of the virial expansion to obtain the temperature of the gas. In the last part, I discuss the main achievements of this work, i.e. the measurement of the equation of state of the unitary superfluid Fermi gas.

5. In Chapter 5, I discuss about the possible sources of errors (statistical and systematic) that may affect our measurements.

Chapter 1

Theory

We first present some basic concepts of the thermodynamics of the ideal Fermi gas. These textbook results will be used in the rest of the thesis to validate our experimental procedure to extract the equation of state of a superfluid Fermi gas. We continue this chapter by describing the scattering problem in the case of dilute ultracold atomic systems. In particular, we will see how the inter-particle interactions can be experimentally tuned via Fano-Feshbach resonances. The possibility of controlling the scattering properties between ultracold fermions allows the investigation of the so called BEC-BCS crossover, i.e. the continuous transition between tightly bound bosonic molecules (BEC limit) to generalised Cooper-like pairs of fermions. We describe the crossover region (where the scattering length "diverges"), also called unitary regime, where the thermodynamics of the system becomes "universal" since the only remaining length scale is the mean inter-particle distance. At the end we will show how, in this limit, the thermodynamics relations are connected by universal functions.

1.1 Thermodynamics

Classical particles are distinguishable, since, at least in principle, one can follow their trajectories in a continuous way. This statement does not hold in quantum mechanics, where particles are instead described by wavefunctions. When the wavefunctions of two identical particles overlap, the possibility of labelling individually the particles is lost. This loss of information at the microscopic level affects deeply both statistical and thermodynamic properties of a macroscopic system. In this section, we describe the specific case of non-interacting Fermi gases. We derive the grand-canonical partition function obtaining some thermodynamic quantities like pressure and internal energy in the low-temperature limit. We will show how these quantities are combined in an equation of state (EoS) that fully describes the (equilibrium) properties of the system.

1.1.1 Ideal gas

Consider an ensemble of identical particles. Each particle has the same energy spectrum. We call k the collection of quantum number that univocally define the state of the system. If $|k\rangle$ is an eigenvector of energy, we call ε_k its eigenvalue.

Working with canonical ensemble, i.e. fixed number of particles N, in thermal equilibrium with a heat bath, at some fixed temperature T, we write the partition function as [10]:

$$\mathcal{Z}_N = \sum_{\{n_k\}} \exp\big(-\beta \sum_k n_k \varepsilon_k\big) = \sum_{n_k} \exp\big(-\beta \sum_k n_k \varepsilon_k\big) \delta(N - \sum_k n_k), \tag{1.1}$$

where n_k is the occupation number of a given state $|k\rangle$, $\beta = 1/k_B T$ and k_B is the Boltzmann constant. The summation over $\{n_k\}$ means that one has to sum over all possible collection of state n_k, within the condition that the total number of particle in N. Because of this, is very hard to develop further this equation. What one can do to simplify the problem is freeing the condition of fixed number of particle and work in the grand canonical ensemble instead:

$$\mathcal{Z}_{GC} = \sum_N e^{\beta\mu N} \mathcal{Z}_N \tag{1.2}$$

$$= \sum_N e^{\beta\mu N} \sum_{n_k} \exp\left[-\beta \sum_k n_k \varepsilon_k\right] \delta(N - \sum_k n_k) \tag{1.3}$$

$$= \sum_{\{n_k\}} \exp\left[-\beta \sum_k (\varepsilon_k - \mu) n_k\right] \tag{1.4}$$

$$= \prod_k \sum_{n_k} \exp\left[-\beta \sum_k (\varepsilon_k - \mu) n_k\right] = \prod_k \xi_k, \tag{1.5}$$

where

$$\xi_k = \sum_{n_k} e^{-\beta(\varepsilon_k - \mu) n_k} \tag{1.6}$$

and μ is the chemical potential. We can now explicitly evaluate ξ_k paying attention to the quantum nature of the particle one is dealing with. Bosons have symmetrical wavefunction under exchange, therefore, n_k can take any value. Fermions, on the other hand, have anti-symmetrical wavefunction and, as a consequence, two identical fermions cannot exist in the same state $|k\rangle$. This is the so called Pauli exclusion principle. For this reason, n_k can only assume value 0 or 1. Having this in mind we evaluate the sum separately for fermions and bosons:

$$\xi_k^F = 1 + e^{-\beta(\varepsilon_k - \mu)} \tag{1.7}$$

$$\xi_k^B = \sum_{n_k=1}^{\infty} e^{-\beta(\varepsilon_k - \mu) n_k} = \frac{1}{1 - e^{-\beta(\varepsilon_k - \mu)}}, \tag{1.8}$$

where, in the last passage, we impose $(\varepsilon_k - \mu) > 0$. At this point the grand potential can be written explicitly in the form:

$$\Omega^{F,B} = -\, k_B T \log(\mathcal{Z}_{GC}^{F,B}) = -k_B T \sum_k \log(\xi_k^{F,B}) \tag{1.9}$$

$$= \mp \frac{1}{\beta} \sum_k \log(1 \pm e^{-\beta(\varepsilon_k - \mu)}), \tag{1.10}$$

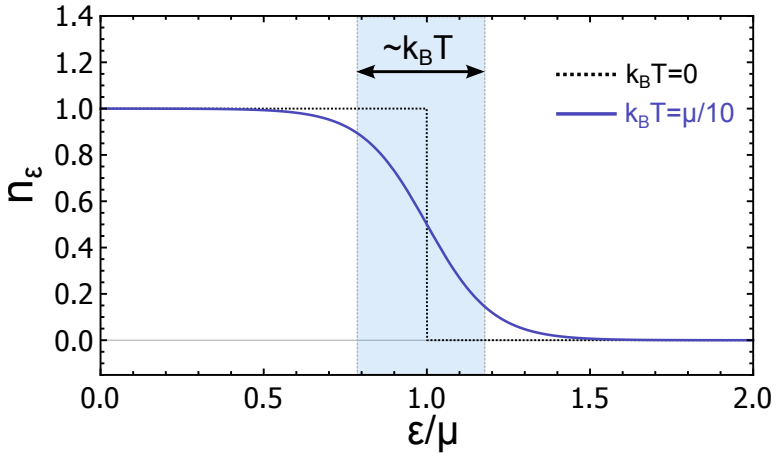

Figure 1.1: *Mean occupation number of the state $|k\rangle$ corresponding to the energy ε_k, given by the Fermi statistics. The blue solid line corresponds to a temperature of $T = \mu/(10k_B)$. The black dashed line corresponds to the zero temperature limit.*

In the same way we calculate the mean occupation number of the state $|k\rangle$:

$$\left\langle n_k^{F,B} \right\rangle = \frac{1}{e^{\beta(\varepsilon_k - \mu)} \pm 1}. \tag{1.11}$$

We notice that, while for bosons $\langle n \rangle$ can assume, in principle, any value, for fermions can only span from 0 to 1, since the denominator is always > 1. This is again the manifestation of the Pauli principle. In the limit of high temperature ($k_B T \gg E_F$) one find the classical Maxwell-Boltzmann distribution.

Free particles

If we consider the case of free particles, we can describe them using plane wave wavefunctions: $\exp(-i\vec{q}\cdot\vec{x})$. The system is than well described by the set of quantum number k:

$$k \to (q_x, q_y, q_z, m_s), \tag{1.12}$$

where q_i is the impulse along $\hat{i}$ and m_s is the projection of the spin along $\hat{z}$. The dispersion law for non-relativistic free particle is simply quadratic:

$$\varepsilon_k = \frac{\hbar^2}{2m} q^2, \tag{1.13}$$

where m is the mass of the particle and $q^2 = q_x^2 + q_y^2 + q_z^2$.

We now proceed with the quantization of momentum considering those particles to be in a box of side L_x, L_y, L_z with periodic boundary conditions:

$$q_i = \frac{2\pi}{L_i} n_i, \tag{1.14}$$

where n_i is an integer number. The free particle case is found again considering the limit of $L_i \to \infty$, although, this wont be a problem since the result we will find wont depends on the quantization volume any more. We have now all the tools we need to write down the grand-potential function for this system:

$$\Omega^{F,B} = \sum_{m_s} \sum_{q_x,q_y,q_z} \mp \frac{1}{\beta} \log(1 \pm e^{-\beta(\varepsilon_k - \mu)}). \tag{1.15}$$

It is very useful to replace the sum over quantized momentum into an integral and, using the dispersion law (1.13) we chose the energy to be the integration variable:

$$\Omega^{F,B} = \sum_{m_s} \frac{V}{8\pi^3} \int d^3q \left[\mp \frac{1}{\beta} \log(1 \pm e^{-\beta(\varepsilon_k - \mu)}) \right] \tag{1.16}$$

$$= \int d\varepsilon \rho(\varepsilon) \left[\mp \frac{1}{\beta} \log(1 \pm e^{-\beta(\varepsilon - \mu)}) \right] \tag{1.17}$$

where $V = L_x \times L_y \times L_z$ is the volume of the box. The criterion for the integral to be an accurate approximation with respect to the sum of discrete states is the following:

$$k_B T \gg \frac{\hbar^2}{2m} \left(\frac{2\pi}{L} \right)^2. \tag{1.18}$$

Physically it means that the energy distance between states has to be small compared to single particle energy fluctuation.

In equation 1.17 we also introduce the density of states ρ which, in three dimensions and in the case of the quadratic dispersion law, assumes the value:

$$\rho(\varepsilon) = \frac{g_s V}{\sqrt{2}\pi^2} \frac{m^{3/2}}{\hbar^3} \sqrt{\varepsilon}, \tag{1.19}$$

where $g_s = 2s + 1$ is the spin degeneracy of energy levels. Using explicitly the expression for the density of state into equation 1.17, we link the grand potential function to internal energy of the system E:

$$\Omega = \mp \frac{g_s V m^{3/2}}{\sqrt{2}\pi^2 \hbar^3} \frac{1}{\beta} \int_0^\infty d\varepsilon \sqrt{\varepsilon} \log(1 \pm e^{\beta(\mu - \varepsilon)}) \quad \text{[integration by parts]} \tag{1.20}$$

$$= -\frac{3}{2} \frac{g_s V m^{3/2}}{\sqrt{2}\pi^2 \hbar^3} \int_0^\infty d\varepsilon \frac{\varepsilon \sqrt{\varepsilon}}{e^{\beta(\varepsilon - \mu)} \pm 1} \tag{1.21}$$

$$= -\frac{2}{3} \int_0^\infty d\varepsilon \rho(\varepsilon) \varepsilon \frac{1}{e^{\beta(\varepsilon - \mu)} \pm 1} = -\frac{2}{3} E. \tag{1.22}$$

Since pressure is linked to grand potential by the relation,

$$P = -\left(\frac{\partial \Omega}{\partial V}\right)_{T,\mu}, \tag{1.23}$$

we can express the pressure as:

$$PV = \frac{2}{3}E \tag{1.24}$$

It is interesting to notice that this result holds for all kind of ideal gases, being them composed by fermions, bosons or even classical particles.

Classical limit

In the classical limit, or high temperature limit, a particle occupies an energy state independently from other particles. This condition is satisfied when:

$$\langle n_k \rangle = \frac{1}{e^{\beta(\varepsilon_k - \mu)} \pm 1} \ll 1 \quad \forall k \tag{1.25}$$

Within this limit we can calculate the density n of the system:

$$n = \frac{N}{V} = \frac{g_s m^{3/2}}{\sqrt{2}\pi^2\hbar^3} \int_0^\infty d\varepsilon \sqrt{\varepsilon} e^{-\beta(\varepsilon-\mu)} \tag{1.26}$$

$$= g_s \left(\frac{m k_B T}{2\pi}\right)^{3/2} \frac{1}{\hbar^3} e^{\beta\mu} = \frac{g_s e^{\beta\mu}}{\lambda_{dB}^3}, \tag{1.27}$$

where we introduced de Broglie wavelength $\lambda_{dB} \equiv \hbar\sqrt{2\pi/m k_B T}$, which represents how much a particle is delocalized in space, i.e. the spread of its wavefunction.

In conclusion, we can talk about classical regime when the thermal spread of the wavefunction, λ_{dB}, is much shorter than the mean inter-atomic distances. This means that the overlap between the wavefunctions of different particles is negligible and the atoms return to behave like distinguishable particles.

$$\lambda_{dB}^3 \ll \frac{1}{n}. \tag{1.28}$$

Quantum limit

The opposite limit is called quantum limit and it is reached when the spread of the wavefunctions is comparable with the inter atomic distances:

$$n\lambda_{dB}^3 \sim 1 \tag{1.29}$$

In those conditions of density and temperature, essentially all elements are solids. The only exceptions are helium, which is liquid, and hydrogen in a particular spin

polarised state. If this is true how can we talk about quantum gas? A possible answer to this question is considering a system out of equilibrium, at very low densities, in the so called dilute regime ($n < 10^{15}\text{cm}^{-3}$). Working out of equilibrium means that the gas will, in a certain amount of time, eventually become a solid. In order to practically perform experiments on such a gas we need the time scale of solidification to be much longer than the experiment time scale, usually given by thermalisation. Fortunately, while thermalisation process only requires two body collisions, solidification, because of the conservation of energy and momentum, works mostly trough three body recombination process. Since the rate of the first is proportional to the density of the gas, n, and the rate of the latter is proportional to the square of the density, n^2, at low enough density the lifetime of a quantum gas is extended (metastable system) and we can actually performs experiment on it [11].

1.1.2 Fermi gas

Since in our experiment we use fermionic ^{6}Li atoms from now on we will focus our attention on the Fermi statistics.

In the limit of zero temperature, the physics of a Fermi gas is dominated by Pauli exclusion principle. The particles occupy the lowest allowed energy levels, filling all the levels from the lowest one, up to zero temperature chemical potential μ_0, also called Fermi energy E_F. In the momentum space the particles fill a sphere of radius p_F, the Fermi momentum. The surface of this sphere is called the Fermi sphere.

The mean occupation number of the system is evaluated taking the limits of $T \to 0$ in equation 1.11:

$$\langle n_\varepsilon \rangle_{T\to 0} = \begin{cases} 0, & \text{if } \varepsilon > \mu \\ 1, & \text{if } \varepsilon < \mu \end{cases} \tag{1.30}$$

Using this result we evaluate the Fermi energy, E_F, for a gas of N particles, in a volume V.

$$\frac{N}{V} = \int_0^\infty d\varepsilon \rho(\varepsilon) n(\varepsilon) \overset{T\to 0}{=} \frac{g m^{3/2}}{\sqrt{2}\pi^2\hbar^3} \int_0^{E_F} d\varepsilon \sqrt{\varepsilon}, \tag{1.31}$$

from this, one obtains the explicit value of E_F:

$$E_F = \frac{\hbar^2}{2m} \left(\frac{6\pi^2}{g_s} \frac{N}{V} \right)^{2/3}. \tag{1.32}$$

We can also calculate the mean energy per particle:

$$\epsilon_0 = \frac{E_0}{V} = \frac{g m^{3/2}}{\sqrt{2}\pi^2\hbar^3} \int_0^{E_F} d\varepsilon \sqrt{\varepsilon}\,\varepsilon = \frac{3}{5} E_F \tag{1.33}$$

Low temperature expansion

In order to evaluate the thermodynamic properties of a Fermi gas at low temperature, one can basically follow two paths. The first consists in using numerical

methods to integrate the equation 1.20, while the second makes use of the Sommerfeld expansion [12]. We describe here the second approach, while we postpone the numerical one in the section 1.5.2.

The idea behind the Sommerfeld expansion lies in the fact that, at low temperature, interesting physics takes place mostly in a small region of energy near E_F due to the Pauli blocking. This allows to obtain an approximated solution of integrals like (1.20) as an expansion in T. We can obtain, for example, an explicit expression for internal energy [10]:

$$E = \frac{3}{5} N E_F \left[1 + \frac{5}{12} \pi^2 \left(\frac{k_B T}{E_F} \right)^2 + \dots \right] \tag{1.34}$$

From 1.24 we calculate the equation of state of a non interacting Fermi gas in the form:

$$P = \frac{2}{3} \frac{E}{V} = \frac{2}{5} \frac{N E_F}{V} \left[1 + \frac{5}{12} \pi^2 \left(\frac{k_B T}{E_F} \right)^2 + \dots \right], \tag{1.35}$$

where P is the pressure. Since we can experimentally produce a gas of non interacting (chapter 3), this relation can be used in order to to check and tune the experimental procedure in a simple case.

1.2 Interacting gas

Many interesting and intriguing phenomena such as superfluity and superconductivity are due to interactions between particles. In cold atomic systems the average density is million times lower than air. Due to this diluteness, most of the scattering properties can be described by two-body collisions and by a single parameter, the scattering length a.

In the following we summarise the main results of the scattering theory.

1.2.1 Introduction to the scattering problem

In non relativistic quantum physics the time evolution of a generic state vector $|\Psi(t)\rangle$ is described by the Schrödinger's equation:

$$i\hbar \frac{\partial}{\partial t} |\Psi(t)\rangle = H |\Psi(t)\rangle , \tag{1.36}$$

where H is the hamiltonian of the system. We can properly talk about scattering when the energy of the system is positive. In order to describe a scattering state one usually use a superposition of stationary states of the hamiltonian, since, if the range of the potential is finite, outside of the interaction area, those states are simply free-particle states.

Lippmann Schwinger equation

Let's consider the case of a particle of mass m scattering from a potential V[1]. We can write the total hamiltonian of this system as a sum of the free-particle hamiltonian $H_0 = p^2/(2m)$ and the interaction potential: $H = H_0 + V$. Let's call $|\Phi\rangle$ a generic eigenvector of H_0:

$$H_0 |\Phi\rangle = E |\Phi\rangle \tag{1.37}$$

In order to find the stationary states of the entire system we need to solve the equation

$$(H_0 + V) |\Psi\rangle = E |\Psi\rangle , \tag{1.38}$$

keeping in mind that $|\Psi(t)\rangle \to |\Phi(t)\rangle$ in the limit of vanishing potential $V \to 0$. The solution is the Lippmann-Schwinger [13] equation:

$$\left|\Psi^{\pm}\right\rangle = |\Phi\rangle + \frac{1}{E - H_0 \pm i\epsilon} V \left|\Psi^{\pm}\right\rangle . \tag{1.39}$$

In the coordinate space, discarding the unphysical solution of incoming waves $\Psi(\mathbf{r})^-$ and working in the asymptotic limit[2], this equation can be rewritten as [14]:

$$\Psi(\mathbf{r})^+ = \frac{1}{(2\pi)^{3/2}} \left[e^{i\mathbf{k}\cdot\mathbf{r}} + f(\mathbf{k}, \mathbf{k}') \frac{e^{ikr}}{r} \right] , \tag{1.40}$$

where $\mathbf{k}$ is the initial wave vector, $\mathbf{k}'$ the scattered one and $f(\mathbf{k}, \mathbf{k}')$ is the scattering amplitude:

$$f(\mathbf{k}, \mathbf{k}') \equiv -\frac{(2\pi)^2 m}{\hbar^2} \int d\mathbf{r}' \frac{e^{i\mathbf{k}'\cdot\mathbf{r}'}}{(2\pi)^{3/2}} V(\mathbf{r}) \Psi(\mathbf{r}) \tag{1.41}$$

The scattering amplitude is linked to the differential scattering cross section by the relation:

$$\boxed{\frac{d\sigma}{d\Omega} = |f(\mathbf{k}, \mathbf{k}')|^2}, \tag{1.42}$$

where Ω is the solid angle. If we consider only elastic scattering, i.e. the internal energy levels remain unchanged after the collision, the wavevector of the incoming and scattered wavefunctions must have the same module: $|\mathbf{k}| = |\mathbf{k}'|$. The scattering amplitude can be written as a function of the scattering angles θ, ϕ and of wavevector module $k = |\mathbf{k}|$. In the case of ultracold atoms we will show that the inter-atomic interaction potential is also spherically symmetric, $V(\mathbf{r}) = V(r)$, therefore, the scattering amplitude must not depend also, on the azimuthal angle ϕ.

$$\boxed{f(\mathbf{k}, \mathbf{k}') \overset{\text{elastic scattering}}{\to} f(k, \theta, \phi) \overset{\text{central potential}}{\to} f(k, \theta).} \tag{1.43}$$

[1] Note that the mathematical description of such a system is actually equivalent to the one of two colliding particle, working in the centre of mass framework, where m is the reduced mass $m = m_1 m_2/(m_1 + m_2)$ and V is the interaction potential.

[2] We write the wave function $\Psi(\mathbf{r})$ far away from the scattering region, where the actual scattering process is finished.

Identical particles

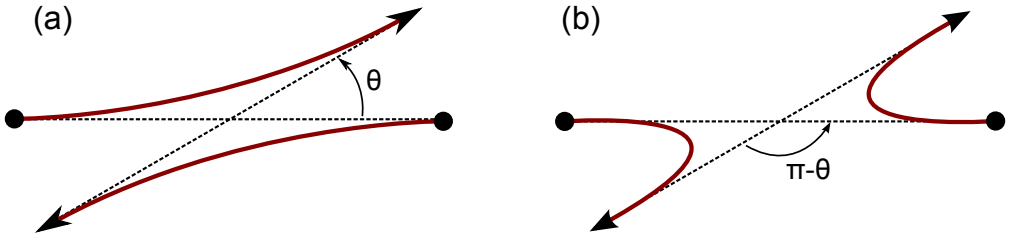

Figure 1.2: *When two identical particles collide one can not distinguish the case (a) from the case (b). Therefore, in order to calculate the scattering amplitude, one has to consider the interference between these two possibilities.*

if we consider identical particles, in the same internal state, the collision process corresponding to scattering amplitudes $f(k,\theta)$ and $f(k,\pi-\theta)$ cannot be distinguish. Because of this, one should consider the quantum statistics of the particle in order to describes correctly the scattering process [14]:

$$f(k,\theta) \overset{\text{identical particle}}{\rightarrow} f(k,\theta) \pm f(k,\pi-\theta), \tag{1.44}$$

where the angle θ is restricted to the interval $0 \leq \theta \leq \pi/2$ and the sign is determined by statistics: " $+$ " for bosons and " $-$ " for fermions. Keeping this in mind the differential cross section turns out to be:

$$\frac{d\sigma}{d\Omega} = |f(k,\theta) \pm f(k,\pi-\theta)|^2. \tag{1.45}$$

1.2.2 Scattering in ultra-cold atoms

Dilute ultracold gas limits

We now consider the case we are most interested in, the scattering properties of a trapped ultracold gas. Neglecting the dipolar interaction[3], the inter-atomic interaction is essentially described by the Lennard-Jones potential:

$$V(r) = \frac{A}{r^{12}} - \frac{B}{r^6}, \tag{1.46}$$

where the first term is used to approximate the short range repulsion and the second describes the van der Waals force due to mutual interaction between fluctuation induced dipoles of the atoms. We state that this kind of interaction is short-ranged,

[3]This kind of interaction can't be neglected in the case of atoms with half empty shells like Chromium ($\mu \simeq 6\mu_B$) or Erbium ($\mu \simeq 7\mu_B$). On the contrary, in commonly used alkali atoms, the dipole moment is $\mu \simeq \mu_B$. Considering that interaction strength is proportional to μ^2, this effect is 36 times smaller then the one present in Er or Cr and can be completely neglected.

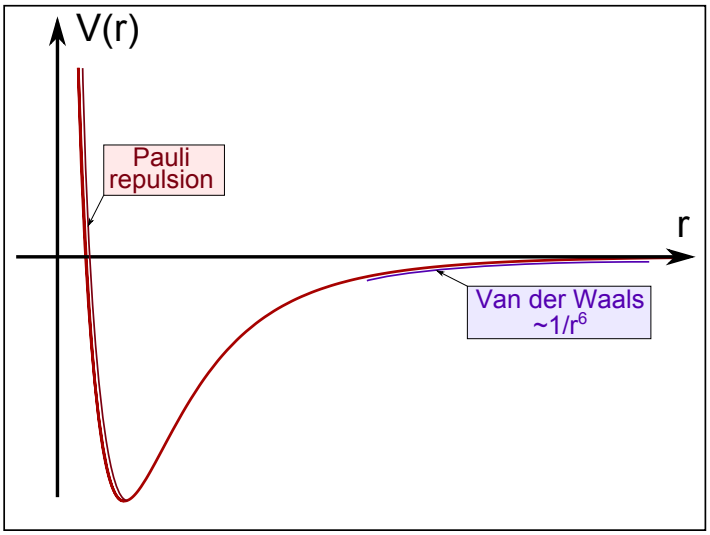

Figure 1.3: *Lennard-Jones interaction potential.*

since, the radius r_0 after which the potential becomes completely negligible, is very small with respect to the average inter-atomic distance. If n is the atomic density:

$$nr_0^3 \ll 1 \tag{1.47}$$

In this limit, called *dilute regime*, the particles in the gas behave most of the time as non interacting particles, until it happens that two particles came across and find each other at a distance comparable with r_0. We treat this scenario as a scattering process, where we don't care about the physics during the collision itself, but we are interested in how the kinetic properties of the particles change after the scattering process. This is what we call the *asymptotic limit*, i.e. the region where the effect of the potential is completely vanished and the particles can be considered free again.

The other limit we should keep in mind working with ultra-cold atoms is that they are actually *ultra-cold*. Qualitatively it means that the typical collision process occur at low momentum with respect to the scale given by the range of the potential:

$$r_0 \ll \frac{1}{k} \tag{1.48}$$

In this regime the atomic wavefunction is delocalized over a distance that is much bigger than the range of the potential. This means that the collision properties do not depend on the details of interaction potential and, in order to theoretically simplify the problem, we can model the potential as a spatial delta function with a coefficient that describe the physics of the scattering.

Partial wave expansion

In the limit of ultra-cold collisions it is natural to expand the scattering wave function on the spherical-wave basis. This is useful because, as we will realize, only few

functions of this basis contribute to the actual scattering wavefunction.

Since the interaction potential depends only on the distance between the two atoms, as we have already seen in previous sections (equation 1.43), the scattering amplitude can not depend on the azimuthal angle ϕ. This means that, in spherical basis expansion, we only have contributes from functions with $m_l = 0$:

$$\psi(\mathbf{r}) = \sum_{l=0}^{\infty} \sum_{m_l=-l}^{l} Y_l^m(\theta,\phi)\frac{u_{k,l,m_l}(r)}{r} \to \sum_{l=0}^{\infty} Y_l^0(\theta)\frac{u_{k,l}(r)}{r}, \tag{1.49}$$

where $Y_{m_l}^l$ are spherical harmonics and u_{k,l,m_l} is the radial wavefunction. Using this expansion into the Schrödinger equation 1.38 we write one effective one-dimensional equation for each radial wave function $u_{k,l}(r)$:

$$\left[\frac{d^2}{dr^2} + k^2 - \frac{l(l+1)}{r^2} - \frac{2m}{\hbar^2}V(r)\right] u_{k,l}(r) = 0, \tag{1.50}$$

where the third term contains the centrifugal barrier. We solve this set of equations imposing, on the radial wavefunction, the boundary condition $u_{k,l}(0) = 0$. We write the solution at large distance from the scattering region, in the asymptotic limit, $kr \gg 1$:

$$u_{k,l}(r) \simeq \sin\left(kr - \frac{l\pi}{2} + \delta_l\right), \tag{1.51}$$

where δ_l is the phase shift and it contains all the information about the variation of the l-harmonic component of the wavefunction, due to the scattering process.

From this equation it is possible to calculate the total scattering cross section distinguishing the case of identical bosons, identical fermions and finally non identical particle [15]:

$$\begin{cases} \sigma_B(k) = \dfrac{8\pi}{k^2}\displaystyle\sum_{l\text{even}}^{\infty}(2l+1)\sin^2\delta_l(k) & \text{(Identical bosons)} \\ \sigma_F(k) = \dfrac{8\pi}{k^2}\displaystyle\sum_{l\text{odd}}^{\infty}(2l+1)\sin^2\delta_l(k) & \text{(Identical fermions)} \\ \sigma_{n.i.}(k) = \dfrac{4\pi}{k^2}\displaystyle\sum_{l=0}^{\infty}(2l+1)\sin^2\delta_l(k) & \text{(Non identical particles)} \end{cases} \tag{1.52}$$

Scattering length

Because of the centrifugal term we find out that all the harmonics with $l \neq 0$ can be neglected in the limit of ultra-cold atoms collisions. Qualitatively this is shown in figure 1.4: if the centrifugal barrier is much bigger than the kinetic energy of the incoming particle, this particle is simply reflected and does not feel the details of

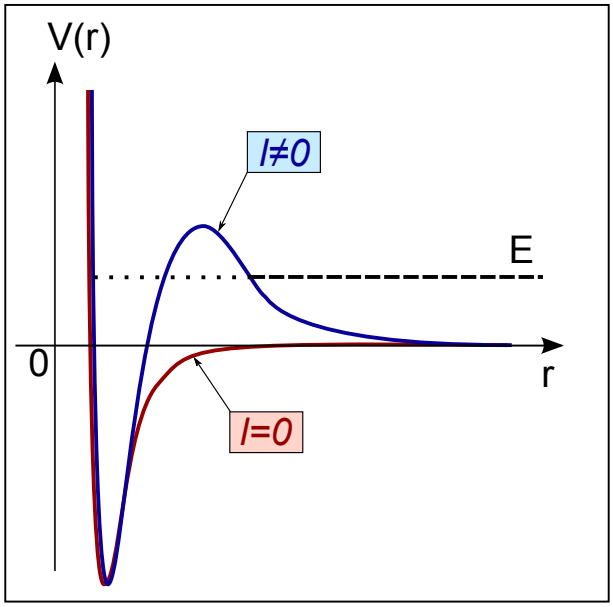

Figure 1.4: *In ultracold collisions the centrifugal term in equation 1.50 allows only s-wave scattering process. The red curve is the s-wave component of the potential ($l = 0$), the blue line is instead an example of ($l \neq 0$) component. E is the energy of the incoming particle.*

the short range potential. More quantitatively the scattering cross section, relative to the partial wave l, scales with the wavevector as [16]:

$$\sigma_l \propto k^{4l} \tag{1.53}$$

In the limit of $k \to 0$ only the s-wave (i.e. $l = 0$) contributes to the scattering length. In this limit one can introduce a very useful parameter called scattering length:

$$a = -\lim_{k \to 0} \frac{\tan \delta_0(k)}{k} \tag{1.54}$$

It is possible to show [15] how, in the low-energy expansion, the scattering amplitude is related to the scattering length by the simple relation:

$$f(k \to 0) = -\frac{a}{1 + ika - \dfrac{r_e k^2 a}{2}}, \tag{1.55}$$

where r_e is the effective range, which depends on the details of the interaction potential. The s-wave scattering cross section for bosons, for fermions and for distinguishable particles becomes in the same limit:

$$\begin{cases} \sigma_{0_B}(k \to 0) = \dfrac{8\pi a^2}{1 + k^2 a^2}. & \text{(Identical bosons)} \\ \sigma_{0_F}(k \to 0) = 0. & \text{(Identical fermions)} \\ \sigma_{0_{n.i.}}(k \to 0) = \dfrac{4\pi a^2}{1 + k^2 a^2}. & \text{(Non identical particles)} \end{cases} \tag{1.56}$$

We note here that the s-wave scattering for identical fermions vanishes because the scattering wavefunction must be antisymmetric. This is a very important properties to keep in mind concerning the cooling process in ultracold atoms experiments with fermions. During this process thermalisation is required, therefore collisions are necessary. To overcome this problem one can use two strategy: by mixing two different species of atoms (sympathetic cooling [17]) or by mixing two different internal states of the atoms (this is the strategy we adopt in our experiment). This property can also be exploited to produce an ideal Fermi gas.

Within the Born approximation [14], in the limit ($|a|, r_e \ll k^{-1}$), the effect of interaction is described by a delta-like potential of the form:

$$V(r) = \frac{4\pi\hbar^2}{m} a. \tag{1.57}$$

The interactions between ultracold dilute particles are described by a contact potential that depends only on one parameter: the scattering length. Changing the module of the scattering length is equivalent to change the strength of the interparticle interaction, while swapping its sign from positive to negative corresponds to go from a repulsive to an attractive interaction.

1.3 Fano-Feshbach resonance: BEC-BCS crossover

In the previous section we have seen how collisions in ultra-cold atoms can be described by the scattering length a. Thanks to Fano-Feshbach resonances, in ultracold atoms experiments, there is the possibility of tuning the scattering length by changing the magnitude of a static and homogeneous magnetic field B. This is possible because, during a scattering process, two atoms can pass through a resonant intermediate bound state. This mechanism physically appears in the form of a resonant behaviour of the scattering length. The magnetic field plays the role of a knob in this process, because, since there is a difference in the magnetic moment between the incoming scattering state and the bound state, tuning B has the effect of changing the energy difference between those two. It is therefore possible to reach the resonance for some value of $B = B_0$. On a phenomenological level, the effective scattering length close to a Fano-Feshbach resonance can be written as [18]:

$$a(B) = a_{bg}\left(1 - \frac{\Delta B}{B - B_0}\right), \tag{1.58}$$

where a_{bg} is the off-resonance background scattering length and ΔB is the width of the resonance.

In order to rigorously calculate the expression of the scattering length near a Fano-Feshbach resonance, one should solve a set of coupled differential equations called coupled channel equation. This approach is introduced in [15], but its description goes beyond the purpose of this thesis. We will instead focus on how

one can take advantages of the Fano-Feshbach resonance in order to experimentally explore very interesting topics of quantum many-body physics.

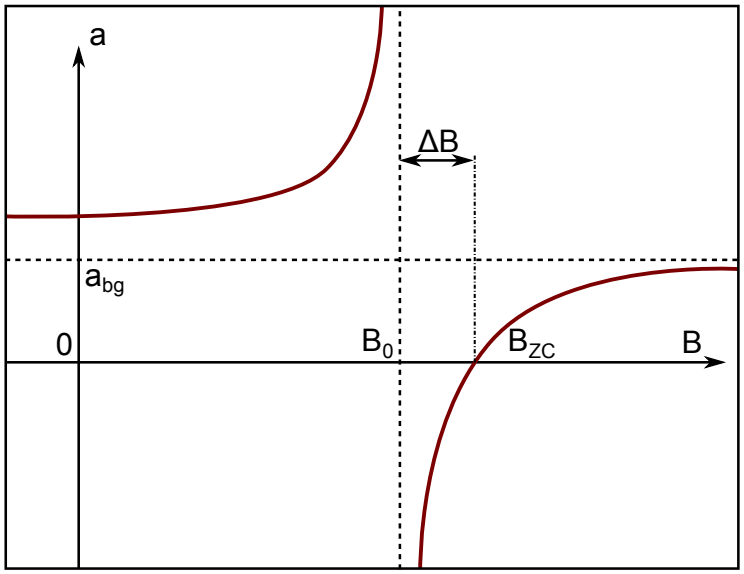

Figure 1.5: *Scattering length near a Fano-Feshbach resonance. a_{bg} is the background value of the scattering length, B_0 is the value of the magnetic field corresponding to the resonance, B_{ZC} is the value of magnetic field where the scattering length vanishes and ΔB is the width of the resonance.*

BEC-BCS crossover

The possibility of changing the inter-atomic interaction simply tuning a magnetic field, makes of ultracold atoms systems a perfect test bed for studying lots of many body physical theory, from superfluidity and superconductivity to, in some way, the more exotic physics of high T_c superconductors. In particular a gas of fermions in two different spin states allows to have, at the same time, strongly interacting gases and negligible three body losses[4] [11].

Depending on the scattering length we can identify three main regimes. Being k_F the Fermi wavevector we recognise:

- BEC regime for $1/(k_F\, a) \to \infty$: couple of atoms, with different spin state, form tightly bound bosonic molecules. The distance between these atoms is much smaller than the average inter-atomic spacing of the gas. Because of

[4] In strongly interacting systems three-body losses can't be, in principle, neglected any more, making impossible to perform experiment on them. Fortunately in the case of fermions the Pauli principle comes to help us: in order to interact, two fermions must have different spin. If the system has only two possible spin states, the presence of a third particle during a scattering process is highly suppressed because it would have the same spin state of one of the two colliding particles.

this the gas behaves almost identically to a Bose gas and, if cooled below the critical temperature, can form a Bose Einstein condensate.

- BCS regime for $1/(k_F\, a) \to -\infty$: the atoms form long-range Cooper pairs with a characteristic size much larger than the inter-particle spacing of the gas. This case is described by BCS theory (Bardeen-Cooper-Schrieffer) and the gas can undergo, at least in principle, to a superfluid transition.

- Crossover regime for $1/(k_F\, a) \to 0$: this is an intermediate regime between BEC and BCS. Like in the BCS regime it is characterized by the formation of Cooper pairs but this time the pair size is comparable to the inter-particle spacing.

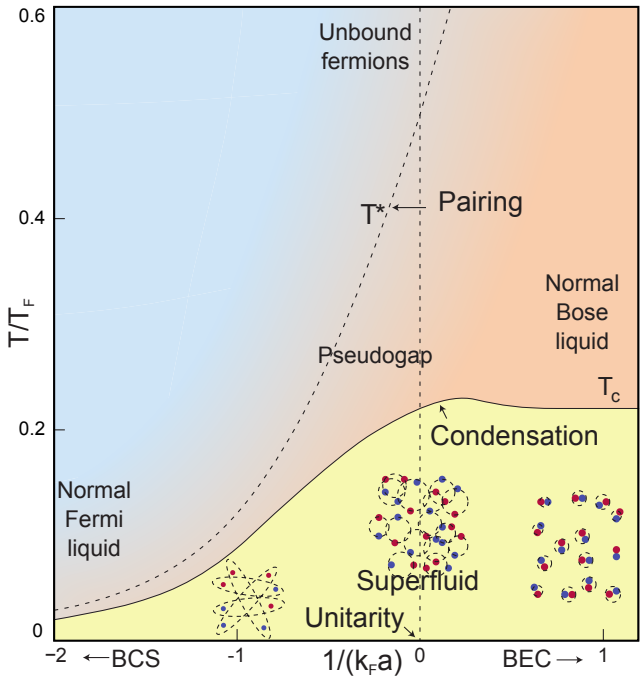

Figure 1.6: *Qualitative phase diagram of the BCS-BEC crossover as a function of the dimensionless parameter T/T_F and the dimensionless coupling strength $1/(k_F a)$. In the figure it is shown a scheme of the ground state evolution of an ultracold gas from the generalised Cooper pairs in the BCS regime, to the tightly bound bosonic molecules in the BEC side. The dashed curve shows the limit temperature T^* for the pair formation. Figure adopted from [19].*

One of the main difference between there three regimes is the value of the critical temperature, i.e. the temperature which correspond to the superfluid transition. As we can see in figure 1.6 the critical temperature decrease exponentially moving toward the BCS regime preventing, at the current state of art, to experimentally obtain

a superfluid in the deep BCS regime. On the other hand this critical temperature is higher in the BEC regime and reaches its maximum near the BEC-BCS crossover. This makes the latter regime very suitable for the study of the superfluid transition. In the following table, adopted from [20], we compare the ratio between the critical temperature and the Fermi temperature in very different physical scenarios.

System	T_C	T_F	T_C/T_F
Metallic lithium at ambient pressure	0.4 mK	55000 K	10^{-8}
Metallic superconductors	$1-10$ mK	$50000-150000$ K	$10^{-4}-10^{-5}$
^{3}He	2.6 mK	5 K	5×10^{-4}
High-T_C superconductors	$35-140$ K	$2000-5000$ K	$1-5\times10^{-2}$
Neutron star	10^{10} K	10^{11} K	10^{-1}
Strongly interacting atomic Fermi gases	200 nK	1 μK	0.2

1.4 Universal thermodynamics

In section 1.2 we have seen how the physics of ultracold atoms is dominated by s-wave collisions and the only parameter necessary to describe all the inter-atomic interactions is the scattering length. Because of this all the thermodynamic variables can depend only on three fundamental length scales:

- The average inter-particle spacing: $n^{-1/3}$, given by the density of the gas.
- The scattering length: a, given by the inter-particle interactions.
- The de Broglie wavelength: λ_{dB}, given by the temperature.

We can therefore write a quantity like the pressure as: $P = P(n, \lambda_{dB}, a)$. Choosing the density n as a natural scale we can normalise the pressure with the value of ideal gas, at $T = 0$, would assume at the same density: $P_0 = 2/5\, nE_F$. The ratio we obtain this way, P/P_0, is a dimensionless quantity and can be described by a universal function depending only on the dimensionless ratio T/T_F (temperature scale) and $1/(k_F\, a)$ [21]:

$$\frac{P}{P_0} = f_P\left(\frac{T}{T_F}, \frac{1}{k_F a}\right). \tag{1.59}$$

We have seen that, in correspondence of a Fano-Feshbach resonance, the scattering length diverges and the interaction reaches the maximum value allowed by quantum mechanics. In this limit, called unitary limit, also the length scale given by interaction is lost and the only remaining parameter is T/T_F. As a consequence all the thermodynamic variables, normalized to the ideal case, depend only on the ratio T/T_F, therefore they can all be linked together in a universal way. In other

words we can express any normalized quantity as a function of any other through a universal function.

Moreover in the limit of zero temperature all those normalised quantities assume the same value, called Bertsch parameter:

$$\boxed{\xi = \frac{E}{E_F} = \frac{P}{P_0} = \frac{\kappa_0}{\kappa}...} \tag{1.60}$$

where κ is the compressibility.

In the next section we find a way to link the universal functional relations between those variables to measurable quantities in order to finally obtain them experimentally in chapter 4.

1.5 Equation of state

In this section, we describe the two quantities around which orbits all the work of this thesis: the pressure and the compressibility. The choice of these thermodynamic variables is due to the fact that, from one side, they are quite easy to link to experimental observable (see chapter 2 and chapter 4) and, on the other hand, they are very suitable in order to unveil the superfluid transition of an unitary Fermi gas.

We will also present one of the few analytical treatment possible for studying a unitary Fermi gas: the virial expansion. This allows us to obtain the equation of state of unitary Fermi gas in the high temperature regime. We use this limit to check our procedure. The virial expansion analysis can be considered an effective tool to measure the temperature of the gas as shown in [5]. This is a very important achievement since there are no other easy thermometer available for a unitary Fermi gas.

1.5.1 Gibbs-Duhem equation

In ultracold atoms experiments there is basically one fundamental quantity one can measure: the density profile of trapped gas. The bridge between density and all other thermodynamic quantities is given by the Gibbs-Duhem equation [21]:

$$VdP - SdT - Nd\mu - Cda^{-1} = 0, \tag{1.61}$$

where V is the volume, P the pressure, S the entropy, T the temperature, N the number of atoms, μ the chemical potential, C the contact constant and a the scattering length. The contact is a quantity that measure the probability of two particle to be within a short distance of each other and it is defined by the relation [21][22]:

$$C = -\frac{\partial E}{\partial a^{-1}}\bigg|_{S,N,V}. \tag{1.62}$$

In the special case of ultracold atoms the equation 1.61 can be simplified considering two properties of the cloud:

- The gas is in thermal equilibrium $\rightarrow dT = 0$.
- The variation of the magnetic field through the cloud is negligible with respect to the width of the Fano-Feshbach resonance $\rightarrow da^{-1} = 0$.

The final relation one obtains is:

$$\boxed{dP = n\ d\mu,} \tag{1.63}$$

where $n = N/V$. The pressure is obtained integrating this equation:

$$P(\mu) = \int_{-\infty}^{\mu} d\mu' n(\mu') \tag{1.64}$$

Local compressibility

One of the main goal of this thesis is to experimentally observe the superfluid transition in a strongly interacting Fermi gas. Being this a second order phase transition, it reveals itself in a singularity of the second derivative of the grand potential Ω, or equivalently of the pressure P. Therefore a natural candidate to study the superfluid transition is the isothermal compressibility, being proportional to the second derivative of pressure with respect to the chemical potential:

$$\kappa = -\frac{1}{V}\frac{\partial V}{\partial P} = \frac{1}{n^2}\frac{\partial n}{\partial \mu} \tag{1.65}$$

It is exactly thanks to this quantity that we will observe a signature of the superfluid transition in our system.

Specific heat

As we have seen in section 1.4 knowing the universal function like $\tilde{\kappa} = \kappa/\kappa_0 = \tilde{\kappa}(\tilde{P})$ implies, in the unitary regime, the knowledge of all the others universal relations between normalised thermodynamic quantities. In order to find the connection between the specific heat, C_V, and the normalised temperature, $\tilde{T} = T/T_F$ (being T_F the Fermi temperature), we start finding a relation between the normalised pressure and the normalised temperature. Thanks to this we are able to link an intuitive thermometer, given by the temperature, to one given by pressure, that is much easier to obtain experimentally. Following [21], we note that:

$$\frac{d\tilde{P}}{d\tilde{T}} = -\frac{T_F}{\tilde{T}}\frac{\partial \tilde{P}}{\partial T_F}\bigg|_T = -\frac{1}{\tilde{T}}\frac{3}{2}n\frac{\partial \tilde{P}}{\partial n}\bigg|_T. \tag{1.66}$$

The derivative in the last term can be explicitly written as:

$$n\frac{\partial \tilde{P}}{\partial n}\bigg|_T = -n\frac{\tilde{P}}{P_0}\frac{\partial P_0}{\partial n} = \frac{5}{3}\left(\frac{1}{\tilde{\kappa}} - \tilde{P}\right), \tag{1.67}$$

Using 1.67 in equation 1.66 we obtain the relation:

$$\frac{d\tilde{P}}{d\tilde{T}} = \frac{1}{\tilde{T}}\frac{5}{2}\left(\tilde{P} - \frac{1}{\tilde{\kappa}}\right). \tag{1.68}$$

This equation can be integrated to find $\tilde{T}$:

$$\tilde{T} = \tilde{T}_i \exp\left(\int_{\tilde{P}_i}^{\tilde{P}} d\tilde{P} \frac{1}{\tilde{P} - \frac{1}{\tilde{\kappa}}}\right), \tag{1.69}$$

where $\tilde{T}_i$ is the normalised temperature corresponding to an initial normalised pressure $\tilde{P}_i$. Practically this quantity can be estimated choosing $\tilde{P}_i$ to be in the high temperature known regime such the virial or the Boltzmann one. This will allow us to estimate its value in a region where the physics is well known and calibrate this way our thermometer in the low temperature region.

Remembering the definition of the specific heat [10]:

$$C_V = \left.\frac{\partial E}{\partial T}\right|_V, \tag{1.70}$$

one can, using the relation[5] $E = 3/2PV$ and the equation 1.68, write:

$$\frac{C_V}{k_B N} \equiv \left.\frac{1}{k_B N}\frac{\partial E}{\partial T}\right|_{N,V} = \frac{3}{2}\frac{\partial \tilde{P}}{\partial \tilde{T}} = \frac{3}{2}\frac{1}{\tilde{T}}\left(\tilde{P} - \frac{1}{\tilde{\kappa}}\right). \tag{1.74}$$

While at high temperature ($T/T_F \geq 1$), as we have seen in section 1.1.2, the specific heat reach the value equal to the one of an ideal Fermi gas $C_V \to 3/2Nk_B$, at low temperature, as we will see in chapter 4, it shows a narrow peak. This peak is a

[5] This relation, we have found in the case of ideal gases in section 1.1.1, is remarkably identical to the one of a unitary gas unitary [21]. This can be seen starting from the definition of pressure:

$$P = -\left.\frac{\partial E}{\partial V}\right|_{N,S}. \tag{1.71}$$

Fixing the number of particle and the entropy is equivalent to fix E/E_0 [21], therefore one can write:

$$P = -\left.\frac{E}{E_0}\frac{\partial E_0}{\partial V}\right|_{N,S} = \frac{2}{3}\frac{E}{V}. \tag{1.72}$$

From this equation follows directly the relation:

$$\boxed{E = \frac{3}{2}PV.} \tag{1.73}$$

clear signature of superfluid transition. A jump in C_V like this one can be found in the presence of all kind of second order phase transition such as the λ-transition in ^{4}He or the superconductor phase transition. An example of this transition in the ^{3}He is reported in figure 1.7.

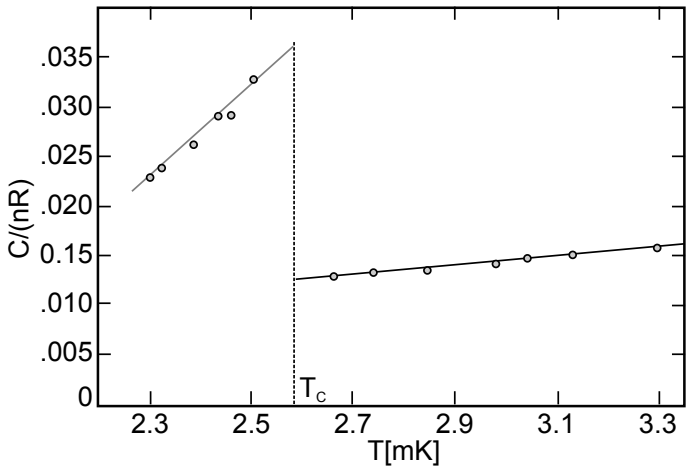

Figure 1.7: *λ transition in the specific heat of fermionic ^{3}He at $T_C \simeq 2.6mK$. From [23].*

From the position of this jump we can estimate the critical temperature T_c/T_F, that represent the critical conditions of density and temperature at which the superfluid transition takes place. The results of this measurement are reported in section 4.5.

1.5.2 Pressure and compressibility of an ideal Fermi gas

The main goal of this thesis is to study the superfluid transition of a unitary Fermi gas, however, it is also very useful to introduce some results, concerning the pressure and the compressibility of an ideal Fermi gas. The reason is that we can experimentally produce[6], in very good approximation, and ideal gas and obtain its equation of state. We have then the possibility of comparing a well known theory with the experiment and this will allow us both to check and tune our experimental procedure.

In section 1.1 we derived the expression for the grand potential of a non interacting Fermi gas. From the grand potential function Ω we have calculated the pressure and the internal energy using the Sommerfeld expansion for low temperature. Here we start from Ω but we follow a direct numerical approach. We focus on finding an expression for pressure and compressibility and we finally link them together in a

[6] In order to produce a non interacting gas we exploit the zero-crossing region of the Fano-Feshbach resonance. The experimental procedure is described in chapter 4.12. One other option to obtain non interacting Fermi gas is actually produce a fully polarized Fermi gas. This way all the interaction are suppressed by the Pauli principle.

universal equation of state. For more details about calculations in this section one can read Appendix A of Nascimbène PhD thesis [24].

Recalling the equation 1.17, we write the grand potential as [25]:

$$\Omega = -k_B T \int_0^\infty d\epsilon\, \rho(\epsilon) \log\left[\frac{1}{1+\exp(-\frac{\epsilon-\mu}{k_B T})}\right], \tag{1.75}$$

where $\rho(\epsilon) = V m^{\frac{3}{2}}(\sqrt{2}\pi^2\hbar^3)^{-1}\sqrt{\epsilon}$ is the density of states of a single spinless particle of mass m in a box of volume V. Since the grand potential $\Omega = E - TS - \mu N = -PV$, we write the pressure of an ideal Fermi gas as a function of chemical potential μ and temperature T:

$$\begin{aligned} P_{\text{n.i.}}(\mu, T) &= \frac{1}{6\pi^2}\left(\frac{2m}{\hbar^2}\right)^{\frac{3}{2}} \int_0^\infty d\epsilon \frac{\epsilon^{\frac{3}{2}}}{1+\exp(\frac{-\mu}{k_B T})} \\ &= \frac{k_B T}{\lambda_{dB}^3(T)\frac{4}{3\sqrt{\pi}}} \int_0^\infty du \frac{u^{\frac{3}{2}}}{1+\exp(\frac{\epsilon-\mu}{k_B T})\exp(u)}, \end{aligned} \tag{1.76}$$

where we integrate by parts and introduce the integration variable $u = \epsilon/k_B T$. The integral in 1.76 is a function of $\mu/k_B T$ only and can be expressed using the function $f_{5/2}$ defined as[7]:

$$f_{5/2}(z) = \sum_{n=1}^{\infty} (-1)^{n+1} \frac{z^n}{n^{5/2}} \tag{1.78}$$

Introducing the inverse of fugacity $\zeta = e^{-\mu/k_B T}$ we write the pressure of an ideal Fermi gas in the form:

$$P_{\text{n.i.}}(\mu, T) = \frac{k_B T}{\lambda_{dB}^3(T)} f_{5/2}(\zeta^{-1}) \tag{1.79}$$

From this equation we can calculate the density n_0[8]

$$n_0(\mu, T) = \frac{d}{d\mu} P_{\text{n.i.}}(\mu, T) = \frac{1}{\lambda_{dB}^3(T)} f_{3/2}(\zeta^{-1}) \tag{1.82}$$

[7] The function $f_{5/2}$ is practically identical to the Polylogarithm function $\text{Li}_{5/2}$, but with opposite sign convention:

$$f_{5/2}(z) = -\text{Li}_{5/2}(-z). \tag{1.77}$$

[8] We remember the derivation rule for the polylogarithm function:

$$z\frac{\partial \text{Li}_s(z)}{\partial z} = \text{Li}_{s-1}(z), \tag{1.80}$$

or, more practically in our case:

$$\frac{\partial \text{Li}_s(e^\mu)}{\partial \mu} = \text{Li}_{s-1}(e^\mu), \tag{1.81}$$

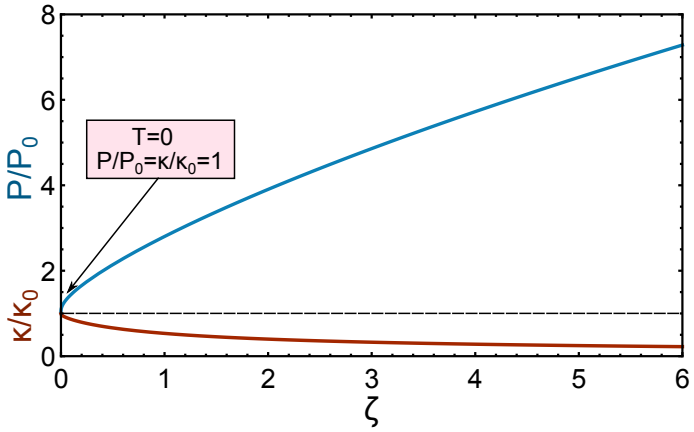

Figure 1.8: *In blue the normalised pressure as a function of ζ. In red the normalised compressibility.*

and the compressibility:

$$\kappa(\mu,T) = \frac{1}{n_0(\mu,T)^2}\frac{d}{d\mu}\left[n_0(\mu,T)\right] = \lambda_{dB}^3(T)k_BT\frac{f_{1/2}(\zeta^{-1})}{f_{3/2}(\zeta^{-1})^2}. \tag{1.83}$$

All those quantities depend on temperature and chemical potential. We want now to express them as a function of only one parameter. This is done normalizing them by the corresponding value, at the same local density at $T = 0$.

Normalized pressure of an ideal Fermi gas

Following the approach described in section 1.4 we start finding the expression for the normalized pressure, $\tilde{P}_0$:

$$\tilde{P}_0 = \frac{P_{\text{n.i.}}(\mu,T)}{P_0(n)}, \tag{1.84}$$

where we introduced here the pressure of a non interacting Fermi gas, at temperature $T = 0$ and local density n:

$$P_0(n) = \frac{2}{5}nE_F. \tag{1.85}$$

We can now explicitly write the value of the normalised pressure replacing, in equation 1.84, the expressions found in equation 1.79 and 1.85.

$$\tilde{P}_0 = \frac{10}{3^{2/3}\pi^{1/3}}\frac{f_{5/2}(\zeta^{-1})}{\left[f_{3/2}(\zeta^{-1})\right]^{5/3}}. \tag{1.86}$$

As we have already anticipated, the normalized pressure depends only on the parameter ζ, or equivalently on the adimensional ratio $\mu/(k_BT)$.

Normalized compressibility of an ideal Fermi gas

We now calculate the normalised compressibility following the same reasoning we have employed for the pressure. The compressibility of a non interacting Fermi gas, at $T = 0$ and local density n is:

$$\kappa_0(n) = \frac{3}{2}\frac{1}{nE_F}. \tag{1.87}$$

From this the normalized compressibility is:

$$\tilde{\kappa}_0 = \frac{\kappa}{\kappa_0} = \left(\frac{\pi}{3}\right)^{1/3} \frac{f_{1/2}(\zeta^{-1})}{2\left[f_{3/2}(\zeta^{-1})\right]^{1/3}} \tag{1.88}$$

Pressure vs compressibility

Since both normalised compressibility and normalised pressure are functions of the same single variable ζ, we can actually show directly the dependence of the first with respect to the latter:

$$\tilde{\kappa}_0 = g_0(\tilde{P}_0), \tag{1.89}$$

where g_0 is the function plotted in figure 1.9. Since experimentally we can reach the

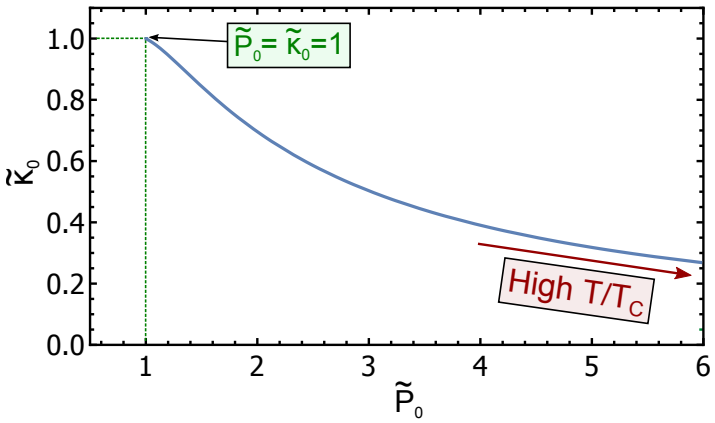

Figure 1.9: *Non interacting equation of state in the form* $\tilde{\kappa}_0 = g_0(\tilde{P}_0)$.

regime of *non interacting* Fermi gas, we can actually measure the function g_0. This is very important because we can use this known regime to both calibrate and check the experimental procedure and the numerical analysis.

1.5.3 Virial expansion: a new thermometer for strongly interacting Fermi gases

Describing strongly interacting Fermi gases is a very hard task in many-body physics. Most of theoretical approaches to this problem are based on quantum Monte Carlo

(QMC) simulations [26][7], but, at this stage, numerical simulations suffer from sign problem for fermions (antisymmetrization of the wavefunction) or from the finite size effects in small samples. That is why exacts results in non-trivial limits are very valuable. The limit we are interested in is the high temperature limit, where quantum virial expansion provides a bridge from many-body physics to few body physics. The properties of a strongly interacting Fermi gas can be expanded in a non-perturbative way, using expansion coefficients, calculable from few-fermions systems [27].

The basic idea of virial expansion is that, at high temperature, the correlation between particles would become more and more weak. At a certain point, the scattering cross section, σ, becomes of the order of λ_{dB}^2, where λ_{dB} is the de Broglie wavelength. In this region σ becomes much smaller than the average inter-atomic distance. As a result it is possible to describe the properties of the system starting from a few-body problem. The mathematical derivation and complete description of the virial expansion method is beyond the scope of this thesis. For a deeper insight into this problem one can read the review written by Xia-Ji Liu [27].

Grand potential in the virial regime

In this thesis we start from the grand canonical potential expressed as a high-temperature series of ζ^{-1}:

$$\Omega(\mu, T) = -\frac{2K_B T V}{\lambda_{dB}^3(T)} \left[b_1 \zeta^{-1} + b_2 \zeta^{-2} + b_3 \zeta^{-3} + b_4 \zeta^{-4} + ... \right], \tag{1.90}$$

where b_i are the so-called virial coefficients. The values of b_i until the third order can be found in the literature [28]: $b_1 = 1,\ b_2 = 3\sqrt{2}/8,\ b_3 = -0.29095295$. From this equation we can calculate the pressure:

$$P_v = -\frac{\Omega}{V} \simeq \frac{2K_B T}{\lambda_{dB}^3(T)} \left(b_1 \zeta^{-1} + b_2 \zeta^{-2} + b_3 \zeta^{-3} \right), \tag{1.91}$$

the density:

$$n = \frac{dP}{d\mu} \simeq \frac{2}{\lambda_{dB}^3(T)} \left(b_1 \zeta^{-1} + 2b_2 \zeta^{-2} + 3b_3 \zeta^{-3} \right) \tag{1.92}$$

and the compressibility:

$$\kappa_v = \frac{1}{n^2} \frac{dn}{d\mu} \simeq \frac{1}{n^2} \frac{2}{\lambda_{dB}^3(T) k_B T} \left(b_1 \zeta^{-1} + 4b_2 \zeta^{-2} + 9b_3 \zeta^{-3} \right) \tag{1.93}$$

$$= \frac{\lambda_{dB}^3(T) k_B T}{2} \frac{\left(b_1 \zeta^{-1} + 4b_2 \zeta^{-2} + 9b_3 \zeta^{-3} \right)}{\left(b_1 \zeta^{-1} + 2b_2 \zeta^{-2} + 3b_3 \zeta^{-3} \right)^2}. \tag{1.94}$$

Normalised pressure and compressibility for strongly interacting Fermi gases in high T/T_c regime

As we have already done for the non interacting case in section 1.5.2, we normalise both the pressure and the compressibility in order to obtain adimensional parameter.

We explicitly write the normalised pressure:

$$\tilde{P}_v = \frac{P_v}{P_0} = \frac{5}{3^{2/3}} \left(\frac{2}{\pi}\right)^{1/3} \frac{b_1\zeta^{-1} + b_2\zeta^{-2} + b_3\zeta^{-3}}{(b_1\zeta^{-1} + 2b_2\zeta^{-2} + 3b_3\zeta^{-3})^{5/3}}, \tag{1.95}$$

and the normalised compressibility:

$$\tilde{\kappa_v} = \frac{\kappa_v}{\kappa_0} = \left(\frac{\pi}{6}\right)^{1/3} \frac{b_1\zeta^{-1} + 4b_2\zeta^{-2} + 9b_3\zeta^{-3}}{(b_1\zeta^{-1} + 2b_2\zeta^{-2} + 3b_3\zeta^{-3})^{1/3}}. \tag{1.96}$$

Again these two quantities depend only on ζ and are linked together by a function we name g_v:

$$\tilde{\kappa_v} = g_v(\tilde{p_v}). \tag{1.97}$$

We plot this function in figure 1.10.

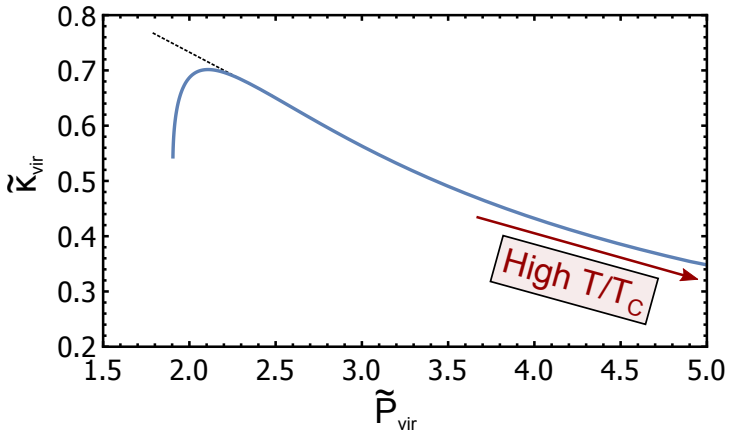

Figure 1.10: *Equation of state obtained using the high temperature third order virial expansion.*

Experimentally, when we measure this kind of curve, we are not limited by the high temperature approximation, but we span a wider range of $\mu/(k_BT)$ having a unitary Fermi gas cooled below the superfluid transition. Nevertheless equation (1.97) is still very useful because we can compare it with the measurements we perform on the high temperature tails of the atomic cloud. We point out that the term *high temperature* in this context can be misleading, since the atomic cloud on which we perform all the measurements is at thermal equilibrium, therefore T is constant in the whole system. What we really mean here is actually high T/T_c ratio. Since T_c decrease with density, this ratio becomes much bigger in the cloud tails, where the density vanishes.

As we show in section 4.3 we use equations 1.95 and 1.96, in the virial regime, to estimate the temperature of the cloud. This has a great importance since we haven't access to other kind of thermometry in the unitary regime. Beside that we can also experimentally evaluate the goodness of the parameter b_3 we used and also we can estimate a value for the next coefficient b_4. This is useful because, while the b_1 and b_2 coefficients can be obtained from analytical calculations [28], higher coefficients requires numerical calculation [29] or direct experimental measurement [5].

Chapter 2

Measuring the EOS of ultracold gases

We build up the bridge between the thermodynamic quantities introduced previously and the experimental observables: the density and the trapping potential. We will show how to map the physics of an ultracold trapped gas to the physics of many homogeneous systems using the local density approximation. In particular we describe the method to extract the thermodynamics (the equation of state) from a single experimental density profile, via the combination of inverse Abel transformation and local density approximation. We also discuss about the validity of our treatment in the case of ultracold atomic systems.

2.1 Local density approximation (LDA)

In the previous chapter we have described the main thermodynamic properties of a homogeneous system, considering the gas to be in a very large box. In ultracold atoms experiments the scenario is actually very different, since the gas is confined in a trapping potential $U(\mathbf{r})$. At first sight, one can think that the presence of the trap could make difficult to link the measured quantities to the thermodynamics of a bulk system. Vice versa, we will show how the presence of the trap turns out to be a very useful and powerful feature, if local density approximation is exploited [30][3][5][4]: from a single experimental density profile of the trapped gas we can obtain the thermodynamics of many homogeneous systems!

In the local density approximation one assumes thermodynamic equilibrium to hold in an infinitesimal volume ΔV around every point $\mathbf{r}$ of the trapped gas. Every infinitesimal volume is then considered as an independent system, characterized by the local potential $U(\mathbf{r})$. Since these systems can exchange particles with the surrounding ones, we choose to use the grand-canonical description with fixed local chemical potential [21]:

$$\mu(\mathbf{r}) = \mu_0 - U(\mathbf{r}) \tag{2.1}$$

where μ_0 is the maximum chemical potential. In this description, the density of each of those volumes, called local density $n(\mathbf{r})$, depends only on local trapping

potential $U(\mathbf{r})$ and global quantities, considered constants through the cloud, such as temperature T and scattering length a:

$$n(\mathbf{r}) \equiv n(\mu_0 - U(\mathbf{r}), T, a), \tag{2.2}$$

In the experiment, the temperature and the scattering length practically do not depend on the position $\mathbf{r}$. The gas is indeed at thermal equilibrium while the scattering length is also constant because it depends on the local value of the magnetic field, which varies very slow with respect to the dimension of the cloud[1].

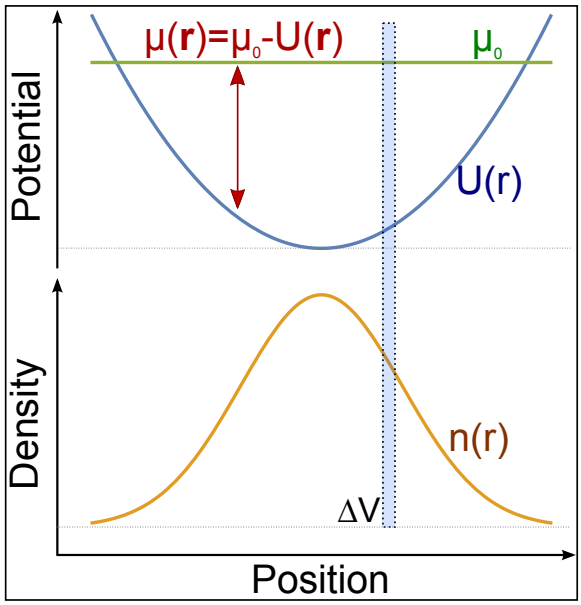

Figure 2.1: *Local density approximation scheme. Each infinitesimal volume is consider to be an independent system, characterised only by the local chemical potential, the temperature and the scattering length. $U(\mathbf{r})$ is the local potential and $n(\mathbf{r})$ is the local density.*

The power of this approximation is already clear: with only one experimental image we can, in principle, obtain the entire equation of state of the trapped gas, since every pixel represents in fact a different and independent thermodynamic system. Considering our experimental apparatus, as shown in chapter 3, a density profile consists in a matrix of $\sim 10000 \div 20000$ pixels and, each of them, represents a measure on a different bulk system.

In the following, we will show how to link the density of the trapped atoms to the pressure and to the compressibility. We focus on these two quantities because it is

[1]

$$|\nabla_{\mathbf{r}} B| \times \Delta R \ll \Delta B, \tag{2.3}$$

where ΔR is the dimension of the cloud, B is the magnetic field and ΔB is the width of the Fano-Feshbach resonance.

easy to relate them with density and, as we have seen in the case of the unitary Fermi gas (see section 1.4), it is always possible to write any couple of thermodynamics quantities as a function of these two.

Pressure and compressibility in LDA

In section 1.5 we have used the Gibbs-Duhem equation in order to obtain a relation between pressure and chemical potential.

$$P(\mu) = \int_{-\infty}^{\mu} d\mu' n(\mu') \tag{2.4}$$

With local density approximation we are able to link the chemical potential to the experimental trapping potential U. Using the equation 2.1 we write the equation for hydrostatic equilibrium in the form [21]:

$$dP = nd\mu = -ndU \tag{2.5}$$

The local pressure $P(\mathbf{r})$, corresponding to the infinitesimal volume $\Delta V(\mathbf{r})$ with local potential $U(\mathbf{r})$, can be written as:

$$\boxed{P(U) = \int_{U}^{\infty} dU' n(U').} \tag{2.6}$$

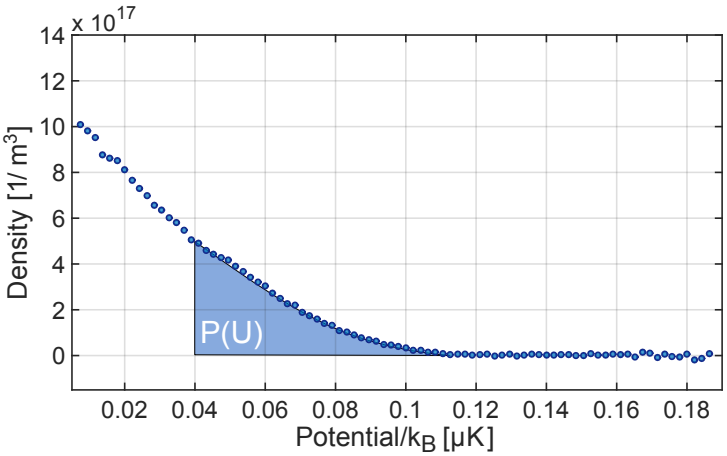

Figure 2.2: *Sketch of the idea behind the calculation of the pressure. The blue points are an example of an experimental density profile $n(U)$.*

A simple way to visualise this equation is to think about the atmospheric pressure. This pressure is given by the weight of the air above the measurement point. Equation 2.6 describes exactly this when one chooses U to be the gravitational potential: $U(h) \to mgh$. This way we integrate the air density over the gravitational potential obtaining as result nothing but the atmospheric pressure itself.

The same substitution can be done for compressibility. From equation 1.65 we write:

$$\boxed{\kappa = -\frac{1}{n^2}\frac{dn}{dU}.} \tag{2.7}$$

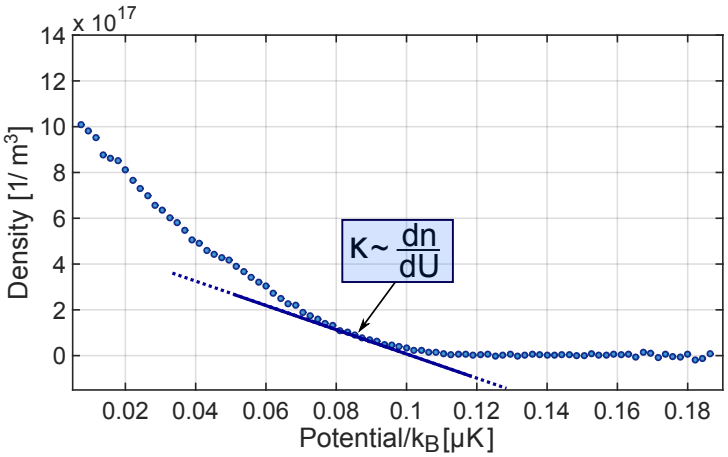

Figure 2.3: *Sketch of the idea behind the calculation of the compressibility. The blue points are an example of an experimental density profile $n(U)$.*

We have obtained two expressions that, linking the pressure and the compressibility to the density and the trapping potential, create a bridge from the thermodynamic quantities we are interested in, to the experimental observables. In chapter 4 we are going to use those equations to reconstruct the equation of state of a unitarity gas. In the next section we will describe what, in practice, this approximation actually means.

2.1.1 Limits of LDA

We now discuss when the local density approximation is a good approximation and what are the limits of applicability. We start describing the easier case of molecular condensate (BEC limit) introducing the concept of healing length. Finally we discuss about the applicability of LDA in the unitary limit, where the coherence length takes the role of the healing length.

LDA in the BEC limit

In order to study the applicability limits of the local density approximation we start considering, following [24], the simple situation of two component balanced Fermi gas in the BEC limit ($1/k_F a \gg 1$). The gas is described by the Gross-Pitaevskii equation:

$$\left(-\frac{\hbar^2}{4m}\nabla^2 + U(\mathbf{r}) + \frac{4\pi\hbar^2 a_{dd}}{2m}n\right)\sqrt{n} = \mu\sqrt{n}\,, \tag{2.8}$$

where n is the density of molecules, a_{dd} the dimer-dimer scattering length, μ the chemical potential and $U(\mathbf{r})$ the trapping potential. We suppose that the potential is harmonic and isotropic, with trapping frequency ω. The factor 4 in the kinetic term comes from the fact that we called m the mass of a single particle and not of the dimer.

When the kinetic energy is negligible with respect to the interaction energy the Gross-Pitaevskii equation simplifies in the so called Thomas-Fermi limit. Within this approximation we can write the density profile as [31]:

$$n(\mathbf{r}) = \frac{m}{2\pi\hbar^2 a_{dd}} \left(\mu - U(\mathbf{r})\right). \tag{2.9}$$

As we have seen, the density profile depends only on quantities related only to a precise spatial location regardless of the surrounding points (this statement was false in the Gross-Pitaevskii equation because of the derivative in the kinetic term). For this reason the Thomas-Fermi limit is equivalent to the Local Density Approximation. The physics of this system is in fact completely described by local quantities.

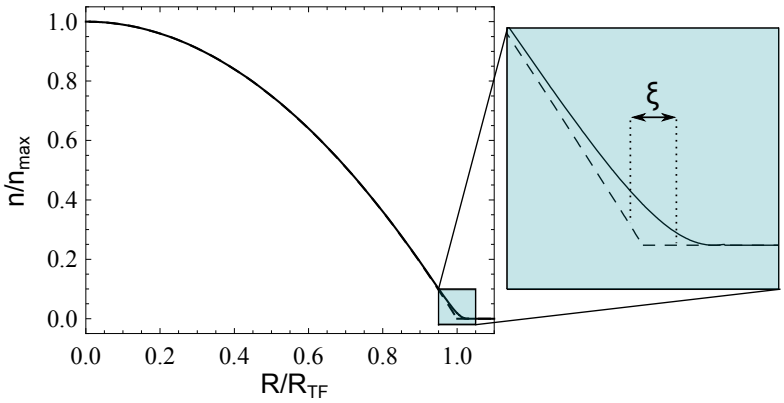

Figure 2.4: *Deviation between the density profile calculated with Gross-Pitaevskii equation (solid line) and Thomas-Fermi approximation (dashed line). Image adopted from [24].*

Qualitatively we can estimate the error introduced by local density approximation following this line of reasoning. LDA holds when the kinetic energy is small compared to interacting energy:

$$\frac{P^2}{4m} \ll \frac{4\pi\hbar^2 a_{dd}}{2m} n. \tag{2.10}$$

Using the relation $PX \sim \hbar$ we rewrite this inequality in the form:

$$X^2 \gg \frac{1}{8\pi a_{dd} n} = \xi^2 \tag{2.11}$$

where we introduce the healing length $\xi = 1/\sqrt{8\pi a_{dd} n}$. This means that local density approximation can not resolve correctly details of the order of the healing length or smaller. Since the cloud size is much bigger than the healing length, we can conclude that LDA accurately describes the density profile of a trapped Fermi gas in the BEC limit.

The healing length

In order to get an insight on the physical meaning of the healing length is useful to consider, following [31] and [15], the case of interacting bosons confined in a box potential. We note that we are studying here a physical scenario in some sense opposite to the one of the previous sections. While in the previous case the trapping potential varies relatively smoothly in space, we investigate here the case of infinitely hard walls.

We consider a box of volume L^3 with periodical boundary conditions along two axis and a strict boundary condition along the planes $x = 0$ and $x = L$. In the case of non interacting gas, the wave function, along $\hat{x}$, is practically the ground state of the trap:

$$\psi(x) = \frac{2}{\sqrt{L}} \sin\left(\frac{\pi x}{L}\right). \tag{2.12}$$

In the presence of interactions the wave function tends to minimize the interaction energy and, in practice, it is inclined to be as homogeneous as possible. The point is that the wavefunction still has the constrain to vanish at $x = 0, L$ because of the boundary conditions. The meaning of the healing length lies exactly here: it represents the characteristic length scale over which the wave function, in the presence of interactions, varies from 0 to the region where the density is constant. In other words it is the minimum distance required by a wavefunction to recover its value (*to heal*) from a local perturbation.

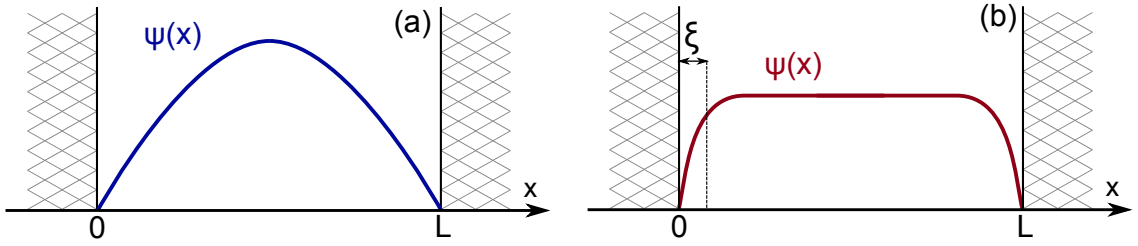

Figure 2.5: *On the left the ground state wavefunction of a non interacting bosons in a box. On the right the ground state wavefunction of interacting bosons. The healing length ξ is the characteristic length after which the wavefunction recovers from a local perturbation like the boundary conditions imposed by the walls.*

LDA in the unitary limit

In the unitary limit the calculation reported above is not possible, since the Gross-Pitaevskii equation is not a good description of the system any more. What we can do is considering, instead of the healing length, the correlation length. In general local density approximation seems to hold also in this case since, the correlation length is of the order of the inverse of the Fermi wave vector, $1/k_F$, that is still much smaller than the cloud size. A problem rises in proximity of the transition between the superfluid and the non superfluid region of the cloud. The problem comes out because of the divergence of the correlation length, being this, a second order phase transition. In this critical region the coherence length diverges according to [24]:

$$\xi \sim \frac{1}{k_F} \left| \frac{T - T_c}{T} \right|^{-\nu}, \tag{2.13}$$

where $\nu \simeq 0.67$ and T_c is the critical temperature, where the transition occurs. In order to find out if this is a real problem or not in the context of our experiment, we consider a gas in an isotropic trap, with trapping frequency ω, sufficiently cold to have a superfluid fraction. Near the critical region we can write the coherence length as a function of the distance, δr, from the critical radius R_c. The critical radius is defined as the radius where the phase transition occurs.

$$\xi(\delta r) = \frac{1}{k_F} \left(\frac{\mu(R_c + \delta r) - \mu(R_c)}{\mu(R_c)} \right)^{-\nu}, \tag{2.14}$$

where μ is the chemical potential. In order to estimate the length over which the

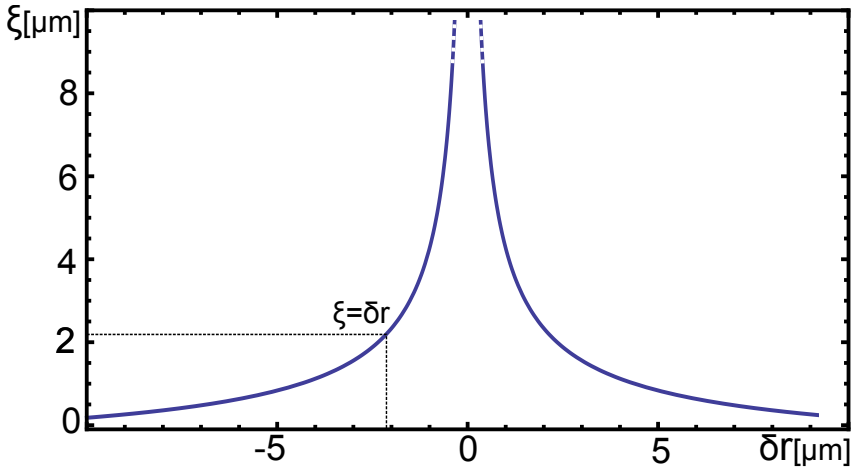

Figure 2.6: *Coherence length across a second order phase transition. δr is the distance from the point the phase transition occurs. The dashed line indicate the distance from the phase transition point where the coherence length assume the value of the distance itself: $\delta r = \xi$.*

local density approximation holds, we can consider the quantity, $\tilde{\delta r}$, the distance

from the transition radius where the coherence length assume the value of $\tilde{\delta r}$ itself:

$$\tilde{\delta r} = \xi(R_c + \tilde{\delta r}) \sim \frac{1}{k_F}\left(\frac{m\omega^2 R_c \tilde{\delta r}}{m\omega^2 R_c}\right), \tag{2.15}$$

solving for $\tilde{\delta r}$,

$$\tilde{\delta r} \sim \left[\frac{1}{(3\pi^2 n)^{1/3}} R_c^{\nu}\right]^{\frac{1}{\nu+1}}, \tag{2.16}$$

where we express the Fermi wave vector k_F as a function of density, $k_F = (3\pi^2 n)^{1/3}$. Considering typical number in ultracold atoms experiments, $n \sim 2 \times 10^{17}\mathrm{m}^{-3}$ and $R_c \sim 20\mu$m, we obtain $\tilde{\delta r} \sim 2\mu$m, that is of the order of the finite resolution resolution we have in our imaging setup.

We can conclude that the local density approximation accurately describes the density of a trapped Fermi gas at unitarity, cooled below the critical temperature T_c, except for a small region of $1 \div 2\mu$m around the region where the superfluid phase transition occurs. Because of this we can predict that a measurement of the equation of state in this region will show a peak, instead of the actual divergence, that is smoothed both by the imaging resolution and by the effect of the coherence length, as it has already been observed by [5].

2.2 Inverse Abel transformation

In the previous section, we have seen how with local density approximation, we can obtain the pressure and the compressibility knowing the density of the cloud $n(\mathbf{r})$ and the trapping potential $U(\mathbf{r})$. While the latter can be easily obtained experimentally, the density is not directly accessible. The real quantity we actually can measure is the integrated density, $n_{2D}(x, y)$, of the cloud (see absorption imaging section 3.3.1). As we will show in the next chapter, this quantity is the integral of the density, that we now call $n_{3D}(x, y, z)$ for clarity, along the imaging direction:

$$n_{2D}(x, y) = \int dz\ n_{3D}(x, y, z). \tag{2.17}$$

In order to reconstruct the 3D-density we use a transformation called Abel deconvolution [32].

Abel deconvolution

Obtaining the 3D density profile from the integrated density is a deconvolution problem which, in general, has no unique solution. In our case we can exploit a symmetry to restrict the problem to have one solution only. We will see in the next chapter that, in our experiment, the trapping potential, and therefore the cloud density, is cylindrically symmetric along a direction perpendicular the imaging one.

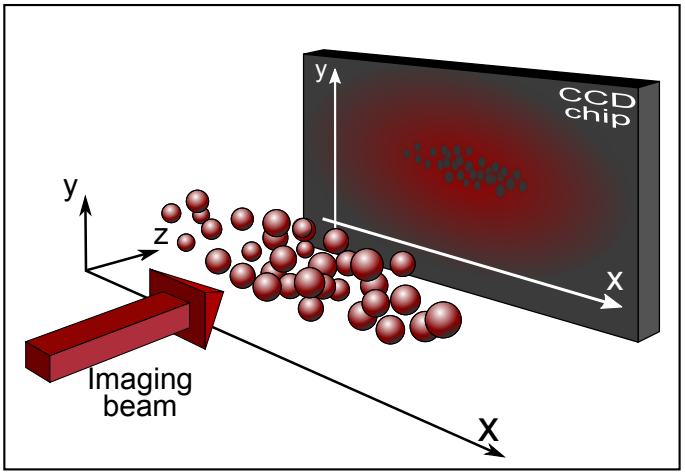

Figure 2.7: *Sketch of the absorption imaging working principle. The measured optical density is proportional to the integrated 3D density along the imaging beam direction. Since we need the 3D density to obtain $n(U)$ Abel deconvolution is required.*

It is exactly this symmetry that allows us to reconstruct the 3D density profile. The tomography of cylindrically symmetric objects was, in fact, analytically solved by Abel [32] in the nineteenth century:

$$n_{3D}(x,\rho) = -\frac{1}{\pi}\int_r^\infty \frac{dn_{2D}(x,y)}{dy}\frac{dy}{\sqrt{y^2-r^2}}, \tag{2.18}$$

where the 3D density profile is expressed in cylindrical coordinates and where we have assumed that $n_{3D}(x,\rho)$ drops to zero more quickly than $1/\rho$ as $\rho \to \infty$.

Although we have this analytical solution to our problem, the generalization to discrete data points is not straightforward, in particular in the presence of noise. This is due fundamentally to the fact that:

- In order to apply this deconvolution method to an actual image we need to convert the integration into a summation and this leads to a divergence every time $y = r$.
- The equation contains a derivative, and this is quite a big problem if data points are noisy (for a deeper discussion on this topic see Appendix A).

In order to deal with these problems one can use one of the several numerical algorithm available in the literature: Dasch [33] describes the three point Abel deconvolution, onion-peeling and filtered back-projection methods, Ma [34] the Fourier-Hankel method and Dribinski [35] the BASEX method. The choice of the best method can change depending on specific properties of data such as noise level and image dimension. The method we adopted is described in section 4.1.1.

This approach of experimentally study the thermodynamic of a unitary Fermi gas is used for the first time by Zwierlein's group in MIT [5]. It is worth to mention that there is an alternative approach to study this kind of thermodynamic without relying on the Abel deconvolution and working directly with integrated quantities. This is done in Paris by Salomon's group [3] [36].

Chapter 3

Experimental Setup

We describe the experimental sequence to cool to quantum degeneracy clouds of fermionic ^6Li atoms trapped in two spin states by evaporating the gas in an optical trap at the Fano-Feshbach resonance. At the crossover we produce a strongly interacting (eventually superfluid) Fermi gas of about 10^5 atoms per spin state. We will give particularly attention to the experimental characterisation of the trapping potential and to the absorption imaging technique used to measure the in-situ atomic density profile. We address also the imaging limitations (i.e. resolution, noise and blurring due to photon recoil during the imaging pulse) that can affect the reliability of the experimental density profile. The knowledge of the potential and the density profile are indeed the fundamental blocks on which we construct the procedure to extract the equation of state of the (superfluid) fermionic gas.

3.1 Li-6 properties

Lithium-6 is widely used in ultracold atoms experiment because of its extremely broad Feshbach resonances (compared the the other alkali) that allow a unique control of the interaction between particles. That is why it is the best system to study the physics at the BEC-BCS crossover [1].

The optical spectrum of lithium contains a prominent spectroscopic features called D-line. This line corresponds to the transition between the ground state 2^2S and the exited state 2^2S. The D-line is actually composed by two fine structure lines D_1 and D_2, where the splitting is given by the spin-orbit interaction:

$$H_{s.o.} \sim \vec{L} \cdot \vec{S}, \tag{3.1}$$

Consider also the coupling with the nuclear spin, one finds an additional splitting known as *hyperfine structure*:

$$H_{HF} \sim \vec{J} \cdot \vec{I}, \tag{3.2}$$

where $\vec{J} = \vec{L} + \vec{S}$. We report the result of those interactions in the level diagram in figure 3.1.

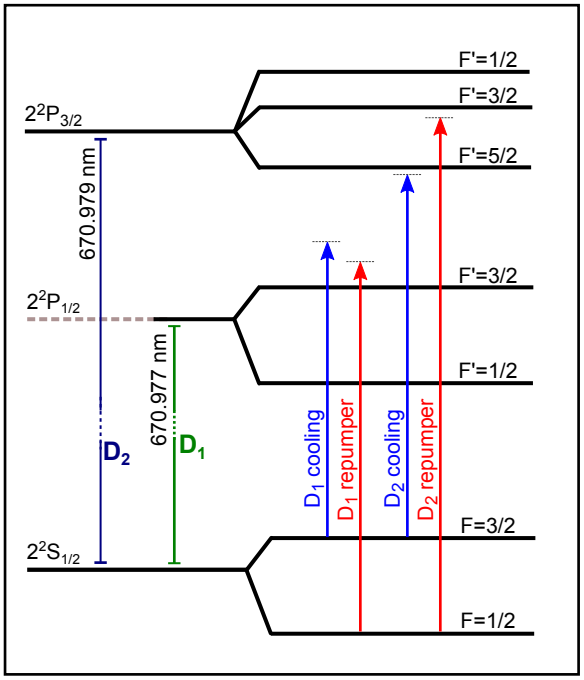

Figure 3.1: *Scheme of the D_1 and the D_2 transition in ^{6}Li. On the right side the hyperfine splitting. In light blue and light red the transitions used for grey molasses cooling [37].*

During the experiment we introduce the Feshbach magnetic field, therefore, we have to consider the Zeeman shift of the energy levels due to the interaction between this field and the the total spin of the atom. The typical used magnetic field ($B \geq$ 500G) is high enough to completely decouple $\vec{I}$ and $\vec{J}$. The shift induced by B is dominant with respect to the hyperfine one and can be written as:

$$\Delta E \simeq \frac{\mu_B}{\hbar} g_J m_J B \tag{3.3}$$

We plot the energy shift as a function of the magnetic field in figure 3.2.

3.2 Laser cooling of ^{6}Li atoms

Our experimental sequence starts with loading a magneto-optical trap (MOT) operating on the D_2 optical transitions ($2S_{1/2} \rightarrow 2P_{3/2}$) as shown in figure 3.1. We typically collect about 10^9 atoms at about 500 μK. The temperature in this phase is limited by the absence of efficient sub-Doppler cooling due to the unresolved hyperfine splitting of the excited states. In our experiment we have recently developed a new and efficient sub-Doppler scheme based on grey molasses which exploits D_1 ($2S_{1/2} \rightarrow 2P_{1/2}$) transitions (for details see [37]). This mechanism relies the presence of dark states which are populated by choosing the opportune relative ratio

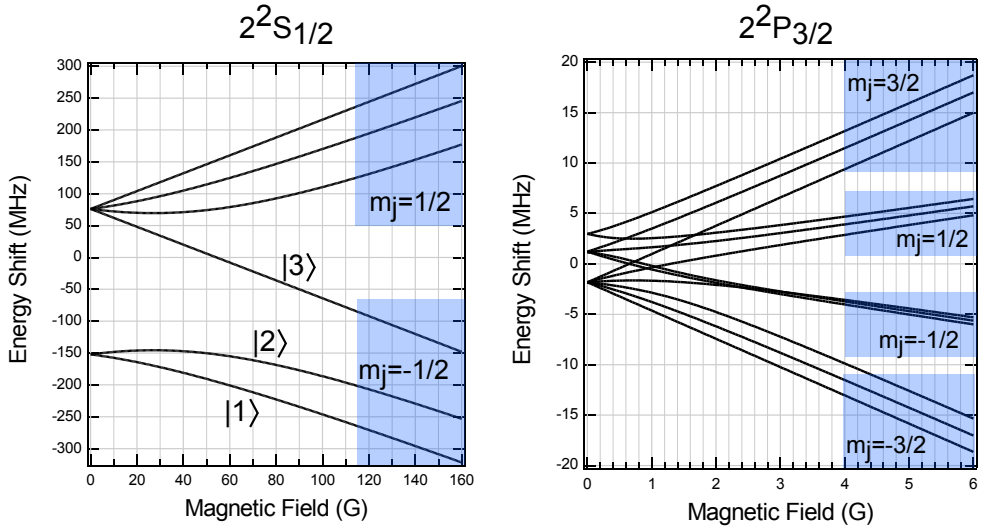

Figure 3.2: *^{6}Li energies shift of $2^2S_{1/2}$ level (on the left) and $2^2S_{1/2}$ level (on the right), as a function of the magnetic field. After the grey molasses cooling stage the atoms populates the $|1\rangle$ and $|1\rangle$ of the $2^2S_{1/2}$ level [37]. The imaging transition goes from $|1\rangle$ (on the left) to the unresolved triplets $m_j = -3/2$ (on the right). For clearness the shifts are plotted up to a value of magnetic field of 160 G and 6 G but the actual imaging takes place at 832 G.*

and relative frequency between cooling and repumper lights as shown in figure 3.1 In this way we can cool the lithium sample to about 40 μK in few ms. The fraction of cooled atoms is about 75% of the initial number. These are the ideal conditions to transfer the atoms in a conservative potential (optical dipole trap, ODT), where to perform the evaporation stage to quantum degenerate regimes. In the following I will briefly describe the main features of this kind of optical potentials.

3.2.1 Optical dipole trap

Optical dipole traps provide a spatial potential on atoms using a non-homogeneous laser radiation, detuned with respect to atomic transition. The oscillating electric field of the laser induces an oscillating electric dipole moment on atoms. This dipole moment interacts with the laser field itself and shifts the energy levels of the atoms (ac Stark shift or light shift [38]). Since this shift depends on the laser intensity and the laser intensity varies in space, also the shift varies and produce an effective spatial potential. When the laser frequency is detuned below the atomic resonance, red-detuning ($\delta < 0$), the atoms are attracted towards regions of maximum intensity of the laser field. On the contrary if the laser frequency is detuned above the resonance, blue-detuning ($\delta > 0$), atoms are attracted to regions of minimum intensity.

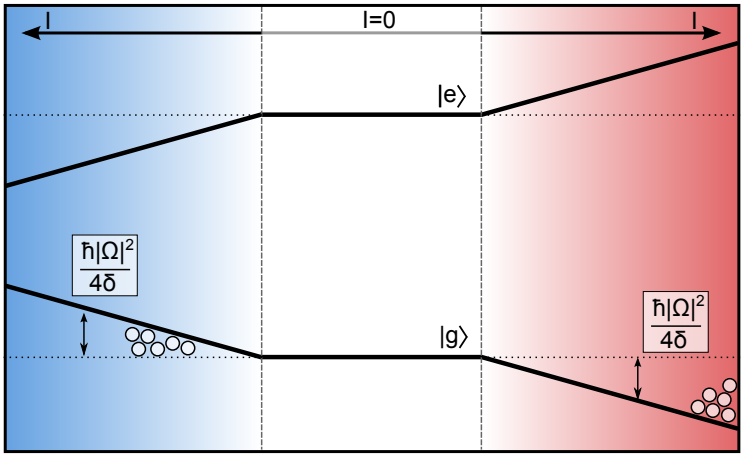

Figure 3.3: *Energy shift of the dressed states as a function of the intensity of the laser radiation. On the left blue detuned light ($\delta > 0$) corresponding to a repulsive potential: the atoms are pushed away toward the minimum of the intensity. On the right red detuned light ($\delta < 0$) corresponding to an attractive potential: the atoms are draw toward the maximum of the intensity.*

Light shift

We introduce here a simple derivation of the optical dipole potential following the dressed-state approach described by [38] and [39].

We consider the atom as a two level system coupled with the radiation field. The energy difference between the ground state $|g\rangle$ and the exited state $|e\rangle$ is $\hbar\omega_0$. We write the Hamiltonian of this system, under rotating wave approximation (RWA)[39], as:

$$\hat{H} = \begin{bmatrix} 0 & \frac{\hbar}{2}\Omega^* \\ \frac{\hbar}{2}\Omega & -\hbar\delta \end{bmatrix}, \tag{3.4}$$

where Ω is the Rabi frequency and $\delta = \omega - \omega_0$ is the detuning between the radiation frequency ω and resonance frequency ω_0. We can now diagonalize this Hamiltonian to study the stationary solution. The new eigenstates $|g'\rangle$ and $|e'\rangle$ can be written as a linear combination of the initial state:

$$\begin{bmatrix} |g'\rangle \\ |e'\rangle \end{bmatrix} = \begin{bmatrix} \cos(\beta) & \sin(\beta) \\ -\sin(\beta) & \cos(\beta) \end{bmatrix} \begin{bmatrix} |g\rangle \\ |e\rangle \end{bmatrix}, \tag{3.5}$$

where β is defined by $\cos(2\beta) = 1/\sqrt{1 + |\Omega|^2/\delta^2}$. In this base the new eigenstates have energies $\hbar(-\delta \pm \sqrt{\delta^2 + |\Omega|^2})/2$. If we consider the far-detuned regime ($|\delta| \gg$

Ω), those energy eigenvalue became:

$$\hat{H}' |g'\rangle = \frac{\hbar|\Omega|^2}{4\delta} |g'\rangle \tag{3.6}$$

$$\hat{H}' |e'\rangle = -(\hbar\delta + \frac{\hbar|\Omega|^2}{4\delta}) |e'\rangle , \tag{3.7}$$

where $\hat{H}'$ is the diagonal Hamiltonian written in the new base.

The magnitude of the coupling field is proportional to the laser intensity ($I \propto |\Omega|^2$) and therefore, for a Gaussian laser beam, depends on spatial position $\mathbf{r}$. Here we see the working principle of the dipole trap: we find that light induces on the atoms an energy shift proportional to the radiation intensity and, if the intensity is positionally dependent, we obtain a spatially dependent potential:

$$U_d(\mathbf{r}) = \frac{\hbar|\Omega(\mathbf{r})|^2}{4\delta} = \frac{e^2\mu_{eg}^2}{4\hbar\delta} E^2(\mathbf{r}) = \frac{e^2\mu_{eg}^2}{2\hbar\delta\epsilon_0 c} I(\mathbf{r}), \tag{3.8}$$

where μ_{eg} is the transition dipole moment and we considered the average field intensity $I = \epsilon_0 c E^2/2$. As we see from equation 3.8 the potential is proportional to the intensity of the laser beam and inversely proportional to the detuning with respect to D lines.

Gaussian laser beam

In our experiment we use only a single focused Gaussian red-detuned laser beam to obtain the desired intensity profile for the trap. We remind here some basic properties of gaussian beams. The intensity profile can be written as:

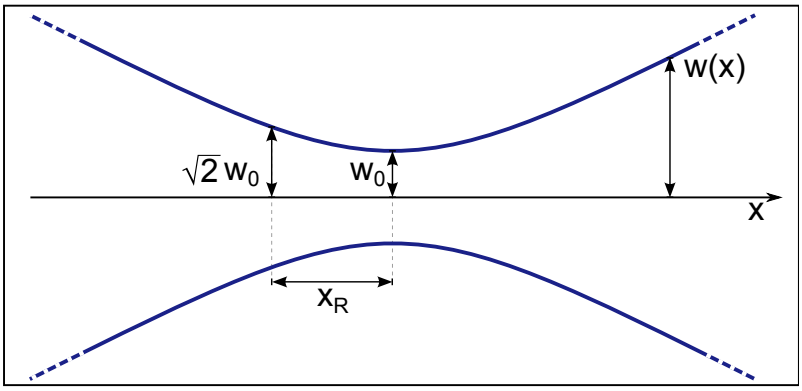

Figure 3.4: *Shape of a gaussian beam along the propagation direction. w_0 is the waist of the beam and z_R is the Rayleigh length.*

$$I(r,z) = I_0 \left(\frac{w_0}{w(x)}\right)^2 \exp\left[-\frac{2r^2}{w^2(x)}\right], \tag{3.9}$$

where r is the distance from the beam axis and x is the propagation direction. We have also defined the beam radius $w(x)$ and the waist w_0 as follow:

$$w(x) = w_0\sqrt{1 + \left(\frac{x}{x_R}\right)^2}, \tag{3.10}$$

where z_R is the Rayleigh length:

$$x_R = \frac{\pi w_0^2}{\lambda}. \tag{3.11}$$

λ is the radiation wavelength. The beam radius represents the distance from the beam axis where the intensity is reduced by a factor of e^2 and the waist w_0 is the smallest radius.

From the expression of intensity (3.9) we realise that our trapping potential is parabolic along the propagation axis and gaussian in the perpendicular plane.

3.2.2 Cooling to quantum degenerate regime

Our single beam optical dipole trap is generated by a 200 W multimode ytterbium fiber laser (IPG), with a central wavelength of 1073 nm. To create a large volume ODT we use elliptic shaped beam ($w_{0y} = 80$ μm, $w_{0z} = 42$ μm). The initial trap depth is of the order of $U_0 \sim 1$ mK, larger than the temperature of the atoms after the molasses to allow an efficient transfer from the MOT to the ODT. In particular, the number of atoms is of the order of 10^7 at a temperature of about 90 μK. The increase in temperature is mainly due to the compression of the atoms in the optical trap volume. The grey molasses scheme populates efficiently the $F = 1/2$ manifold, i.e. the $m_F = \pm 1/2$ [37]. In the following we name these states as $|1\rangle$ and $|2\rangle$. For these two internal levels exists a broad Feshbach resonance centred at about 832 G as shown in figure 3.5.

A pair of coils produces the uniform magnetic field up needed to approach the resonance. The magnetic field is calibrated by radio-frequency spectroscopy and it is actively stabilised by retroactive PID control at the level of $\sim 5 \times 10^{-5}$ at 830 G. To enter the degenerate strongly interacting regime we evaporate the $|1\rangle$-$|2\rangle$ spin mixture at the resonance by lowering in a controlled way the ODT trap depth decreasing the laser intensity. Just after the first part of the evaporation we superimpose a weaker additional laser beam crossing the IPG one at about 12.75°. This laser is a Nd-YAG Mephisto, single mode, operating at 1064 nm, focused on the sample with a beam waist of 42 μm. The contribution of the Mephisto is marginal at the beginning of the evaporation, while at the end it is the only optical potential for the atoms, being the IPG intensity is diminished to zero. In addition to the optical trap we superimpose a magnetic curvature to provide the necessary harmonic confinement along the Mephisto beam propagation, where the optical confinement is negligible. The characterisation of the full potential, which is

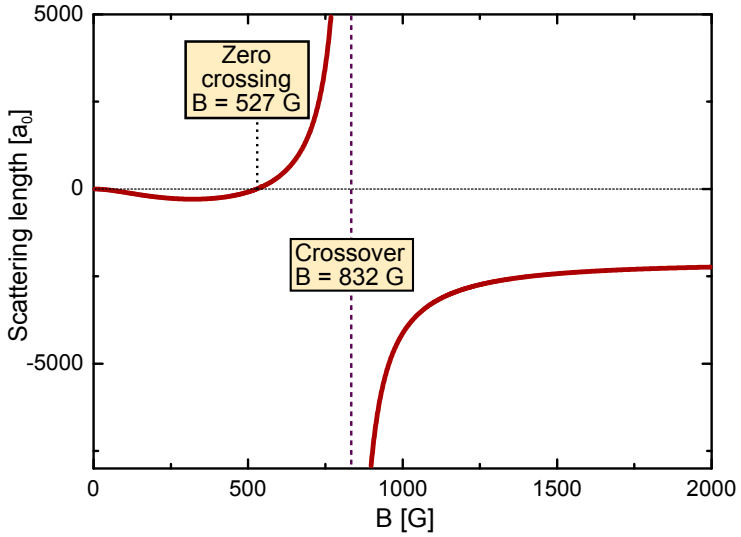

Figure 3.5: *^{6}Li scattering length across the Fano-Feshbach resonance between the levels $|1\rangle$ and $|2\rangle$. A magnetic field $B = 832$ G, corresponding to the resonance, is used to produce the unitary Fermi gas ($a \to \infty$). A magnetic field $B = 527$ G, corresponding to the zero-crossing, is used to produce an ideal Fermi gas ($a \to 0$). Data points are taken from [40].*

one of the key ingredients to obtain the equation of state, fill be described in detail in the next section.

After about 6 seconds of evaporation we typically produce degenerate Fermi gases of 4×10^5 atoms at $T/T_F < 0.1$. As we have seen in the first chapter there are three different regimes that can be explored across the Feshbach resonance, the BEC, the BEC-BCS crossover and the BCS side. In this thesis we focus our attention to the unitary and to the non-interacting Fermi gas. The latter is achieved by reducing the interaction in the $|1\rangle$-$|2\rangle$ spin mixture setting the Feshbach magnetic field at the zero-crossing of the Feshbach resonance. In figure 3.6 we show an example of unitary Fermi gas of about $\sim 4 \times 10^5$ atoms. The typical size of the cloud is of the order of half a mm in the longitudinal direction and about 40 μm in the radial one. One last remark: in the case of the unitary gas we can not extract the temperature with standard technique (i.e. from the momentum distribution) due to strong interaction. We can estimate the degree of degeneracy of the cloud considering that, for the same final trap depth, we observe a BEC of molecules if we evaporate the gas at 700 G (molecular regime). At this magnetic field, the interactions are strongly reduced and therefore we can directly obtain the ratio T/T_C measuring the fraction of thermal atoms with respect to the condensed one the analysis of the cloud after time-of-flight. This is why is relevant to develop an alternative technique to extract the temperature in the unitary regime. In the next chapter, we will indeed present our results based on the virial theory applied on the experimental density profiles of the strongly-interacting Fermi gases that eventually allows us to determine the

temperature of the system.

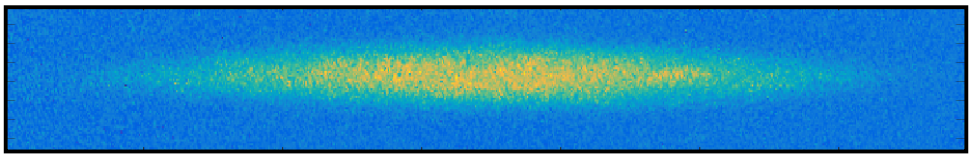

Figure 3.6: *Example of density profile of the unitary Fermi gas obtained with absorption imaging.*

3.2.3 Potential characterization

In the previous chapter we have seen how we can obtain the local pressure and the local compressibility of the atomic cloud respectively integrating and derivating the density profile, n, with respect to the final potential U, seen by the atoms at the end of the evaporation. Therefore an accurate characterization of the trapping potential is fundamental in order to obtain $n(U)$.

We use basically two methods to estimate this potential depending on the direction:

- Trap oscillation frequency (used along the direction of the ODT beam: $\hat{x}$).
- Imaging of the section of optical dipole trap beam (used along the directions perpendicular to the ODT: $\hat{y}, \hat{z}$).

Along the direction of the optical dipole beam the trapping potential is fundamentally given by the magnetic residual curvature of the Feshbach coils and by a small contribution from the ODT curvature. This potential is harmonic in a very good extent. Because of this we can characterise the potential using the oscillation frequency of the centre of mass of an atomic cloud.

In practice we introduce a displacement in the position of the cloud using an one other red-detuned laser (IPG). When we turn this laser off the cloud begins to oscillate in the trap. In order to estimate the oscillation frequency we repeat this procedure many times, changing the delay between the moment we turn off the IPG laser and the moment we image the cloud. For each image obtained this way we fit the position of the centre off mass of the cloud and we plot the results as a function of the time delay in figure 3.7. We then estimate the oscillation frequency, ω_x, fitting the data with a sine function[1]. The trapping potential is finally given by:

$$U_x(x - x_0) = \frac{1}{2} m \omega_x (x - x_0)^2, \tag{3.12}$$

[1] The fit function we use includes also a damping term, in order to take into account dissipation effects. This term does not affect the frequency we obtain as fit result.

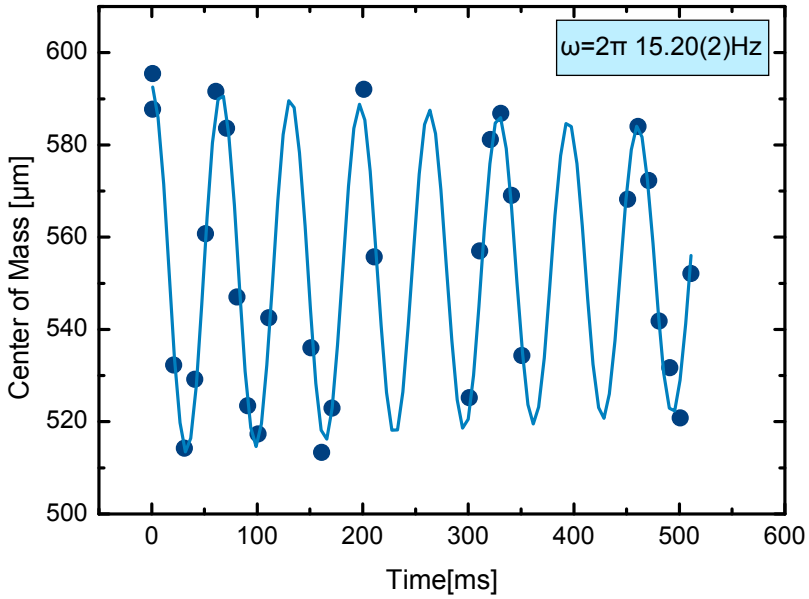

Figure 3.7: *Example of oscillation of the centre of mass of an atomic cloud inside an harmonic potential. On the x-axis the delay between the moment the atoms are released and start to oscillate and the imaging pulse. The data point are fitted with a dumped sine function and the resulting frequency is* $\omega = 2\pi 15.30(2)$ *Hz.*

where x_0 is the position of the centre of the trap.

Concerning the directions $\hat{y}$ and $\hat{z}$ the potential is given by the optical dipole trap and an harmonic model like the one described above is not accurate any more. This is due to the fact that the size of the cloud is now comparable with of the waist of the ODT beam.

For this reason we measure both the power and the waist of the beam, characterising it completely. In order to do this, we deviate it before the vacuum chamber and, using a power-meter we measure its power and, using a CCD camera, its waist. We obtain a waist of $w_{0y} = w_{0z} \simeq 42\mu$m and a power of $P_{\text{meph}} \simeq 9.5\text{mW}$[2]. Given these two parameter we can write the expression of the potential in cylindrical coordinates:

$$U_{rad}(\rho) = \frac{2A_{\text{meph}}P_{\text{meph}}}{\pi w_\rho} \exp\left(-\frac{2\rho^2}{w_\rho^2}\right), \tag{3.13}$$

where $\rho^2 = y^2 + z^2$, $w_\rho = w_y = w_z$ and A_{meph}[3] is the proportional coefficient between

[2] We do not consider here spurious but present effects such as aberration and residual reflection of the optical components that may affect this measurement. They will be kept into account in the chapter 5 when discussing about source of errors in our procedures.

[3] This coefficient is calculated considering both the D_1 and the D_2 line. We can write it as:

$$A_{\text{meph}} = -\frac{\pi c^2 \Gamma}{2}\left(\frac{1}{\omega_{D_1}^3 \delta_{D_1}} + \frac{2}{\omega_{D_2}^3 \delta_{D_2}}\right), \tag{3.14}$$

the trapping potential and the intensity of the beam we obtained in equation 3.8.

We finally consider the total trapping potential to be the sum of those two:

$$U(x,\rho) = \frac{1}{2}m\omega_x^2(x-x_0)^2 + \frac{2A_{\text{meph}}P_{\text{meph}}}{\pi w_\rho}\ \exp\left(-\frac{2\rho^2}{w_\rho^2}\right). \tag{3.15}$$

A representation of this potential is shown in figure 3.8. From the equation 3.15 we can estimate the depth of the trap to be $\sim$ 200nK.

Figure 3.8: *Example of trapping potential. Along the x-axis the confinement is given my the harmonic magnetic curvature. Along the radial direction (y-axis in the figure) is given my the optical dipole trap.*

3.3 Imaging

In this section we describe the imaging technique we use to extract the density information from the atomic cloud. We start with a general overview of the absorption imaging technique. Than we show how we calibrate the magnification and the optical density in order to measure a reliable number of atoms. Finally we describe the Fast Kinetic Series (FKS), a special acquisition mode of our CCD camera (EMCCD Andor iXon3). FKS allows to use only a partial region of CCD chip, in order to drastically reduce the time delay between consecutive acquisition, reducing, in this way, also the fringes-like artefacts normally produced by absorption imaging.

3.3.1 Absorption imaging

Absorption imaging is by far the most popular imaging technique used in ultracold atoms experiments. Its working principle, sketched in figure 3.9, is very simple: the atom cloud is shined with a resonant laser beam. Part of the light is absorbed by the cloud and it is re-emitted, in a random direction, because of spontaneous emission. As a result, there is a net diminishing of the light intensity along the beam direction and this loss is proportional to the number of atoms along the path of the beam. In practice the atoms cast a shadow on the imaging beam that we can image using

where $\hbar\omega_{D_i}$ is the energy of the D_i transition and $\delta_{D_i} = \omega_{D_i} - \omega_{meph}$ is the detuning between the frequency of the D_i transition and frequency of the laser light we use to produce the dipole trap.

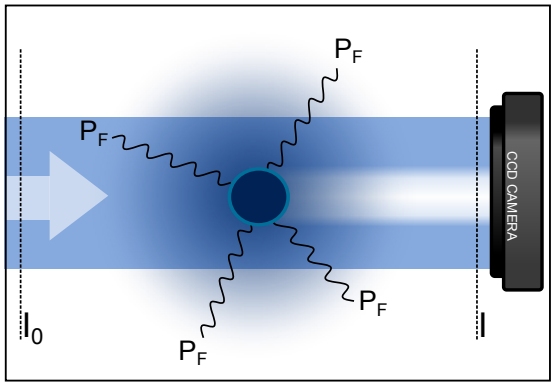

Figure 3.9: *Representation of the working principle of the absorption imaging. The laser beam, passing through the atomic cloud, is attenuated as a function of the optical density and casts a shadow on the CCD camera.*

a CCD camera. An image obtained this way contains the information of the cloud density, integrated along the direction of propagation of the beam.

More quantitatively we can model the problem as follow: we consider the atoms as a two-level system coupled with the radiation field of the imaging light. Within this approximation we can write the amount of power lost by the imaging beam because of absorption and spontaneous emission:

$$P_F = \hbar\omega_0 N \tilde{\rho}_{ee} \Gamma, \tag{3.16}$$

where $\hbar\omega_0$ is the energy of a fluorescence photon, N is the total number of atom, $\tilde{\rho}_{ee}$ is the excited fraction[4] and Γ is the rate of spontaneous emission. Using the steady-state expression for $\tilde{\rho}_{ee}$, we can write the fluorescence power as [39]:

$$P_F = \frac{\hbar\omega_0 N\Gamma}{2} \frac{s}{s+1} \frac{1}{1+\left(\frac{2\delta}{\Gamma_s}\right)^2} \overset{\text{resonant light}}{\rightarrow} \frac{\hbar\omega_0 N\Gamma}{2} \frac{s}{s+1}. \tag{3.17}$$

In this expression we introduce the saturation parameter s, the saturated linewidth $\Gamma_S = \Gamma\sqrt{1+s}$ and the detuning δ. From now on we will consider the case of resonant light $\delta \to 0$. The saturation parameter is strictly linked to intensity by the following equation:

$$s = \frac{I}{I_s}, \tag{3.18}$$

where I_s is the saturation intensity:

$$I_s = \frac{\hbar\Gamma\omega_0^3}{12\pi c^2}. \tag{3.19}$$

[4] $\tilde{\rho}_{ee}$ is obtained studying a two-level system (atomic cloud) interacting with an external field (oscillating electric field). The results are the famous Maxwell-Bloch equations (or optical Bloch equations). An extensive derivation of those equation can be found in the Appendix A of [39].

For small intensities ($s \ll 1$) the fluorescence increase linearly with s. For high intensities ($s \gg 1$), P_F saturates to $\hbar\omega_0 N\Gamma/2$. In this limit the population of excited state is equal to the population in the ground state and increasing the intensity does not have any effect, since absorption and stimulated emission are balanced.

In order to find an expression for the intensity of the beam after the atoms, we consider that, at equilibrium, the rate of absorbed and re-emitted energy must be the same because of energy conservation. The decrease of intensity given by a propagation of length dz inside the gas is:

$$dI = -\frac{P_F}{\Sigma} = -\hbar\omega_0 \frac{N}{\Sigma}\frac{\Gamma}{2}\frac{s}{s+1} = -\sigma n I dz, \tag{3.20}$$

where Σ is the interaction cross section, n the number of atoms per unite volume and σ the photon scattering cross section. In the low intensity regime, σ does not depend on intensity, but only on the transition frequency:

$$\sigma = \hbar\omega_0 \frac{\Gamma}{2I_s} = \frac{6\pi c^2}{\omega_0^2} \tag{3.21}$$

Equation 3.20 can be integrated to obtain:

$$I(z) = I_0 \exp\left(-\sigma \int_{-\infty}^{\infty} n_{3D}(x,y,z)dz\right), \tag{3.22}$$

where I_0 is the intensity before the atomic cloud. Applying a natural logarithm to both sides of this equation we finally obtain an expression for the column density of the cloud:

$$n_{2D}(x,y) = \int_{-\infty}^{\infty} n_{3D}(x,y,z)dz = \frac{1}{\sigma}\ln\left(\frac{I_0(x,y)}{I(x,y)}\right). \tag{3.23}$$

In order to experimentally obtain n_{2D} we need to take two different images: the first one with the atoms, in order to obtain $I(x,y)$, and the second without, to measure the intensity profile of the beam $I_0(x,y)$. In practice it's also useful to take a third image, the background, with the imaging beam turned off. This allows us to subtract the contribution of unwanted external light and part of electronic noise of the camera. In the low saturation limit[5] the density profile is then:

$$n_{2D}(x,y) = \frac{1}{\sigma}\ln\left(\frac{I_{no\,atoms}(x,y) - I_{background}(x,y)}{I_{atoms}(x,y) - I_{background}(x,y)}\right). \tag{3.24}$$

3.3.2 Imaging apparatus

After all the cooling process the atomic cloud is trapped in the centre of a vacuum chamber as we show in figure 3.10. The imaging beam enters from the bottom

[5] A more general case, where intensity I is not completely negligible with respect to the saturation intensity I_s, will be discussed in the section 3.3.6. We will see how this is important for a correct measurement of the number of atom in the cloud.

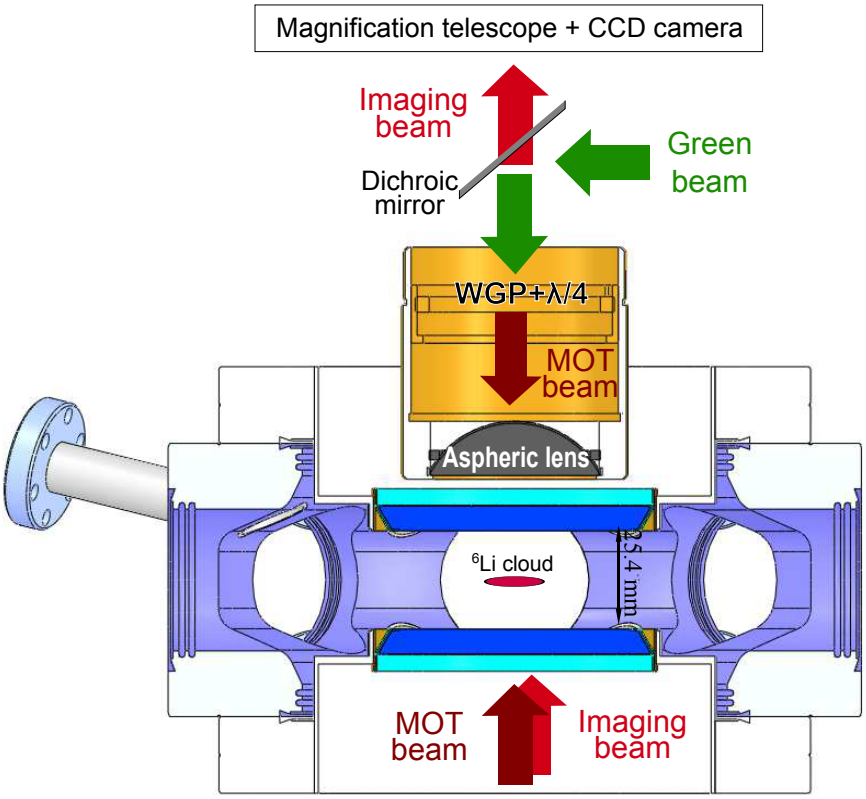

Figure 3.10: *Sketch of the first part of the imaging apparatus. The MOT beam and the imaging beams enters the vacuum chamber from the bottom. The light is then collected by an aspheric lens and the shadow of the atoms is collimated toward the magnification telescope and the CCD camera. The MOT light is reflected by the combination of a wire grid polariser (WPG) and a $\lambda/4$ waveplate. On the top a dichroic mirror allows to superimpose additional potential to the atomic cloud.*

window of the cell and illuminates the atomic gas. The shadow produced by the cloud is then collected by an aspheric lens and collimated towards the magnification telescope and finally imaged using a CCD camera. After the aspheric lens, in order to separate the imaging light from the retro-reflected MOT beam, we placed a wire grid polariser, or WGP, (700μm thick) and a $\lambda/4$ waveplate (250μm thick). After those, we also placed a dichroic plate which allows us to superimpose, to the imaging beam, a green laser beam that is eventually used to add a supplementary controllable potential to the atomic cloud[6].

The imaging beam pass this dichroic plate with negligible losses and it pass through a telescope that magnifies the shadow of the cloud by a factor of 12.5. Finally it gets to the end of the imaging apparatus, which is the CCD camera, where the intensity profile of the beam is acquired.

The imaging beam is obtained with a solid state diode laser that emits at 670 nm. The wavelength is then finely shifted with a series of acousto-optic modulator (AOM) in order to be resonant with the imaging transition, i.e. from the lowest hyperfine state of the $2^2S_{1/2}$ level, $|1\rangle$, to the unresolved triplet $m_j = -3/2$ of the $2^2P_{3/2}$ level (see figure 3.2).

Andor CCD camera

In our experiment we use an Andor iXon3 X-9260 CCD camera. Its main feature is that the CCD chip can be cooled up to $-90°$C. This drastically reduce the dark current noise, both during the acquisition of the image and during the readout process[7]. We report in the following table some technical details of this camera:

Andor iXon3 X-9260	
Model number	CCD201-20-1-179
Pixels number	1024×1024
Pixel dimension	$13\mu\text{m} \times 13\mu\text{m}$
Sensitivity (electrons per A/D count)*	4.22
Single pixel noise (electrons)*	9.2
Vertical clock speed	$(1.9 \div 9)\mu$s/pixel
Horizontal read-out speed	$(1 \div 10)$MHz

(*)Sensitivity and single pixel noise are given for the specific settings we use in our experiment: the conventional amplifier is use instead of the default electron multiplier amplifier (EM) and the pre-amplifier is disabled. The used read-out rate is 1MHz. We opt for all those settings in order to maximise the signal to noise ratio in our images.

[6] At the moment this supplementary potential consists in a blue detuned laser used to create a repulsive thin barrier in the centre of the cloud in order to study transport properties of a superfluid quantum gas.

[7] At the beginning of the work of this thesis we didn't have this camera already and we used a Stingray camera instead (AVT Stingray F-145B) . The images taken with this camera were too much noisy in order to reconstruct the equation of state.

Imaging pulse

Choosing good values for imaging beam intensity and duration is crucial to have a faithful density profile. While from one side we want to increase both intensity and duration of the imaging pulse, to have a better signal to noise ratio, on the other hand, higher intensity bring us away from the low saturation regime, so we have to consider additional terms (see section 3.3.6, equation 3.24). Second, higher pulse time means that, during the imaging, atoms have time to move from the original position because of the recoil due to spontaneous emission of photons thus modifying the measured density profile. To estimate this effect we consider an atom initially at rest. Since, at the end, the obtained density profile is integrated along the beam direction, we neglect the movement of atoms along this axis and we focus on the other two directions. Since the photon is re-emitted in a random direction, also the momentum gained by the atom points in a random direction. To estimate the expectation value of the velocity, in module, gained by an atom during the imaging pulse, we consider that the velocity itself undergoes to a random walk. Using this Brownian motion model we can write the average velocity [41]:

$$\tilde{v} = \frac{\hbar k}{m}\sqrt{\frac{N_{ph}}{3}}, \tag{3.25}$$

where $k = 2\pi/\lambda$ is the imaging light wave vector, m is the mass of the atom and N_{ph} is the number of re-emitted photons:

$$N_{ph} = \frac{\Gamma}{2}\frac{s}{s+1}t_{pulse} = \frac{\Gamma}{2}\frac{I}{I+I_s}t_{pulse}, \tag{3.26}$$

where we used equation 3.17 and we considered a square imaging pulse of time t_{pulse}. One can now estimate the spatial blurring Δx:

$$\Delta x = \tilde{v}t_{pulse} = \frac{2\pi\hbar}{\lambda m}\sqrt{\frac{\Gamma}{2}}\sqrt{\frac{I}{I+I_s}}\,t_{pulse}^{3/2}. \tag{3.27}$$

In our experiment $m_{Li} \simeq 9.99 \times 10^{-27}kg$, $\Gamma \simeq 5.87MHz$, $\lambda \simeq 671nm$ and $I_s \simeq 2.54W/cm^2$. Since we use $I \sim 2I_s$, we need to keep the pulse duration around $5\mu s$, in order to confine the blurring effect in a region of $\sim 1 \div 2\ \mu m$, that is comparable with the imaging resolution[8] (see section 3.3.4). In figure 3.11 we show the effect of this blurring as a function of the imaging pulse duration for different intensities of the imaging beam.

[8] In our experiment the atomic cloud is $\sim 800\mu$m long and $\sim 80\mu$m wide.

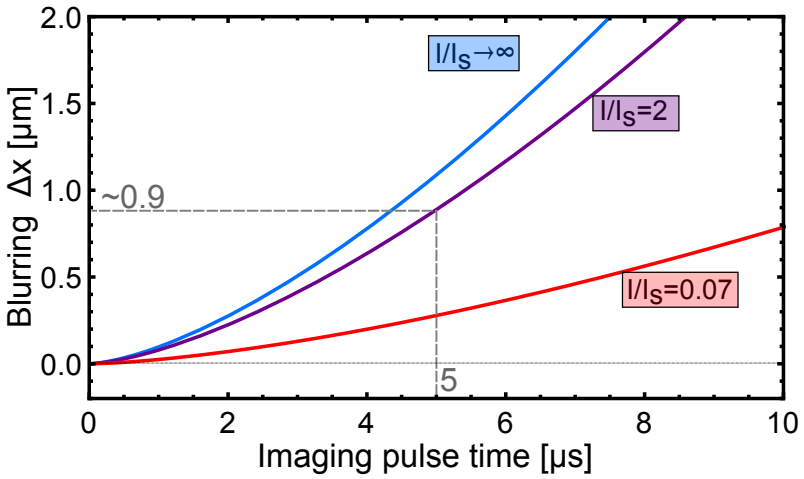

Figure 3.11: *Estimation of the blurring radius due to the random walk caused by the spontaneous emission, as a function of the imaging pulse time. Different lines represent different condition of saturation parameter. The dashed grey line represents our experimental condition, with an imaging pulse of $5\mu s$ that correspond to a blurring of $\sim 0.9\mu m$.*

3.3.3 Calibration of the magnification

The magnification of the imaging system can be roughly estimate considering that there are basically two telescope between the atoms and the CCD sensor. In figure 3.12 we show the experimental scheme of the imaging. As we can see the first telescope is composed by two lenses of $f_1 = 32$ mm and $f_2 = 250$ mm, giving a first magnification factor of $M_a \sim 7.8$. The second has $f_3 = 150$ mm and $f_4 = 250$ mm therefore it contributes with a factor of $M_b \sim 1.7$. The total magnification of the system is than the product of those two: $M_{TOT} \sim 13$.

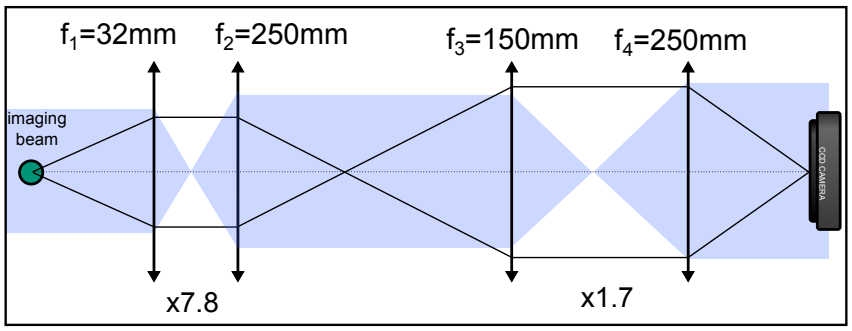

Figure 3.12: *Scheme of the magnification telescope. The green dots represent the atomic cloud, the light blue shape represents the optical path of the imaging beam and the black lines the optical path of the image of the atomic cloud shadow. The magnification factor is ~ 13.*

A more precise estimation of the magnification is performed exploiting the fact that we can move the position of the atomic cloud in a very controlled way. The movement is possible thanks to the fact that the final lens of the optical dipole trap (ODT) beam is mounted on a micrometrical translational stage. As shown in figure 3.13 a transversal displacement of this lens allows a fine movement of the beam.

First of all we calibrate this movement with respect to the lens displacement. This is done deviating, using a mirror, the beam before the vacuum chamber and placing a CCD camera[9] in the beam waist as shown in figure 3.13. Since we know the pixel size of the CCD chip to be 5.2μm we are able to measure the position of the waist as a function of the displacement we read in the translational stage micrometrical screw. We plot the results in figure 3.14 and, since the relationship between those two quantities is linear in good approximation, we estimate the calibration factor with a linear fit finding: $c_1 \simeq 1.0696$.

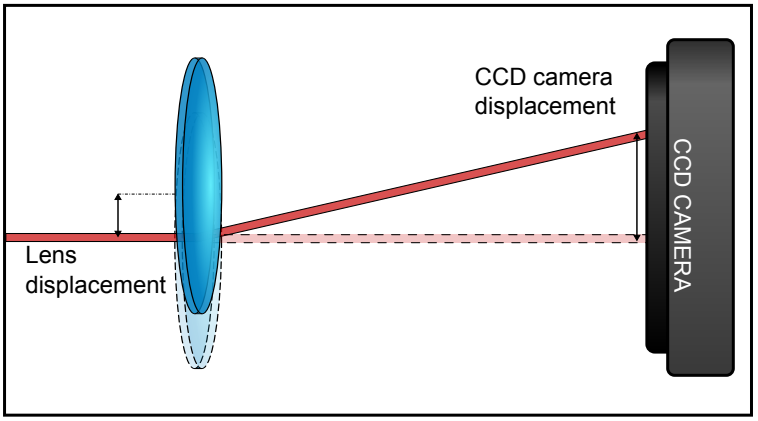

Figure 3.13: *Sketch of the procedure used to estimate the magnification of the imaging. A very controllable displacement of the last lens (on the right) along the ODT beam path allows us to finely move the position of the beam itself. The movement of the beam if first calibrate without the magnification telescope and then, reintroducing the telescope, used to estimate the magnification factor.*

Using this calibration we can determine the magnification of the actual imaging system. This is done by exploiting the fact that the trapped gas itself is positioned in the minimum of trapping potential: the ODT beam waist. We measure the position of the centre of the cloud, estimating it with a gaussian fit, as a function again of the ODT lens displacement. Again we find a linear dependence, figure 3.14, with a slope of: $c_2 \simeq 13.26$. Finally the ratio between c_1 and c_2 gives out the magnification factor of our imaging system:

$$\boxed{M_{\mathrm{TOT}} = \frac{c_2}{c_1} \simeq 12.4.} \tag{3.28}$$

[9] We used a Thorlabs camera model DCC1545M.

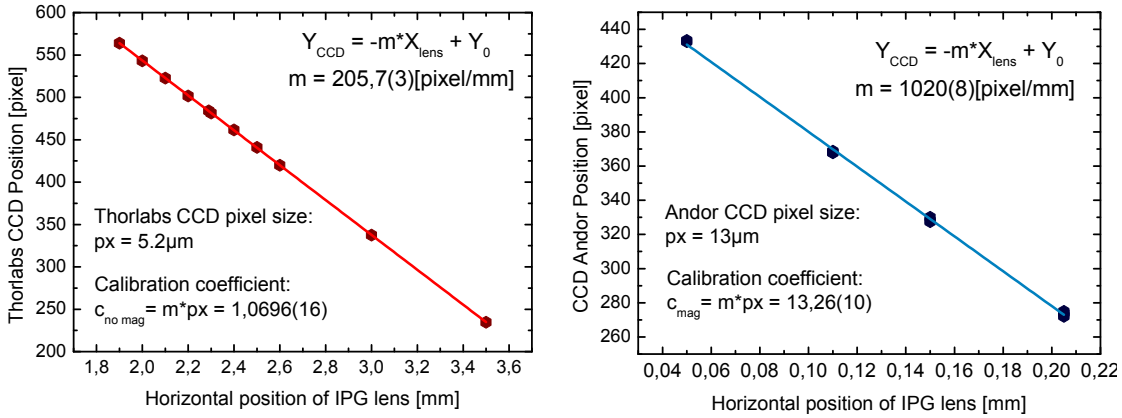

Figure 3.14: *On the left the calibration of the position of ODT beam as a function of the displacement of the final lens in the ODT beam path. On the right the same measure where we have introduced the magnification telescope. In both cases the dependence is liner and is fitted using a straight line. The ratio between the angular coefficient estimated on the right and the one estimated on the left gives the magnification of the imaging system.*

3.3.4 Imaging resolution

A raw estimation of the resolution of our imaging system can be done considering the diffraction limit of the aspheric lens which collect the imaging beam after the vacuum chamber (see figure 3.10). The dimension of the smallest observable point is given by the radius of the Airy disc [42]:

$$\Delta R \simeq \frac{0.61\lambda}{\mathrm{NA}}, \tag{3.29}$$

where λ is the wavelength of the imaging light and NA the numerical aperture. The lens we use is a plano-convex lens (AL4532) with a numerical aperture of NA $\simeq$ 0.61. The theoretical resolution is then $R \simeq 0.6\lambda/\mathrm{NA} \sim \lambda = 670$ nm. In practice one should consider also the finite size of the imaging beam and the imperfections of the lens itself. A deeper analysis and an actual measurement of our imaging resolution, which can be found in [43], gives a result almost three time bigger than the theoretical one: $\Delta R \simeq 1.5\mu$m. This result is really positive since the atomic cloud has a typical dimension of $\sim 800 \times 80 \times 80\mu$m.

3.3.5 Fast Kinetic Series

In absorption imaging is very important to have a very short time delay between the first image, the one with the atoms, and the second, with only the imaging beam. This time should, in principle, be short with respect to the time scale of imaging laser fluctuations and of mechanical vibration of the experimental setup. This is important in order to avoid the formation of fringes-like artefacts due to a position

shift or intensity variation between the images. On the other hand, this time has to be sufficiently long to remove the atom from the beam before taking the second image we should record the intensity profile of the image without the atoms. In practice this is done, not only physically moving the atoms from the initial position, but also detuning the laser from the atomic transition[10]. This way the atoms does not interact with the radiation any more and the cloud is transparent to this out of resonance light.

In practice, the major limitation is usually given by the repetition rate of the CCD camera. Our CCD camera takes almost 0.4 seconds to read a full 1024×1024 matrix of pixels. Since we require a much shorter time we can't use the camera in a standard way. There are several way out to this problem; the one our camera provides is the so called Fast Kinetic Series (FSK). This option allows to drastically decrease the time delay between acquisitions at the expense of the height, in pixel, of the final image. As we show in fig 3.15, this technique consists in using only a

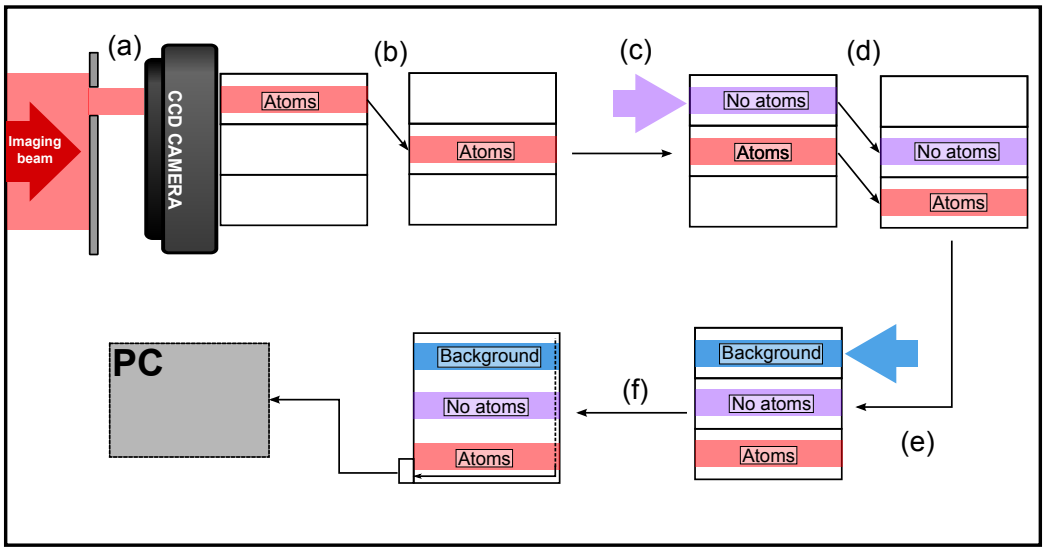

Figure 3.15: *Working principle of the fast kinetic series (FKS). In (a), (c) and (e) the CCD camera acquire the images. This exposure time is of the order of* $\sim 30\mu s$*. During (b) and (d) the electric charge in each pixel of the CCD is shifted down. This operation in our working condition takes* $\sim 210\mu s$*. This time impose a limit on the maximum frame rate one can use. In (f) the electric charge in each pixel is red and the information is sent to acquisition card of the computer. This last operation requires* $\sim$ *1s and limits the frequency of consecutive 3-images series.*

small portion of the CCD sensor for the actual imaging, while using the remaining region for storage. The great advantage comes from the fact that shifting vertically a row of pixels is very fast, compared with horizontal shift and read out time, which are the slowest steps between all the readout process. Our camera takes ~ 1.4 μs

[10] This is done changing the magnetic field.

to shift down a raw of pixels, this means that it's possible to acquire a sequence of 1024×150 pixels images, with a time delay of $\sim 210\mu$s.

During the exposure time, the whole CCD sensor is active, that is why we need to physically mask the storage region. In practice we place a slit, of about 2 mm width, consisting in two razor blades mounted on a rotational and translational stage, in the focal plane of the atoms (figure 3.16). In principle is also possible to put the slit in front of the CCD sensor but, for practical reasons, there is a gap between those two and this increase the diffraction pattern produced by the slit.

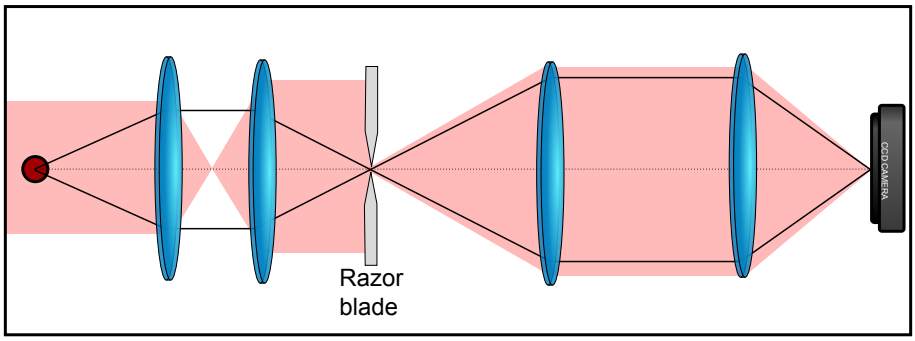

Figure 3.16: *Optical setup needed to use the fast kinetic series. A slit of about 250μm, assembled using two razor blade glued to a rotational and translational stage, is positioned in the focal plane of the images of the shadow of the atomic cloud. This is necessary in order to illuminate only a small section of the CCD camera chip.*

3.3.6 Number of atoms calibration

In chapter 5 we will show that a correct estimation of the number of atoms in the trap is very critical to the reconstruction of the equation of state. In this section we describe the major points one has to consider in order to get a correct calibration of the number of atoms with absorption imaging:

- The intensity of the imaging beam is not strictly in the low saturation regime $I/I_s \ll 1$. Because of this we need to add a correction term to equation 3.23 in order to compensate the reduction of optical density due to saturation.

- The polarization of the imaging beam can be not perfectly defined (circular or linear). This means that the power of the beam may not completely contribute to the absorption because of the selection rules of the used atomic transition. For example if we consider the transition $m_j = 1 \rightarrow m_j' = 0$, only a σ^- polarized photon can be absorbed. If the imaging beam is not fully circularly polarized there is a fraction of σ^+ polarized photons that don't interact with the atoms but are seen by the CCD camera. Since this alters the measured density should be also taken into consideration. One method to deal with this is introducing a corrective parameter and calibrate the imaging following [44].

- The imaging beam effectively pushes the atoms away from resonance because of the Doppler effect induced by the momentum gained by the atoms during the absorption. In order compensate it one can introduce a compensation factor (> 1). This is very important mostly in experiment, like our own, that uses light atoms, being the compensation factor proportional to the inverse of the mass.

We start describing a possible solution to the first two points following the method used by Reinaudi in [44]. In section 3.3.1 we derive the expression for the column density n_{2D} (eq.3.23), in the low saturation regime ($I \ll I_s$). Since in our experiment $I \sim 2I_s$, this equation does not hold any more and we need to generalize it as follow [44]:

$$n_{OD}(x,y) = \left[\log\left(\frac{I_0(x,y)}{I(x,y)}\right) + \frac{I_0(x,y) - I(x,y)}{I_{\text{sat}}}\right], \tag{3.30}$$

where we have introduced the optical density $n_{OD} = \sigma n_{2D}$. The second term in this equation is needed in order to compensate for the reduction of the optical density caused by the saturation of the transition.

In order to correct errors induced by the polarization of the imaging beam we can think that the optical density is a physical property of the atomic cloud, therefore, it can not depend on the imaging procedure itself. Practically we take advantage of this performing the measurement of the optical density changing the power of the imaging beam, finding this way a correction parameter we call α. The expression for the optical density with the correction parameter is than:

$$n_{OD}(x,y) = \alpha\left[\log\left(\frac{I_0(x,y)}{I(x,y)}\right) + \frac{I_0(x,y) - I(x,y)}{I_{\text{sat}}}\right]. \tag{3.31}$$

In order to find α one can take different images of a cloud, obtained always in the same experimental condition, changing the imaging beam intensity (I) and the imaging pulse duration (τ) but keeping the product $\tau \cdot I$ constant, in order to have always the same number of scattered photons. One can finally measure the peak of the optical density for each image taken this way for different values of α. The correct parameter α is then chosen to be the one that mostly keeps constant the peak in optical density calculated according to equation 3.31.

The last point one should consider is that during the imaging pulse, the atoms are pushed toward the propagation direction of the imaging beam because of the radiation pressure [38]. Every time an atom absorbs a photon it gains a recoil velocity which correspond, in the specific case of ^6Li, to a Doppler shift $\delta\omega \sim 2\pi \cdot 300$ kHz. Since the natural linewidth of the D_2 transition is $\Gamma \simeq 6$ MHz, an atom, after the absorption of a few photons, gains a sufficient velocity to put out of resonance the atomic transition with respect to the imaging radiation because of Doppler effect. The resulting effect is that, bigger is the number of absorbed photons during the imaging pulse, more the measured optical density underestimates the number of

atoms in the sample. Because of this we need to multiply the optical density by a correction factor which is proportional to the intensity of the imaging pulse and to its duration.

As we have seen the calibration of the number of atoms is a very complex and delicate task. At the moment the results we obtain using this method still has a rather big uncertainty and it is not completely reliable. For this reason we just use these results as starting point for the actual calibration, described in chapter 4. This calibration, suggested by Mark Ku (MIT) [5], is based on the comparison between the equation of state of a non-interacting Fermi gas, reconstructed experimentally, and the theoretical one we have calculated in section 1.5.2.

Chapter 4

Experimental results

We first describe in details the numerical recipe that we have developed in this thesis to extract the thermodynamics of an ultracold Fermi gas. Using this technique we obtain the equation of state of a strongly interacting unitary Fermi gas. The compressibility and the specific heat show a clear peak corresponding to the superfluid phase transition (in analogy with helium or superconductors). The critical temperature we estimate is of the order of $0.14(3)T_F$. *We will also describe a reliable method based on the virial expansion to determine the temperature of this strongly correlated Fermi gas, where standard thermometric technique fails due to strong the interactions. We can extract a value for the* b_4 *coefficient that is in qualitative agreement with the ones found in literature.*

4.1 Density and trapping potential

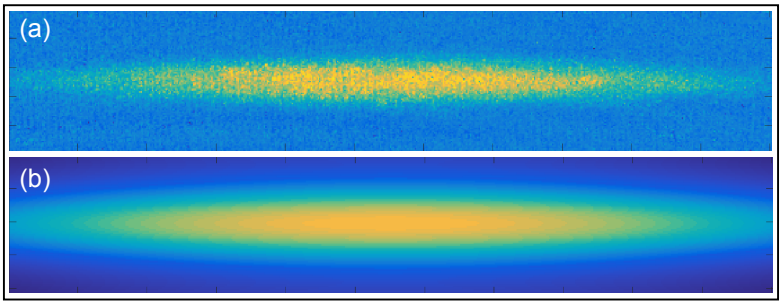

Figure 4.1: *Starting point for the data analysis. (a) Density profile from absorption imaging. (b) Model of the trapping potential.*

In this section we will combine the two experimental ingredients we have found in the previous chapter (in-situ images and trapping potential) to obtain the density profile as a function of the trapping potential, the key relation that allows us to gather the equation of state of the gas.

In the following we first describe the operation we do on the absorption imaging in order to extract the density profile from its column density. All the analysis procedure is written in Matlab code that I have developed during my thesis work.

Rotation

As a first step we apply to the image is a rotation in order to align the symmetry axis of the cloud with the x-axis of the image. This procedure is very important to get meaningful results from the inverse Abel transform routine. In chapter 5 we will see how a misalignment of the cloud produces substantial modification of the final equation of state one obtains. In order to estimate the rotation angle we use a 2D gaussian fit and finally we rotate the image using a built-in Matlab function[1].

Centring and averaging the images

Once the cloud is aligned with the x-axis, the next step consists in finding the position of the symmetry axis in order to define the initial point for the Abel deconvolution. This is in general an easy task, but one should nevertheless pay attention to it. Missing its position by $1 \div 2$ pixels can lead to completely wrong behaviour of Abel reconstruction (see chapter 5). The procedure we used is simply fitting the centre of the cloud with a gaussian function.

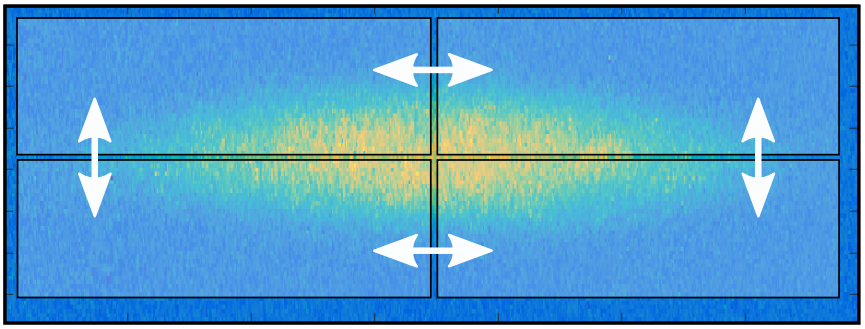

Figure 4.2: *In order to remove noise from the image before the Abel deconvolution, exploiting the symmetry properties of the cloud, we mediate over the four quadrant of the image.*

Once we find it, in order to remove as much noise as possible before the Abel deconvolution, the algorithm we need to apply to obtain the 3D density profile, we mediate the cloud over four quadrants as we show in fig 4.2. This is possible because the potential and, as a consequence, the cloud, has a cylindrical symmetry along

[1] The rotation of an image, of a non trivial angle such as $0, \pi/2, \pi...$, requires some kind of interpolation process that intrinsically introduce a smoothing in the rotated image. The best rotation algorithm, among the ones we have tested, turns out to be the *imrotate* built-in MATLAB function, choosing the *bicubic interpolation* method.

the x-axis and a reflection symmetry with respect to the plane perpendicular x-axis and passing through the centre of the cloud.

Finally, we crop the image to discard all but the region that contains the cloud. Choosing a good size for this crop is very important mostly along the y-axis, the direction along which we apply the Abel deconvolution. If this size is too big, we introduce unnecessary noise, on the other hand, if it's too small we risk to crop away interesting information from the tail of the density profile. Cutting too much from this region brings, in fact, an overall error on the determination of the local pressure.

4.1.1 Abel deconvolution

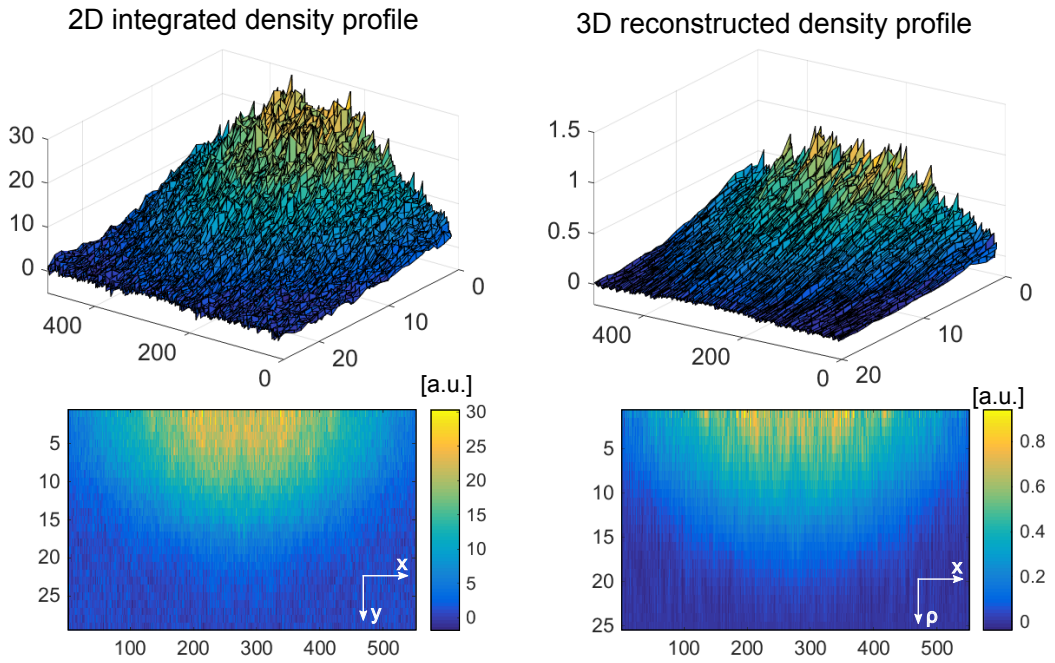

Figure 4.3: *On the left the integrated density profile. On the right the 3D density profile obtained with the inverse Abel transformation routine. For this figure we choose the parameter $c = 4$ in equation 4.1. As we can see we lose this way the first four raw of the image, but the result is quite smooth.*

Once we have the aligned and mediated density profile of the atomic cloud we are ready to apply the Abel deconvolution routine introduced in chapter 2, in order to obtain the 3D-density in cylindrical coordinates starting from the integrated density profile. The discretised version of equation 2.18, which we apply to the 2D matrix

of the column density of the cloud, is:

$$n_{3D}(x_i, \rho_j) = -\frac{1}{\pi} \sum_{k=j+c}^{j_{\max}} D\big[n_{2D}(x_i, y_k), y, c\big] \frac{1}{\sqrt{y_k^2 - \rho_j^2}}, \tag{4.1}$$

where x_i is the horizontal coordinate, along the axial axis of the cloud, of the pixel i, y_k is the vertical coordinate of the integrated density profile, ρ_j the radial coordinate of the final 3D-density and $j_{\max}$ is the number of vertical pixels of the integrated density profile. The function we called D is the numerical algorithm which allows to estimate the derivative of the integrated density, along the radial direction, using groups of c points. This algorithm is described in the Appendix A. In figure 4.3 we show an example of the Abel deconvolution where we use the derivative algorithm with a parameter $c = 4$.

4.1.2 Link density to the trapping potential

Equations 2.6 and 2.7 allow us to obtain both the pressure and the compressibility of the gas once we know the 3D density n as a function of the value of the potential U. Once we have a model for the trapping potential (see section 3.2.3), we can calculate the value it assumes for the position in space of each pixel of the image. We then link every value of potential obtained this way, with the value of the density corresponding to the same pixel.

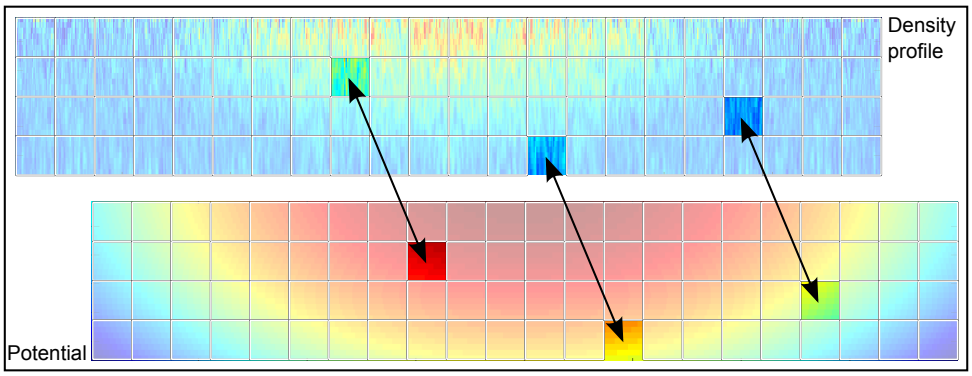

Figure 4.4: *Each pixel of the 3D density profile is linked to the correspondent one of the trapping potential. In this way we obtain the density as a function of the trapping potential: $n(\mathbf{r}) \rightarrow n(U)$. The white squares that we show in the figure only serve to give an idea of the procedure. The actual operation is done for each pixel of the image.*

Already at this stage we can see the power of using the local density approximation: from only one image, for example of size 800×30, we obtain 2400 experimental points. We show a sketch of this procedure in figure 4.4.

We now bin all those data point into intervals of potential. In practice we divide the potential in intervals of equal length. If there are less than three points inside

the interval the bin is rejected. Otherwise we assign to the bin corresponding to a certain potential U_i the mean of the value of the density of all the points inside the bin. We finally obtain the density profile of the cloud as a function of the trapping potential, as shown in figure 4.5.

In can be useful to notice that, most of the time, one can realise that there are errors in the trapping potential model by simply looking at the resulting data $n(U)$. If, for example, the points doesn't follow a smooth path but show a stairs like structure, it probably means that the aspect ratio of the cloud does not match with the ratio between axial and radial trapping frequencies, i.e. the estimation of the trapping potential is not done correctly.

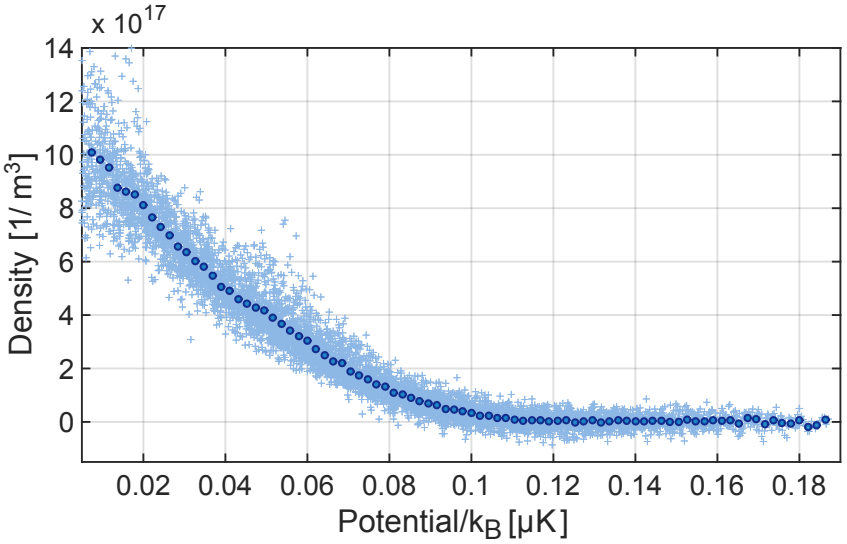

Figure 4.5: *Example of a density profile as a function of the trapping potential (unitary Fermi gas). Each pixel of the 3D density profile as a function of the trapping potential provides a point n=n(U). Because of the noise in the density profile the result is quite scattered. Binning the data in intervals of potential allows to obtain a much more smooth profile.*

4.2 The equation of state of an ideal Fermi gas

Since we have now the density as a function of the trapping potential, we own all the ingredients we need to reconstruct the equation of state of the system. Before exploring the physics of the unitary Fermi gas we first consider the case of the ideal Fermi gas, by using the theoretical results found in section 1.5.2, we both check our experimental routine and calibrate the number of atoms in the trap. As described in chapter 4.12 the non interacting gas is produced exploiting the zero crossing of the Fano-Feshbach resonance, a region where the scattering length vanishes and the inter-particle interaction becomes negligible.

Experimental pressure of an ideal Fermi gas

The first thermodynamic quantity we obtain is the pressure: starting from the density profile $n(U)$, we simply use the equation 2.6 we found in chapter 2:

$$P(U) = \int_U^\infty dU'\ n(U'), \tag{4.2}$$

Of course, since we have discrete data points, we cannot use this relation directly, but we need to substitute the integration with a discrete summation:

$$P(U_i) = \sum_{k=i}^{i_{\max}} n_k \Delta U, \tag{4.3}$$

where n_k and U_k are the density and potential relative to the k bin, ΔU is the potential range of one bin and $i_{\max}$ is the last considered pixel. The sum is not extended to all values of potential, but it is stopped as soon as the density is zero within the noise fluctuations. Integrating the density beyond $U_{i_{\max}}$ adds to all pressure point P_k a constant offset given by any small error introduced during the subtraction of the background from the image. On the other hand, integrating less, means that we are neglecting the tail of the profile, underestimating this way the pressure.

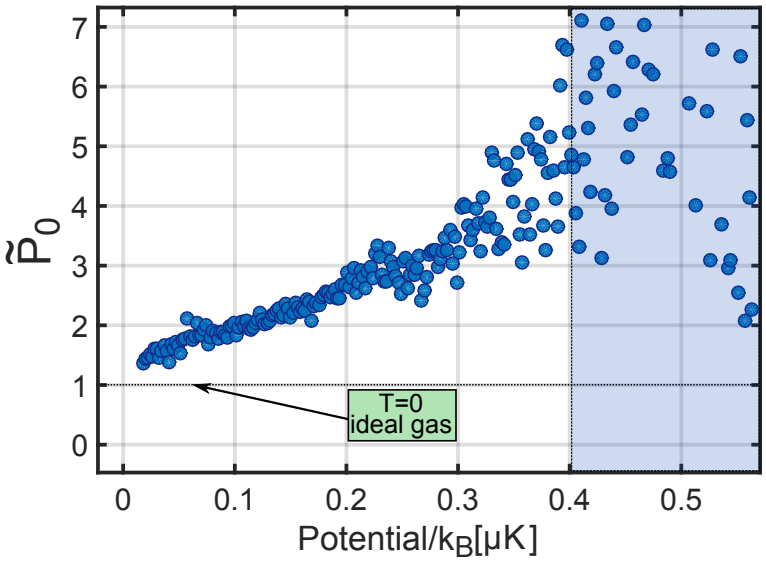

Figure 4.6: *Normalised pressure of an ideal Fermi gas as a function of the trapping potential. The points inside the blue rectangle are very noisy because the signal given by the density in the external region of the cloud is comparable with the imaging noise. For this reason they won't be considered in the in the following analysis.*

Finally we normalize the pressure with respect to P_0, remembering that:

$$P_0 = \frac{2}{5} n E_F, \tag{4.4}$$

where E_F is the local Fermi energy.

As we can see in figure 4.6, the pressure we obtained is always bigger than the pressure of the ideal gas at zero temperature, due to the finite temperature. In the region of deeper potential, where the density of the cloud is bigger, being the Fermi temperature proportional to the density, the ratio T/T_F is smaller and the normalised pressure approaches the zero temperature limit $P/P_0 = 1$. On the other hand, moving towards higher T/T_F region the pressure increases. In the very end of this region we can see that the ratio P/P_0 decreases again but this is not a physical effect, instead it is an artificial one. It is in fact caused by the fact that, in this low density region, the signal given by the tails of the cloud is comparable with the imaging noise. For this reason we will exclude this part of the density profile (enlighten in the figure 4.6 by the blue region) in the future analysis.

Experimental equation of state of an ideal Fermi gas

As we have done for the pressure we again follow the method described in chapter 2 to obtain the compressibility:

$$\kappa = -\frac{1}{n^2}\frac{dn}{nU}. \tag{4.5}$$

Estimating numerically the derivatives of noisy data points it's a very though and delicate task. If not done carefully, the result may be noisy enough to be completely useless or, on the other hand, may hide physical structures like the peak relative to the superfluid transition. A detailed discussion about this topic can be found in chapter 5 and the numerical derivative algorithm in appendix A.

As we have already done for the pressure, we normalise the compressibility respect to κ_0 and finally we plot in figure 4.7 the normalised compressibility as a function of the normalised pressure, i.e. the equation of state if an ideal Fermi gas. This result is used to finely set the imaging parameters in order to obtain the correct calibration between the actual number of atoms in the cloud and the one obtained from the absorption imaging. This is done multiplying the measured integrated density by a numeric factor. We than adjust this factor in order to find an agreement between the experimental equation of state and the theoretical one. Once we determinate this factor we use it to multiply the density profile in the unitary case. If the imaging is perfectly calibrated one should expect to find that the factor is equal to one. In our case it turns out that we overestimate the number of atoms and to get the right result we need to multiply the density profile obtained with the absorption imaging by a factor of 0.86, introducing a correction of 14% on the number of atoms.

Now that we have found a calibration for the imaging we are ready to work with the density profile of a unitary Fermi gas and the first thing we will discuss is the high T/T_F limit where the virial model can be used to estimate the temperature of the cloud.

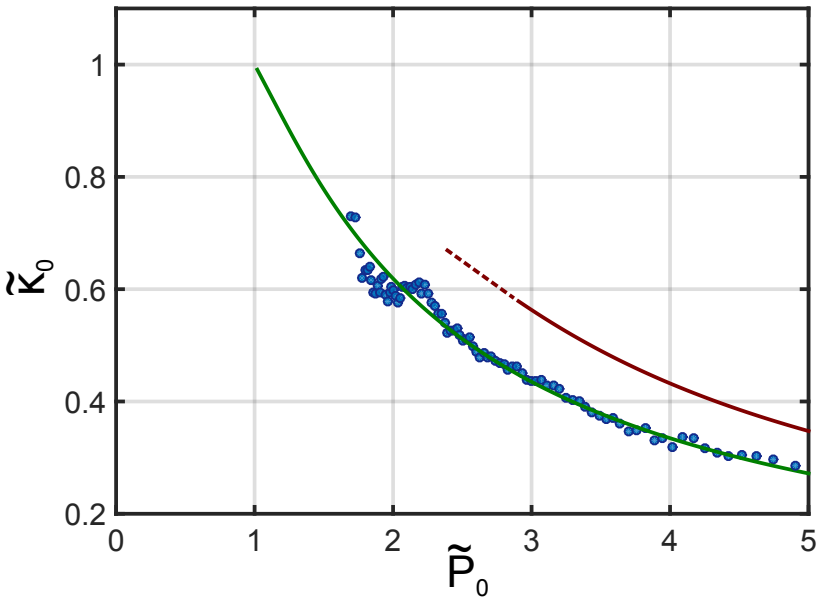

Figure 4.7: *Experimental equation of state of an ideal Fermi gas (obtained mediating over ~ 50 images). The green curve is the theoretical result found in section 1.5.2. The red curve is the equation of state of a unitary gas obtained with the virial expansion (section 1.5.3).*

4.3 Temperature: virial fit

Measuring the temperature of a unitary Fermi gas is a very hard task because one can not rely on standard thermometric technique used for ultracold atomic gases, like the measurement of the ballistic expansion in time of flight. Such a solution does not work because of the strong interaction between the atoms, which affects in a non trivial way the expansion. One solution, adopted by Salomon's group [3] in Paris, can be mixing with a bosonic atomic species the fermionic gas and than use the first as a thermometer. They produce a mixture of ^{6}Li and ^{7}Li (the bosonic isotope), and use the latter to obtain the temperature measuring the size of the bosonic part of the cloud, which is a weakly interacting gas, after a time of flight. Since in our experiment we have only one atomic species, such a technique can not be used.

In this section we describe how we estimate the temperature of the system using the tail in the density-potential of the unitary Fermi gas. This tail describes the high T/T_C region of the cloud, that's why is natural to consider the virial expansion described in section 1.5.3. We recall the equation 1.92:

$$n_{3D}(U) = \frac{2}{\lambda_{dB}^3}\left[\exp\left(\frac{\mu_0 - U}{k_B T}\right) + 2b_2 \exp\left(\frac{2\mu_0 - 2U}{k_B T}\right) + 3b_3 \exp\left(\frac{3\mu_0 - 3U}{k_B T}\right)\right], \tag{4.6}$$

where n_{3D} is the local density, $\mu_0 - U$ is the chemical potential in the local density

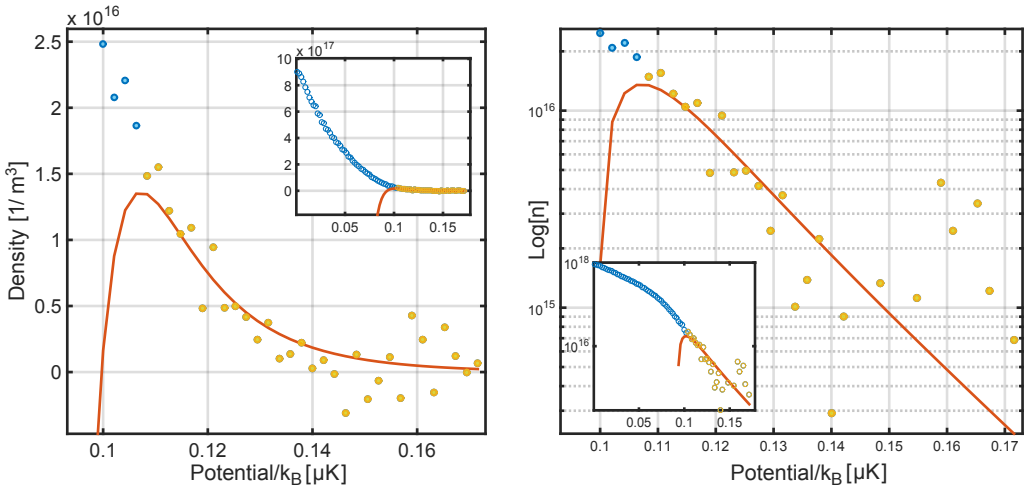

Figure 4.8: *Fit of the temperature of a unitary gas using the third order virial expansion on the tails of the density profile. Notice that only the very end of the profile is used for the fit. On the right de density is reported in a logarithmic scale.*

approximation and T is the temperature. The virial coefficients we use are reported in the table below.

Coefficient	Value	Reference
b_1	1	[45]
b_2	$3\sqrt{2}/8$	[46]
b_3	-0.29095295	[27]

Using this function we fit the temperature and the chemical potential as free parameter. This procedure only works if we consider the very end of the density profile. If one uses a bigger portion of the density profile will find that the fit result completely misses the experimental point. In order to quantitatively select the best region to use for the fit, we chose to minimize the resulting χ^2 parameter. As we show in figure 4.9, if we consider different clouds, prepared with the same experimental sequence, the obtained temperature changes in an interval of about 4 nK. In the case shown in the figure, the temperature is estimated to be between 18 and 23 nK.

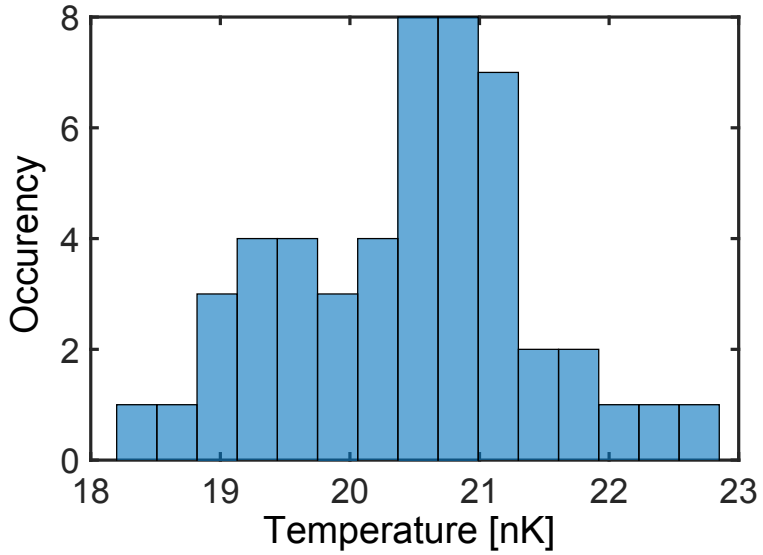

Figure 4.9: *Results for the estimation of the temperature for clouds produced with the same experimental sequence.*

4.3.1 Estimation of the b_4 virial coefficients.

Using the same portion of the density profile we have used for the estimation of the temperature in the previous section, can also estimate the value of the forth virial coefficient adding to equation 4.6 a free fit parameter, b_4. We write the fit function as:

$$n_{3D}(U) = \frac{2}{\lambda_{dB}^3}\left[\exp\left(\frac{\mu_0 - U}{k_B T}\right) + 2b_2 \exp\left(\frac{2\mu_0 - 2U}{k_B T}\right) + 3b_3 \exp\left(\frac{3\mu_0 - 3U}{k_B T}\right) + 4b_4 \exp\left(\frac{4\mu_0 - 4U}{k_B T}\right)\right], \tag{4.7}$$

where we fixed the values of b_4, b_4 and b_4 to the ones we reported in the table in section 4.3. We fit using this function about ~ 50 density profiles and we report the results in a histogram in figure 4.10. As we can see the value we find varies quite a lot from image to image. The mean value we obtained is $b_4 = 0.033$ with a mean standard deviation of 0.020.

In figure 4.11 we compare the result we obtained with the experimental ones by MIT group [5] and Paris group [3], and the theoretical one based on the stochastic variational approach by the Washington group [9].

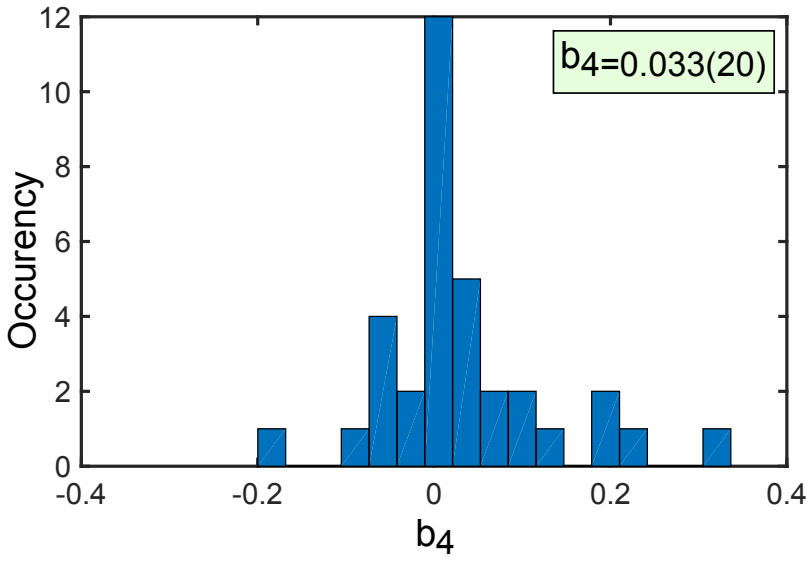

Figure 4.10: *Distribution of the virial b_4 coefficients obtained fitting different density profiles, keeping fixed the b_3 coefficient. The mean value we obtain is $b_4 = 0.033$ with a mean standard deviation of 0.020*

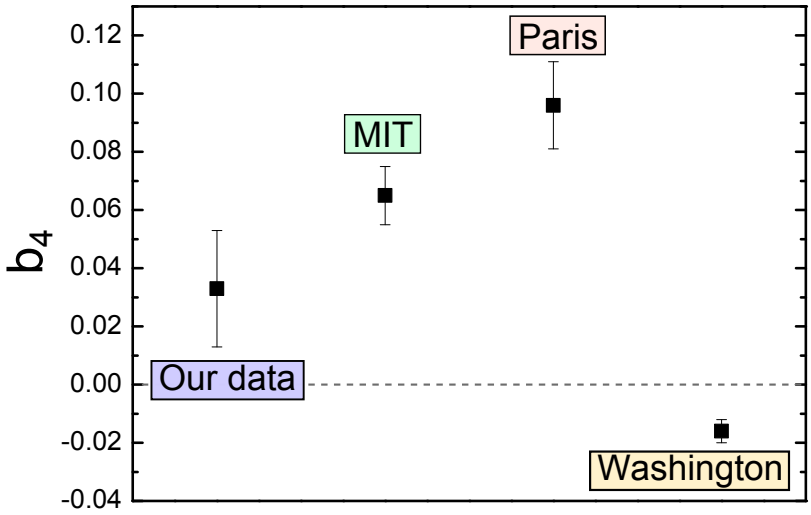

Figure 4.11: *Comparison of the value of b_4 coefficient estimated by us end the ones obtained by the MIT group [20], by the Paris group [3] and by the Washington group [9].*

4.4 Equation of state of a unitary Fermi gas

Starting again from the 3D-density as a function of the trapping potential we are finally ready to find the equation of state of a unitary Fermi gas. Repeating the same procedure we have used in the case of the ideal Fermi gas, we calculate the normalised pressure and the normalised compressibility of the unitary Fermi gas.

Pressure of a unitary Fermi gas

As we have done in section 4.2, the local pressure $P(U)$ is obtained integrating the density profile with respect to the potential:

$$P(U) = \int_U^\infty dU' \; n(U'). \tag{4.8}$$

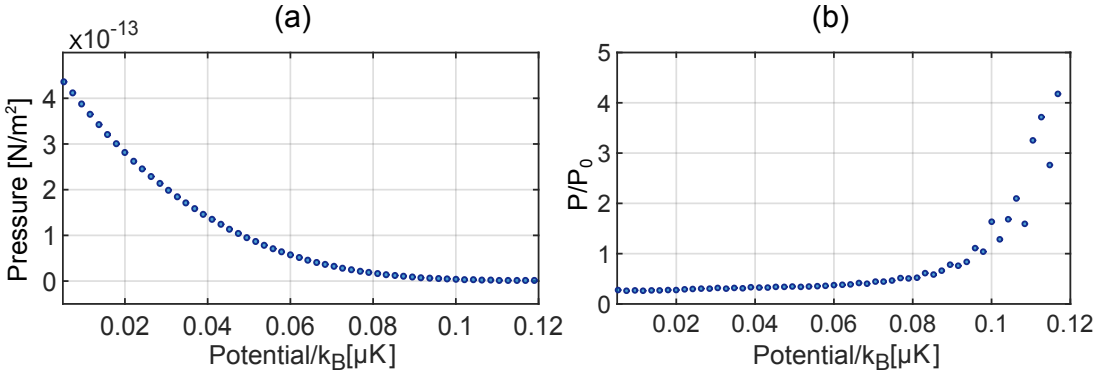

Figure 4.12: *(a) Pressure profile of a unitary Fermi gas. (b) Normalised pressure profile of a unitary Fermi gas. Both the profiles are obtained using only one image of the cloud.*

In figure 4.12, side (a), we show an example of the pressure profile we obtained from a single image. As we can see the points lies in a very smooth curve. This is due to the fact that the integration is an operation that intrinsically reduce noise.

We then normalise the pressure by $P_0 = 2/5nE_F$ and obtain the profile we show in the side (b) of figure 4.12. It's interesting to notice that, while the pressure of the non-interacting gas (figure 4.6) is always bigger than the pressure of an ideal gas at zero temperature, in the case of unitary Fermi gas in the high density region, corresponding to low T/TC, the pressure we find is smaller. This is not surprising at all since we expect the ratio P/P_0 to eventually reach the value of the Bertsch parameter when the temperature $T \to 0$.

Compressibility of a unitary Fermi gas

Always fallowing the procedure we have seen in section 4.2 we obtain the compressibility from the density profile using the relation:

$$\kappa = -\frac{1}{n^2}\frac{dn}{nU} \tag{4.9}$$

and we normalise this quantity by the value it assumes a an ideal gas at zero temperature and same density:

$$\kappa_0 = \frac{3}{2}\frac{1}{nE_F}. \tag{4.10}$$

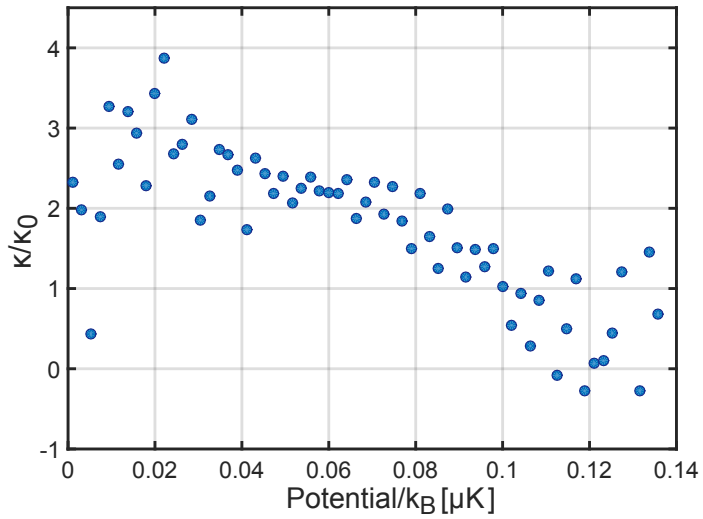

Figure 4.13: *Normalised compressibility of a unitary Fermi gas. The noise in the result is given mostly by derivative routine.*

In figure 4.13, although the presence of a good amount of noise due to the numerical derivative, we begin to see a peak-like shape in the low T/T_F region. As we have seen in chapter 1, being the compressibility proportional to the second derivative of the grand-potential, the presence of a peak would be a signature of a second order phase transition, like the superfluid transition we are looking for.

Pressure vs compressibility of a unitary Fermi gas

Now that we have the normalised pressure profile and the normalised compressibility profile we are ready to obtain the equation of state of a unitary Fermi gas in the form:

$$\tilde{\kappa} = \tilde{\kappa}(\tilde{P}). \tag{4.11}$$

As we have seen in section 1.4, this relationship is universal and does not depend by the specific system any more, the only requirement is the presence of only one

relevant scale of length in the hamiltonian describing the system, in our case the density. This allows us to mediate the equation of state obtained starting from different images because it doesn't matter if the number of atoms, or the temperature of the cloud fluctuates from shot to shot.

In figure 4.14 we show the equation of state of a unitary Fermi gas obtained mediating the results from ~ 50 different images. As we can see, although the single image produces a very noisy and scattered profile (light blue crosses), the final equation of state is very smooth.

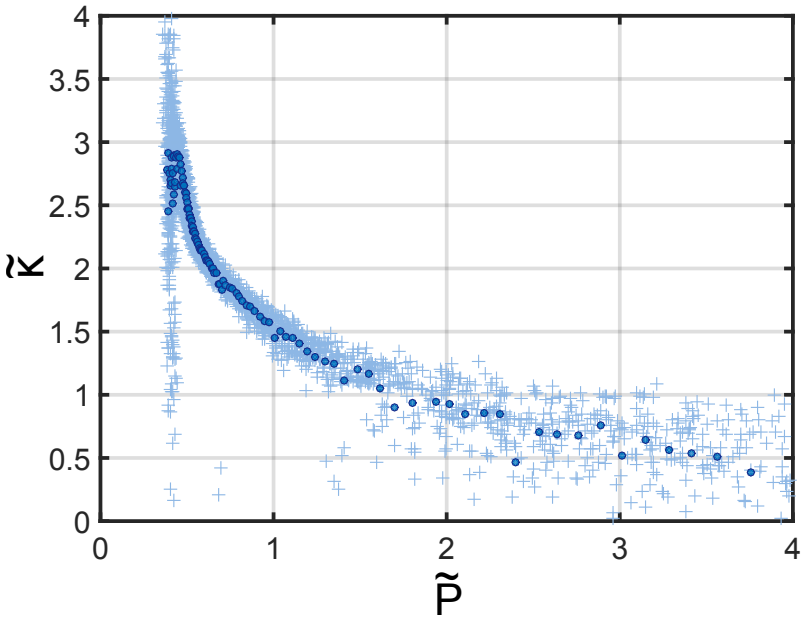

Figure 4.14: *Equation of state of a unitary Fermi gas. The equation of state is obtained independently for* ~ 50 *different images and plotted as a cross. The final profile is obtained mediating groups of* ~ 25 *consecutive points.*

In this figure it is finally possible to easily recognise a sharp peak in the compressibility, a clear signature of the superfluid phase transition.

4.5 Specific heat

Now that we have obtained the equation of state of a unitary Fermi gas in the form $\tilde{\kappa} = \tilde{\kappa}(\tilde{P})$, we would like to express this result in a more familiar way, by showing the relation between the specific heat and the normalised temperature.

Following the method we have described in section 4.5, the universal function that connect the specific heat per particle, c_V/N, to $\tilde{P}$, $\tilde{\kappa}$ and $\tilde{T}$, can be written as:

$$\frac{c_V}{k_B N} = \frac{3}{2}\frac{1}{\tilde{T}}\left(\tilde{P} - \frac{1}{\tilde{\kappa}}\right), \tag{4.12}$$

In order to find $\tilde{T} = T/T_F$ we use the temperature we have estimated in section 4.3. We remember that T_F is the Fermi temperature and that it can be expressed as a function of the density this way:

$$T_F = \frac{E_F}{k_B} = \frac{\hbar^2 \left(3\pi^2 n\right)^{3/2}}{2mk_B}. \tag{4.13}$$

The result is shown in figure 4.15.

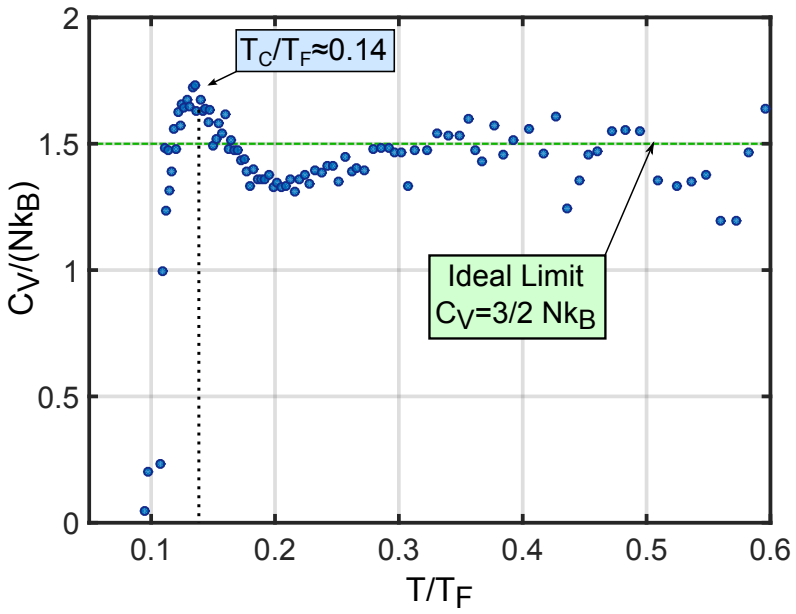

Figure 4.15: *Specific heat of a unitary Fermi gas. At $T_C \simeq 0.14T_F$ it is evident a λ-like peak corresponding the the superfluid second order phase transition. In the high temperature region the specific heat approaches the value $C_V = 3/2Nk_B$, of the non-interacting gas.*

As we can see, at low temperature, it is very clear the peak due to the superfluid transition. Such λ-shaped feature in the specific heat is in fact characteristic of second order phase transitions, as in the famous λ-transition in ^{4}He [47]. At high temperature the specific heat approach the value of the ideal gas case, i.e. $C_V = 3/2Nk_B$. Below the critical temperature it decreases and eventually reach the zero value. The experimental resolution is insufficient to resolve this region

We find the position of the peak to be at $T_c/T_F = 0.14(3)$ which is compatible, within the experimental error, with the measurement performed by the MIT group [5] 0.167(13), Salomon's group in Paris [3] 0.157(15), Tokyo group [4] 0.21(2) and with the theoretical calculations performed by the Washington group [6] 0.23(2), by a collaboration between university of Massachusetts, university of Paris-Sud, Kurchatov Institute in Moscow, university of Trento and ETH in Zurich [48] 0.152(7) and by the Cambridge group [8] 0.171(5).

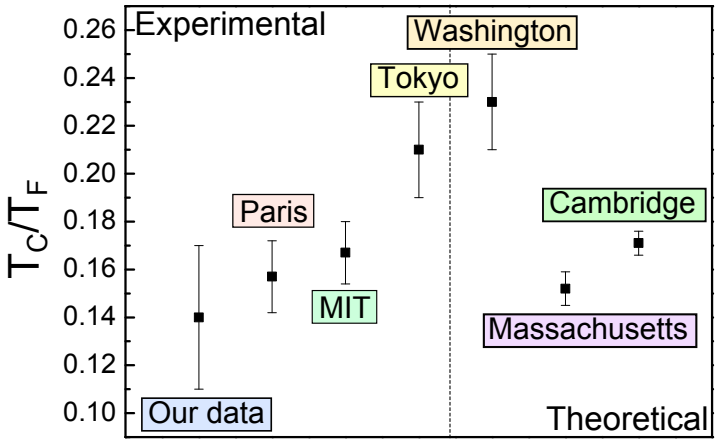

Figure 4.16: *Comparison of the value of the critical temperature T_C/T_F obtained experimentally by us, by the Paris group [3], by the MIT group [5] and by the Tokyo group [4]. From theoretical calculations by the Washington group [6], by a collaboration between Massachusetts, Paris, Moscow, Trento and ETH [48] and by the Cambridge group [8].*

4.6 Comparison

We end this chapter by showing in figure 4.17 the comparison between the experimental equation of state (blue dots) and the result obtained using the third order virial expansion we have described in section 1.5.3. As we can see there is a good agreement between these two in the high $\tilde{P}$, which correspond to the high T/T_C limit. For lower values of normalised pressure the virial expansion does not hold any more and the compressibility is drastically different. In this figure we also show indicatively the experimental results obtained by the MIT group [5]. The agreement in the region of the tails is surprisingly good.

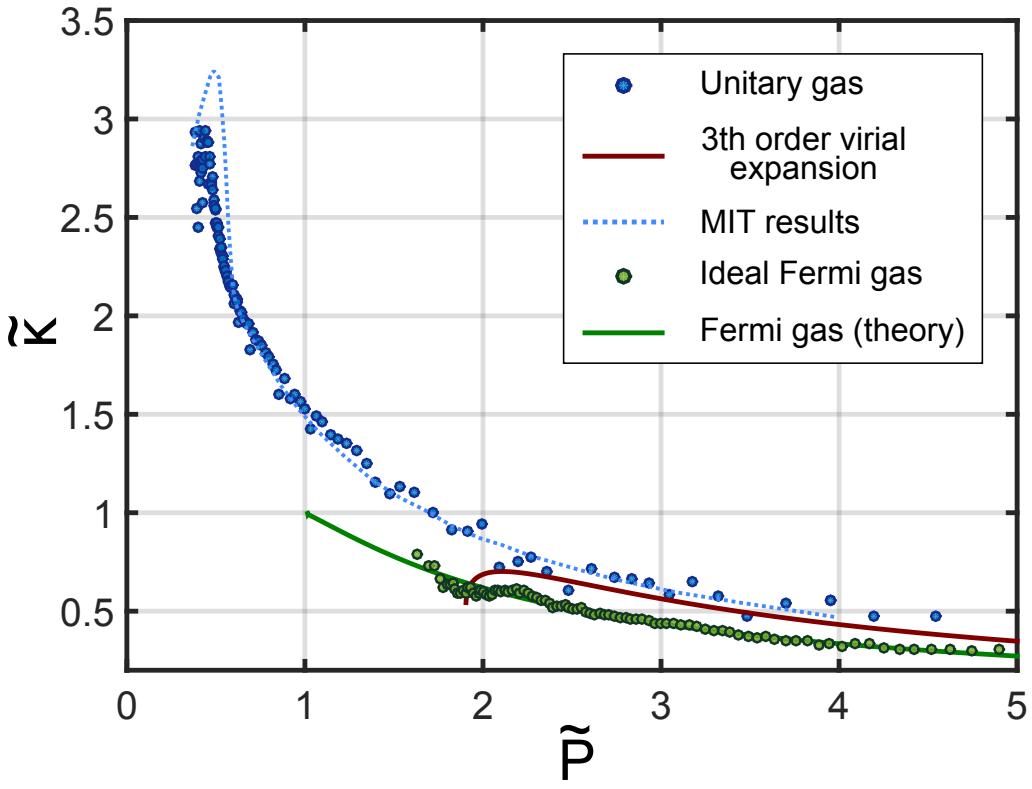

Figure 4.17: *Blue data points are the experimental equation of state of the unitary Fermi gas. The red curve is the theoretical result using the high temperature virial expansion described in section 1.5.3. The blue dashed curve are the experimental results obtained by the MIT group [5]. Green data points are the experimental equation of state of an ideal Fermi gas, and the green line the theoretical result described in section 1.5.2.*

Chapter 5

Error analysis

Every experimental measure is not perfect and it is inevitably affected by some uncertainty. In this chapter we will estimate both the systematic and the statistical errors that influence the determination of the equation of state. We show that within our confidence interval the main features are not washed out. We will conclude this chapter showing how we tested the numerical routine using an artificial density profile.

5.1 Systematic error

We can identify as principal sources of uncertainty in our analisys:

- The calibration of the number of atoms
- The determination of the trapping potential
- Numerical routine errors

Error in the number of atoms

In section 3.3.6 we have seen that calibrating the number of atoms with absorption imaging is a very hard and delicate task. Because of this, as in [5], we have used the equation of state of the non interacting gas to finely calibrate the the optical density we obtain with absorption imaging. Even using this method we still estimate to have an uncertainty of about 15% on determination of the number of atoms.

In order evaluate how this uncertainty is reflected in the final result, we artificially varied the atom number increasing and decreasing the initial measured optical density by the 15% and we give this as input of the numerical routine. The result is reported in figure 5.1, where the red points corresponds to have increased the number of atoms and the green ones, on the contrary, to have decreased it.

As we can see there is quite a big difference between the two curves. While in the high P/P_0 region they are similar, in the low P/P_0 part we see a relative shift of the phase transition peak of about 17%. We apply the same procedure to the

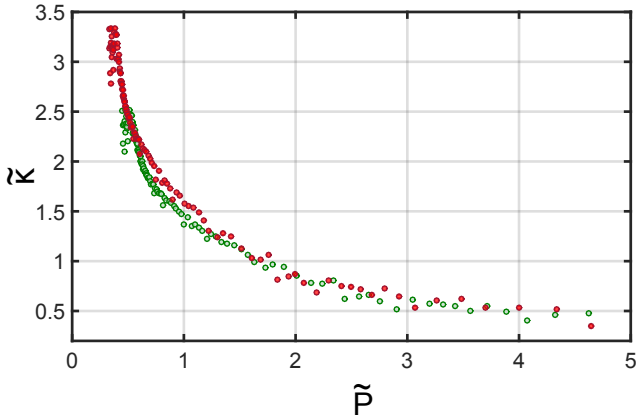

Figure 5.1: *Equation of state obtained changing the number of atoms as input of the numerical routine. The red point corresponds to an increment of* 15% *while the green ones to a decrement of* 15% *in the number of atoms.*

specific heat as a function af the normalised temperature and we find in this case a relative shift of the peak of about 22%. The big uncertainty in the determination of the critical temperature in section 4.5, which is estimated in fact by the position of the peak, is in fact mainly caused by this uncertainty about the number of atoms.

Trapping potential model

In section 3.2.3 we have shown how we describe the trapping potential and how we experimentally estimate it. Concerning the weak confinement along the x-axis (cylindrical symmetry axis), given by the magnetic curvature, the potential is estimated using the oscillation of the cloud inside the trap. Measurement of frequency of this kind are very accurate and the error is completely negligible in the final result (typically $\leq 1\%$). The problem rises when we want to estimate the potential along the other two directions, given by the optical dipole trap. Since with the current experimental setup the size of the cloud is comparable with the ODT beam waist, the potential along the radial direction cannot be considered harmonic and we cannot estimate it with the oscillation frequency any more. Because of this we have to measure the potential characterising the ODT beam with a CCD camera (waist) and with a power-meter (power). Both of these measure are less accurate than the frequency one and we can estimate an uncertainty of 5% both for the power and the waist. Concerning the power, the uncertainty is mainly due to the power-metre calibration. In the case of the waist the problem arise from the fact that we cannot measure it directly inside the vacuum chamber, instead we have to deviate it and perform the measurement outside. In this way all the deviations and aberration due to optical elements are not considered by this measurement, but modifies indeed the actual beam inside the chamber.

As we have done for the number of atoms we show the result of changing these

quantity at the input of the numerical routine in figure 5.2. This time since the resulting curves are quite similar we only plotted the equation of state obtained with the mean value and we coloured the uncertainty regions.

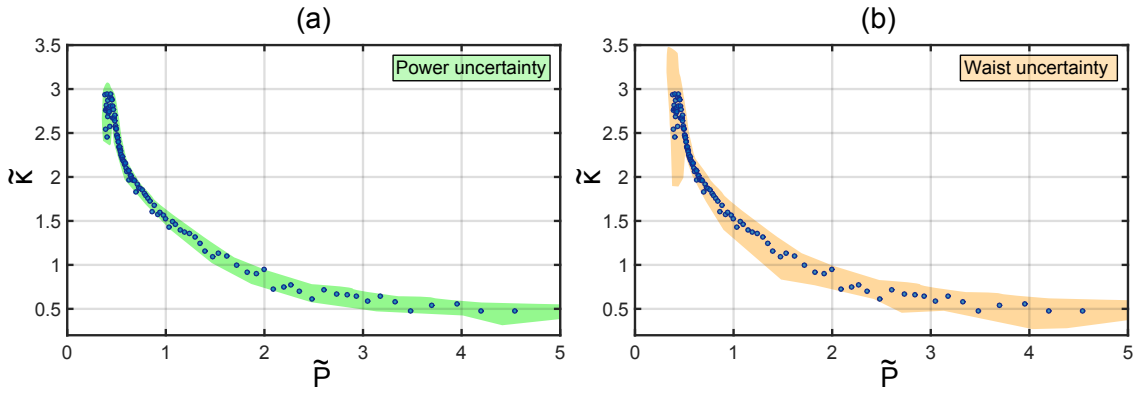

Figure 5.2: *(a) Uncertainty in the equation of state introduced by a 5% variation of the power of the ODT beam. (b) Uncertainty in the equation of state introduced by a 5% variation of the ODT beam waits.*

As we can see an uncertainty in the power of the ODT beam does not affect too much the final result, the only effect is to slightly change the high P/P_0 tail. The relative shift of the peak position is less than 1% therefore we safely neglect the contribution of this effect in the final error on the critical temperature.

Concerning the beam waist, the effect is much more significant. The relative position of the peak changes respectively by $\sim 3\%$. This corresponds also to an uncertainty of $\sim 5\%$ in the estimation of the critical temperature.

5.2 Statistical error

All the errors described in the previous section were systematic and the only way to improve the precision of the final result is enhance directly the accuracy in the estimation of experimental parameters. On the contrary the statistical error can be drastically reduced just by performing more measurements and then take the mean as the estimator of the result. We want to point out that it is not obvious that such an operation of mediating different measurement can always be done. Let's think for example about the compressibility as a function of the trapping potential we have found in section 4.4. Since the result is very noisy one may think to consider lots of different profiles and, mediating them, obtain a smooth compressibility curve. This would actually be rather wrong. The reason is that every image, although is taken in the same experimental condition, does not correspond to the exact same physical situation. From shot to shot things like the temperature or the number of atoms in the cloud fluctuates and the relation between the compressibility and the trapping

potential changes too[1]. If fluctuations are not negligible, taking the mean of these curves would have no sense. Fortunately for us all this reasoning does not hold any more in the case of the equation of state expressed by normalised dimensionless quantity. As we have seen in chapter 1 this equation is universal and never changes despite of fluctuation in temperature, number of atoms or whatever one can think of. It is exactly exploiting this property that in chapter 4 we have mediates the equation of state over ~ 50 images, obtaining this way a very smooth result. We show the outcome of this operation in figure 5.3.

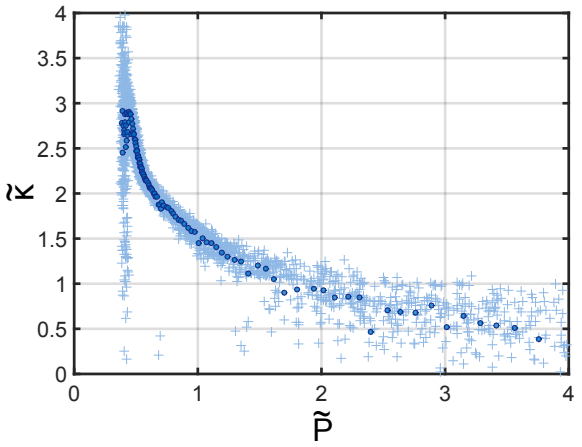

Figure 5.3: *Universality allows to mediate the equation of state over many clouds despite of the fluctuations of the number of atoms or of the temperature.*

5.3 Numerical routine test

Now that we have described the most important source of error in experimental measurements we want to discuss about the goodness of the numerical algorithm we use to extract the equation of state starting from the in-situ density profile and the trapping potential. In this numerical procedure there are two fragile points: the Abel deconvolution and the numerical derivative. Instead of describing the errors introduced by the single part of the program[2], we show the strategy we have chosen to estimate the overall error introduced by the whole routine. The idea is very simple: we generate a *artificial* optical density, of which we can analytically calculate the equation of state, and we use it as the input for the numerical routine.

[1] For simplicity one can think about the pressure instead of the compressibility since the reasoning is the same but it is more intuitive. If the trapping potential stays the same but the number of atoms is much smaller we clearly expect to find the pressure to be much lower and indeed the curve that represents the pressure as a function of the potential changes as well.

[2] Considering each individually each problem is actually very important in order to improve the program, but in this section we wont only to describe the amount of error introduced by the final version of the routine. Details about the numerical derivative can be found in appendix A.

Finally we compare the result we obtain with the analytical one estimating this way the error introduced by the program.

Artificial density profile

In order to obtain a useful *artificial* density profile we choose a density function that qualitatively reproduces the features of the equation of state similar to the one we expect to measure experimentally. An easy expression we find out to fulfil this job, is the following:

$$\hat{n}(\mu) = A\left(Be^{-\alpha\mu} - e^{-\beta\mu}\right), \tag{5.1}$$

where $A = 10^{17}\mathrm{m}^{-3}$, $B = 3,64$, $\alpha = 55\mu\mathrm{K}^{-1}$ and $\beta = 137.5\mu\mathrm{K}^{-1}$. Using those value the density is expressed in m^{-3} and the potential in μK. The density profile is plotted in figure 5.4 on the left. From this density we analytically calculate, using all the formulas we introduced in chapter 1.5.2, the *artificial* equation of state in the form $\hat{P} = f(\hat{\kappa})$. We plot the result in figure 5.4 on the right. As we can see this *artificial*

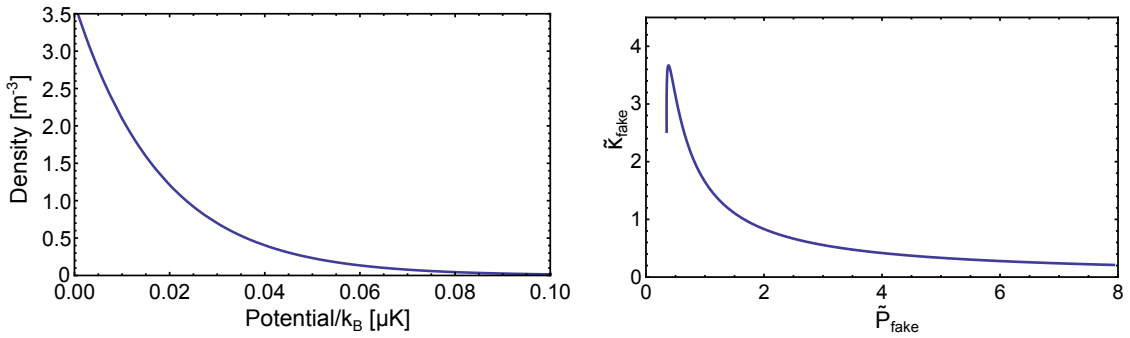

Figure 5.4: *On the left the artificial density profile $n(U)$. On the right the equation of state calculated analytically form the artificial density profile.*

equation of state is very similar to the one we have measured experimentally. It presents a peak at low P/P_0 and then decrease slowly toward zero for high P/P_0.

Artificial image

Using the *artificial* density profile and the expression for the potential we obtain in section 3.2.3, we generate an image of a *artificial* cloud. We then give this image as input to the numerical routine and we show the comparison with the analytical one in figure 5.5. From the comparison we estimate a discrepancy of $\sim 4\%$ in the high P/P_0 region and $\sim 8\%$ in the low one. This error, at the moment, is much smaller that the one given by the uncertainty on the number of atoms, therefore at this stage it does not represent a problem. Nevertheless if one is interested in improving the numerical routine it is convenient to add a white noise contribution to the *artificial* image, in order to simulate the actual noise in the experimental images and evaluate this way also the algorithm robustness to noise. In figure 5.6 we show an example

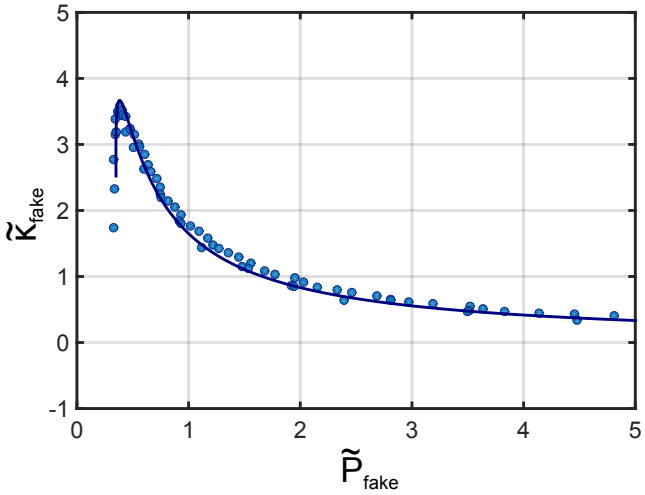

Figure 5.5: *Comparison between the artificial equation of state obtained by using the numerical routine (dots) and the one calculated analytically (line).*

of that. On the right we plot the *artificial* image to give an idea of the amount of white noise introduced.

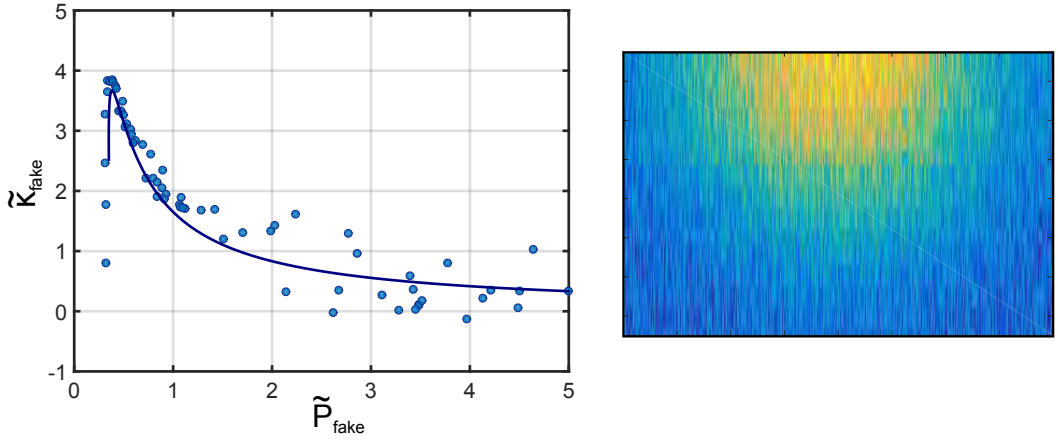

Figure 5.6: *On the left the comparison between the analytical fake equation of state and the one obtained starting from the fake noisy image on the right.*

As we can see the introduction of noise affects quite a lot the final results. Fortunately this error is mostly statistical and can be therefore solved just by taking several image and mediate the result at the end.

The comparison between those two curves can also be useful to adjust routine parameters like binning dimension, Abel deconvolution method and derivative step. This is simply done changing those parameters trying to minimize the difference between the analytical solution and the obtained points.

5.3.1 The rotation and the centring problem

An additional problem we have not considered yet, is given by the fact that in the experimental images, the cloud is not centred nor aligned in the correct way, as described in section 4.1. Since Abel deconvolution requires the cloud to be correctly positioned and aligned in order to work properly, we have to estimate both the position of the inclination of the cylindrical symmetry axis of the cloud with respect to the image.

In order to evaluate how an error in the determination of these quantity affects the final result, we use again our experimental data. Following the same steps of section 5.1, we force the routine to miss the centre position by two pixels for each direction and the angle by 1° in both direction. The results are shown in figure 5.7. As we can see both an error in the rotation angle and in the estimation of the

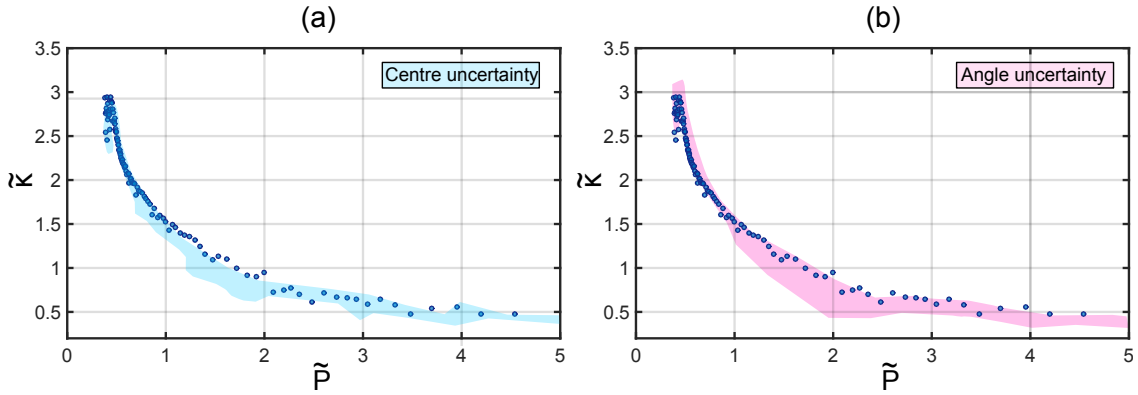

Figure 5.7: *(a) Error in the equation of state introduced by missing the centre position by two pixels in all the directions. (b) Error in the equation of state introduced by missing the rotation angle by* 1° *in both the directions.*

centre changes the relative position of the peak by a factor less than 2%. Because of this we consider negligible, with respect to the other source of error described in this chapter, the uncertainty introduced by these factors on the determination of the critical temperature.

Conclusions

My thesis has been focused on the experimental determination of the equation of state (EoS) of a strongly-interacting (eventually superfluid) Fermi gas composed by ^{6}Li atoms trapped in mixture of two spin states. In the experiment, the strongly interacting regime has been achieved for about 2×10^5 paired fermions by preparing the ultracold gas close to the broad Fano-Feshbach resonance located around 832 G, i.e., in the limit for which the scattering length between fermions becomes much larger than the inter-particle distance. This regime is called universal since the physics essentially depends only on the mean inter-particle distance and on the temperature. The thermodynamics of the gas in this condition is also universal, being the different thermodynamics quantities connected via universal scaling functions.

In my thesis I have developed a full method to derive the EoS for these strongly-interacting fermions. The recipe to reconstruct the equation of state combines experiment and theoretical analysis with the same weight. It consists of the following ingredients:

1. Acquisition of several 2D integrated in-situ density profiles of the unitary gas by absorption imaging procedure. The good quality of the images is one of the essential points of this method: it is mandatory to avoid spurious effects due to diffraction, blurring subsequent to multiple atom-photon scattering, out-of-focus distortions and electronic noise of the CCD camera device. For this reason, part of my work in the lab was to design and to characterise the imaging set-up using the state-of-art equipments to fulfil the requirements. The calibration of the imaging was also accompanied by the calibration of the atomic trapping potential (frequencies and laser trap parameters), since it is another important task of this method.

2. Writing an efficient code to perform the Abel deconvolution. The reconstruction of the 3D atomic density from the 2D integrated profile is another important step: it allows to obtain n(U), i.e. the density as a function of the trapping potential. Applying the local density approximation, it is then possible to map the thermodynamics of the trapped gas into the one of many homogeneous systems: therefore, every density profile generates a complete equation of state. I have developed an efficient Matlab code able to manipulate and to analyse the experimental images, obtaining the EoS of the system. I have also tested this routine on artificial density profiles, validating its reliability.

3. Calibration of this code on the well-known ideal Fermi gas case. Since the thermodynamics (EoS) of the ideal Fermi gas is a text-book relation, I have calibrated the optical density comparing the experimental EoS with the theoretical one.

4. Application of this method on the strongly-interacting clouds, to derive the equation of state of the unitary Fermi gas. In the low temperature regime ($T/T_F < 1$), I have observed a λ-like peak in both the compressibility and in the specific heat, a clear signature of the superfluid transition in this system composed by fermionic pairs at unitarity. The estimated value for the critical temperature $T_C/T_F \sim 0.14$ is in good agreement with the experimental and theoretical values in the literature. In the high temperatures limit ($T/T_F \geq 1$), I have used the virial expansion to fit the experimental profiles, extracting the temperature of the cloud. This is particularly relevant for systems (like ours) for which there is no direct thermometer available.

The future perspectives of this work are:

- As we have seen the quality and the reliability of the EoS analysis depends strongly on the possibility of measuring correctly the number of atoms. For this reason, I will try to reduce our atom-number uncertainty (at this moment of the order of 15%), improving the calibration of the optical density, using different methods such as the one reported in [44]. In this way, we will have an independent determination of the atom number that does not involve the equation of state of the non-interacting gas.

- An interesting direction is the application of this scheme to the Bose gas. Also in this case, we expect a singularity in the compressibility at T_C. One issue concerns the possibility to obtain clear and not saturated images in the proximity of the BEC phase-transition due to the high density. This problem may be circumvented by implementing out-of-resonance phase-contrast imaging. We are currently implementing the optical set-up to proceed in this direction. The study of the equation of state using local density approximation in the case of a bosonic superfluid is relatively unexplored [49]. One alternative proposal is based on the so-called Global Variables [50] and it has been recently applied on a gas of Rb atoms [51]. This method relies on averaged thermodynamic quantities while the one developed in this thesis on local ones. In the future, we want to compare the two different approaches.

Appendices

Appendix A

Numerical derivative of noisy data

The estimation of derivatives from numerical data is probably the most delicate segment in our analysis routine, which enters both in the inverse Abel deconvolution routine and in the estimation of the compressibility. In literature one can find two families of methods to face this problem: local methods and global methods. Suppose you have a series of point $p_1, p_2, ..., p_i, ...p_N$, local methods, in order to estimate the value of the derivative in a point i, uses only data points in the neighbourhood of a_i. On the other hand, global methods makes use of all N points of the series and, using a representation given by some basis functions, they estimate which function best interpolate the data points. These methods are very powerful, especially if one can guess properties about the trend of the physical function from which data point come from. Unfortunately these global approaches does not fit very well with our needs, in fact, as we will show, they tend to give spurious results near the first and the last few points, which happens to be a very important region in our experiment.

A wide variety of techniques are described and compared in detail in [35] and in [52]. We used those articles as major reference to find out which method suite better our needs.

Test function

We now report the simple test we used to choose the derivation algorithm in our routine. We start with a known test function $f(x)$:

$$f(x) = e^{-x} + A \exp\left[-\frac{(x - x_0)^2}{\sigma^2}\right], \tag{A.1}$$

where we set $A = 0.3$, $x_0 = 1$ and $\sigma = 0.2$. We choose such a function because it presents both a smooth behaviour and a sharp peak. This way we can check simultaneously how the derivation algorithm behaves in both cases. We integrate $f(x)$ and we call $F(x)$ the result:

$$F(x) = \int_0^x f(x)dx = -e^{-x} + 0.08 \ \mathrm{Erf}(5x - 5)\,. \tag{A.2}$$

As we show in fig A.1 using $F(x)$, we generate a series of equispaced data point $F_1, F_2, ..., F_i, ...F_N$ and we add to each point a random, uniformly distributed, noise (white noise). We now apply several differentiation routine to $F_1, F_2, ..., F_i, ...F_N$,

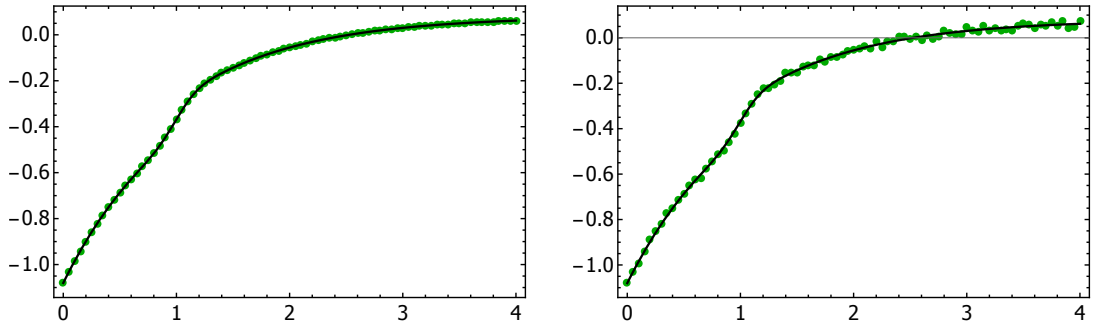

(a) Without noise (b) With noise

Figure A.1: *The black solid line is the plot of the test function $F(x)$ (A.2). The green points are the set of data points obtained from the same function without noise, in figure (a), and with the addiction of white noise, in figure (b). The relative noise level near the change of slope is about $2 \div 3$ %.*

where $F_k \equiv F(x_k) + \text{noise}_k$, and we compare the result with the function $f(x)$.

Simple difference

The simplest way of estimating the differentiation of a set of data point is taking the difference between consecutive points and divide it by the distance between those point:

$$\left(\frac{\partial F}{\partial x}\right)_i = \frac{F_{i+1} - F_i}{\Delta x}, \tag{A.3}$$

where $\Delta x = x_{i+1} - x_i$ is the step size. If noise is negligible this formula is just fine, but if it is not the case one have:

$$\left(\frac{\partial F}{\partial x}\right)_i = \frac{(F(x_{i+1}) + \text{noise}_{i+1}) - (F(x_i) + \text{noise}_i)}{\Delta x} \tag{A.4}$$

$$= \frac{F(x_{i+1}) - F(x_i)}{\Delta x} + \frac{\text{noise}_{i+1} - \text{noise}_i}{\Delta x}. \tag{A.5}$$

The problem is that is possible, like in the case of our experimental data, that the two terms in the equation A.5 (real derivative and noise component) could have the same order of magnitude. As we show in fig. A.2 this introduce a big error in the estimation of the derivative.

With a couple of small variation, we can improve this method quite a lot, obtaining, with a still very simple formula, a way better estimation of $f(x_i)$. The fist improvement is to use symmetric intervals, reducing in this way a systematic error

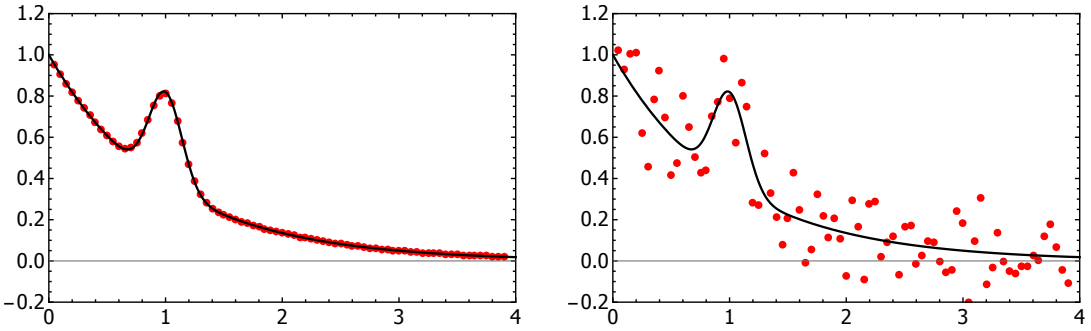

(a) Without noise (b) With noise

Figure A.2: *Black solid line is the plot of the true derivative $f(x)$, red points are the derivative estimation using simple difference method. Fig(a) is the reconstruction without noise, fig(b) with white noise. The noise level is about $2 \div 3$ % near the peak (see fig. A.1b).*

in position, since with formula A.4, you are actually estimating $f((x_{i+1} - x_i)/2)$. The second improvement is to use a step size larger than Δx. In this way we lose, if we use an interval n times larger, all the detail smaller than $n\Delta x$, but we gain in signal to noise ratio (fig A.3). This is easy to realize looking at equation A.5: the first term most of the time increase while the second, since noise is uncorrelated, does not change. We can write this new estimator as:

$$\left(\frac{\partial F}{\partial x}\right)_i = \frac{F_{i+n} - F_{i-n}}{2n\Delta x}, \tag{A.6}$$

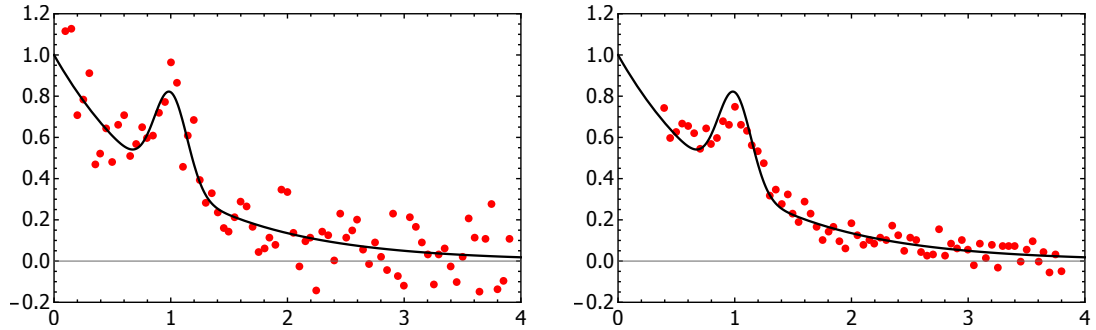

(a) n=2 (b) n=6

Figure A.3: *The black solid line is the plot of the true derivative $f(x)$, the red points are the derivative estimation using equation A.6, with $n = 2$ (a) and $n = 6$ (b). Notice how bigger n reduces noise but also smears out the peak.*

Taylor expansion method

The idea behind this method is this: to estimate the derivative in $F_i \equiv F(x_i)$ we chose $2k+1$ points around F_i, $(F_{i-k}, ..., F_i, ...F_{i+k})$ and we find the polynomial of order m which best fit those points. We finally use the derivative of this interpolated polynomial as the derivative estimator. All this procedure can be synthesize in one formula[52]:

$$\left(\frac{\partial F}{\partial x}\right)_i = \sum_{j=1}^{k} \alpha_j \frac{F_{i+j} - F_{i-j}}{2j\Delta x}, \tag{A.7}$$

with

$$\alpha_j = 2(-1)^{j+1} \binom{k}{k-j} \Big/ \binom{k+j}{k}, \tag{A.8}$$

where $\Delta x = x_{i+1} - x_i$ is the step size. As we can see in fig. A.4 this method is amazingly good with noise-free input data point, but it is very sensible even to small amount of noise.

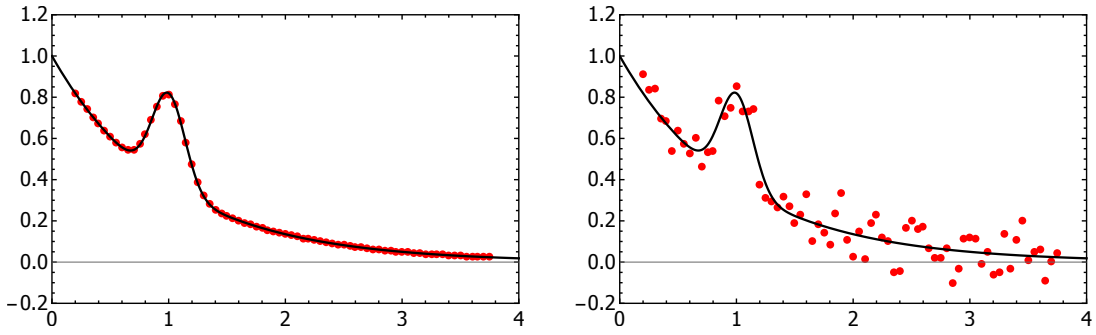

(a) Without noise (b) With noise

Figure A.4: *The black solid line is the plot of the true derivative $f(x)$, the red points are the derivative estimation using Taylor expansion method (with $k = 2$ and $j = 2$). In figure (a) the reconstruction without noise, in figure (b) with white noise. The noise level is about $2 \div 3$ % near the peak (see fig. A.1b).*

Spline method

Spline method is a global method that consist in interpolate data point using a bases of curves called spline [52]. In figure A.5 we plot the interpolating function in (a) and its derivatives calculated for $x = x_i$ in (b). As we can see, this method is quite noise resistant, but it has a couple of major issues, that prevent us to use it in our implementation: the first, and most important one, is that this technique tends to be very inaccurate in the boundary regions, a very critical and interesting region in our experiment. Second, it produces oscillating artefacts that bring correlated noise, that one can erroneously interpret as a signal of some kind.

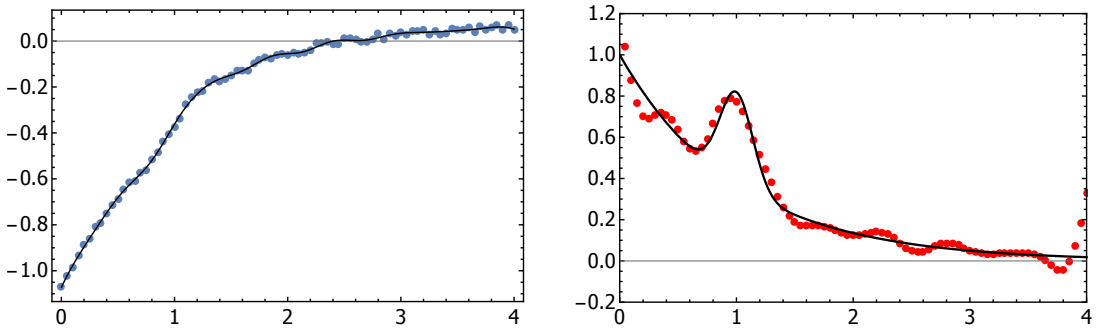

(a) Spline interpolation (b) Spline derivation

Figure A.5: *(a) The red line shows the spline interpolation of the series of points F_i. (b) The black solid line is the plot of the true derivative $f(x)$, the red points are the derivatives of interpolating function calculated in x_i.*

Method we use

In the end the method we adopted in our numerical routine is an extension of the *simple difference* method, with a symmetric interval of n points, we have described above. The idea is simply to consider in the estimation of the derivative all the points inside the interval of $2n$ points. In practice we mediate the result we obtained using all the possible interval size from 2 to $2n$ points. We can therefore write the estimator of the derivative as:

$$\left(\frac{\partial F}{\partial x}\right)_i = \frac{1}{n_{\max}} \sum_{n=1}^{n_{\max}} \frac{F_{i+n} - F_{i-n}}{2n\Delta x}. \tag{A.9}$$

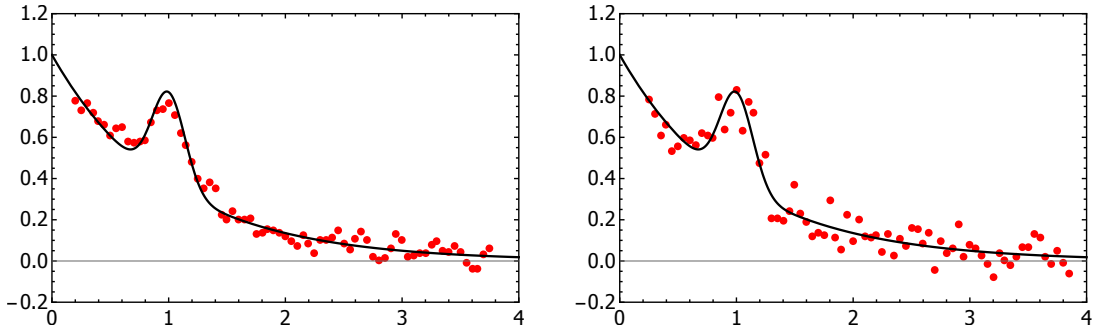

(a) Final method (b) Simple difference

Figure A.6: *The black solid line is the plot of the true derivative $f(x)$. (a) The red points are the derivative estimation using equation A.9 with $n = 4$. (b) The red points are the derivative estimation using equation A.6 with $n = 4$.*

As we can see in figure A.6(a) the estimation of the derivative using the equation A.9 allows to obtain a smoother result that the simple difference method (figure

A.6(b)) , without the generation of unwanted artefacts of spline method (figure A.5 (b)). That is why we have adopted this approach over the other we have tested.

A possible improvement on this method can be considering different weight for each term in the summation of the equation A.9. In this way one can, for example, filter out the high frequency component of the noise.

Bibliography

[1] M Inguscio, W Ketterle, and C Salomon. "Ultra-cold Fermi Gases, Proceedings of the International School of Physics Enrico Fermi, Course CLXIV, Varenna 2006". In: (2008).

[2] Ao J Leggett. "Diatomic molecules and Cooper pairs". In: *Modern trends in the theory of condensed matter*. Springer, 1980, pp. 13–27.

[3] S Nascimbène et al. "Exploring the thermodynamics of a universal Fermi gas." In: *Nature* 463.February (2010), pp. 1057–1060. ISSN: 0028-0836. DOI: 10.1038/nature08814. arXiv: 0911.0747.

[4] Munekazu Horikoshi et al. "Measurement of universal thermodynamic functions for a unitary Fermi gas." In: *Science (New York, N.Y.)* 327.5964 (2010), pp. 442–445. ISSN: 0036-8075. DOI: 10.1126/science.1183012.

[5] Mark J H Ku et al. "Revealing the superfluid lambda transition in the universal thermodynamics of a unitary Fermi gas." In: *Science (New York, N.Y.)* 335.6068 (Feb. 2012), pp. 563–7. ISSN: 1095-9203. DOI: 10.1126/science.1214987. URL: http://www.ncbi.nlm.nih.gov/pubmed/22245739.

[6] Aurel Bulgac, Joaquín E. Drut, and Piotr Magierski. "Spin 1/2 fermions in the unitary regime: A superfluid of a new type". In: *Physical Review Letters* 96.9 (2006), pp. 2–5. ISSN: 00319007. DOI: 10.1103/PhysRevLett.96.090404. arXiv: 0602091 [cond-mat].

[7] Evgeni Burovski et al. "Critical temperature curve in BEC-BCS crossover". In: *Physical Review Letters* 101.August (2008), pp. 1–4. ISSN: 00319007. DOI: 10.1103/PhysRevLett.101.090402. arXiv: 0805.3047.

[8] Olga Goulko and Matthew Wingate. "Thermodynamics of balanced and slightly spin-imbalanced Fermi gases at unitarity". In: *Physical Review A - Atomic, Molecular, and Optical Physics* 82 (2010), pp. 1–11. ISSN: 10502947. DOI: 10.1103/PhysRevA.82.053621. arXiv: 1008.3348.

[9] D. Rakshit, K. M. Daily, and D. Blume. "Natural and unnatural parity states of small trapped equal-mass two-component Fermi gases at unitarity and fourth-order virial coefficient". In: *Physical Review A - Atomic, Molecular, and Optical Physics* 85.3 (2012), pp. 1–12. ISSN: 10502947. DOI: 10.1103/PhysRevA.85.033634. arXiv: arXiv:1106.5958v2.

[10] K. Huang. *Statistical mechanics*. Wiley, 1987. ISBN: 9780471815181.

[11] D. S. Petrov, C. Salomon, and G. V. Shlyapnikov. "Scattering properties of weakly bound dimers of fermionic atoms". In: *Physical Review A - Atomic, Molecular, and Optical Physics* 71.1 (2005), pp. 1–15. ISSN: 10502947. DOI: 10.1103/PhysRevA.71.012708. arXiv: 0309010 [cond-mat].

[12] Neil W Ashcroft and N David Mermin. "Solid State Physics (Saunders College, Philadelphia, 1976)". In: *Appendix N* (2010).

[13] B. A. Lippmann and Julian Schwinger. "Variational Principles for Scattering Processes. I". In: *Phys. Rev.* 79 (3 Aug. 1950), pp. 469–480. DOI: 10.1103/PhysRev.79.469. URL: http://link.aps.org/doi/10.1103/PhysRev.79.469.

[14] L.I. Schiff. *Quantum Mechanics*. International series in pure and applied physics. McGraw-Hill, 1993.

[15] Claude Cohen-Tannoudji and David Guéry-Odelin. *Advances in atomic physics: an overview*. World Scientific, 2011.

[16] C.J. Joachain. *Quantum Collision Theory*. North-Holland Publishing Company, 1979. ISBN: 9780444852359.

[17] R. E. Drullinger, D. J. Wineland, and J. C. Bergquist. "High-resolution optical spectra of laser cooled ions". In: *Applied Physics* 22 (1980), pp. 365–368. ISSN: 03403793. DOI: 10.1007/BF00901058.

[18] Wilhelm Zwerger. *The BCS-BEC crossover and the unitary Fermi gas. Lecture Notes in Physics 836*. Springer Science, Business Media, 2011.

[19] Mohit Randeria. "Ultracold Fermi gases: Pre-pairing for condensation". In: *Nature Physics* 6.8 (2010), pp. 561–562. ISSN: 1745-2473. DOI: 10.1038/nphys1748. URL: http://dx.doi.org/10.1038/nphys1748.

[20] Wolfgang Ketterle and Martin W. Zwierlein. "Making, probing and understanding ultracold Fermi gases". In: June 2006 (Jan. 2008), p. 206. DOI: 10.1393/ncr/i2008-10033-1. arXiv: 0801.2500. URL: http://arxiv.org/abs/0801.2500.

[21] Karl-Heinz Bennemann and John B Ketterson. *Novel superfluids*. Vol. 1. Oxford University Press, 2013.

[22] Eric Braaten. "Universal Relations for Fermions with Large Scattering Length arXiv : 1008 . 2922v1 | cond-mat . quant-gas | 17 Aug 2010". In: (), pp. 1–43. arXiv: arXiv:1008.2922v1.

[23] Lawrence Berkeley and Berkeley Ca. "epl draft Doping evolution of superconducting gaps and electronic densities arXiv : 1007 . 2218v1 | cond-mat . supr-con | 13 Jul 2010". In: 06 (), pp. 1–7. arXiv: arXiv:1007.2218v1.

[24] Sylvain Nascimbène. "Thermodynamique des gaz de fermions ultrafroids Thermodynamics of ultracold Fermi gases, PhD thesis". In: (2010).

[25] Lev Davidovich Landau and EM Lifshitz. *Statistical Physics. Part 1: Course of Theoretical Physics*. 1980.

[26] Vamsi K. Akkineni, D. M. Ceperley, and Nandini Trivedi. "Pairing and superfluid properties of dilute fermion gases at unitarity". In: *Physical Review B - Condensed Matter and Materials Physics* 76 (2007), pp. 1–6. ISSN: 10980121. DOI: 10.1103/PhysRevB.76.165116. arXiv: 0608154 [cond-mat].

[27] Xia Ji Liu. "Virial expansion for a strongly correlated Fermi system and its application to ultracold atomic Fermi gases". In: *Physics Reports* 524 (2013), pp. 37–83. ISSN: 03701573. DOI: 10.1016/j.physrep.2012.10.004. arXiv: 1210.2176.

[28] Xia-Ji Liu, Hui Hu, and Peter Drummond. "Virial Expansion for a Strongly Correlated Fermi Gas". In: *Physical Review Letters* 102.April (2009), pp. 1–4. ISSN: 0031-9007. DOI: 10.1103/PhysRevLett.102.160401. URL: http://link.aps.org/doi/10.1103/PhysRevLett.102.160401.

[29] R. K. Bhaduri, W. Van Dijk, and M. V N Murthy. "Higher virial coefficients of a unitary Fermi gas". In: *Physical Review A - Atomic, Molecular, and Optical Physics* 88 (2013), pp. 4–6. ISSN: 10502947. DOI: 10.1103/PhysRevA.88.045602. arXiv: 1310.4726.

[30] Tin-Lun Ho and Qi Zhou. "Obtaining phase diagram and thermodynamic quantities of bulk systems from the densities of trapped gases". In: *Nature Physics* 6.2 (2008), pp. 131–134. ISSN: 1745-2473. DOI: 10.1038/nphys1477. arXiv: 0901.0018. URL: http://arxiv.org/abs/0901.0018.

[31] Sandro Stringari Lev Pitaevskii. *Bose-Einstein Condensation*. Clerendon press, Oxford, 2003.

[32] N.H. Abel. "Auflösung einer mechanischen Aufgabe." ger. In: *Journal für die reine und angewandte Mathematik* 1 (1826), pp. 153–157. URL: http://eudml.org/doc/183021.

[33] Cameron J. Dasch. "One-dimensional tomography: a comparison of Abel, onion-peeling, and filtered backprojection methods". In: *Appl. Opt.* 31.8 (Mar. 1992), pp. 1146–1152. DOI: 10.1364/AO.31.001146. URL: http://ao.osa.org/abstract.cfm?URI=ao-31-8-1146.

[34] Shuiliang Ma, Hongming Gao, and Lin Wu. "Modified Fourier-Hankel method based on analysis of errors in Abel inversion using Fourier transform techniques". In: *Applied Optics* 47.9 (Mar. 2008), p. 1350. ISSN: 0003-6935. DOI: 10.1364/AO.47.001350. URL: http://www.opticsinfobase.org/abstract.cfm?URI=ao-47-9-1350.

[35] Vladimir Dribinski et al. "Reconstruction of Abel-transformable images: The Gaussian basis-set expansion Abel transform method". In: *Review of Scientific Instruments* 73.7 (2002), p. 2634. ISSN: 00346748. DOI: 10.1063/1.1482156. URL: http://scitation.aip.org/content/aip/journal/rsi/73/7/10.1063/1.1482156.

[36] N Navon et al. "The equation of state of a low-temperature Fermi gas with tunable interactions." In: *Science (New York, N.Y.)* 328.5979 (2010), pp. 729–732. ISSN: 0036-8075. DOI: 10.1126/science.1187582. arXiv: 1004.1465.

[37] A Burchianti et al. "Efficient all-optical production of large 6-Li quantum gases using D1 gray-molasses cooling". In: *ArXiv e-prints* (2014), p. 5. ISSN: 10941622. DOI: 10.1103/PhysRevA.90.043408. arXiv: 1406.4788 [cond-mat.quant-gas]. URL: http://arxiv.org/abs/1406.4788.

[38] Harold J Metcalf and Peter Van der Straten. *Laser cooling and trapping*. Springer Science & Business Media, 1999.

[39] Massimo Inguscio and Leonardo Fallani. *Atomic physics: precise measurements and ultracold matter*. Oxford University Press, 2013.

[40] G. Zürn et al. "Precise characterization of Li6 Feshbach resonances using trap-sideband-resolved RF spectroscopy of weakly bound molecules". In: *Physical Review Letters* 110.13 (2013), pp. 1–5. ISSN: 00319007. DOI: 10.1103/PhysRevLett.110.135301. arXiv: arXiv:1211.1512v2.

[41] Ariel T Sommer. "Strongly Interacting Fermi Gases : Non-Equilibrium Dynamics and Dimensional Crossover, PhD thesis". In: (2013).

[42] Max Born and Emil Wolf. *Principles of optics: electromagnetic theory of propagation, interference and diffraction of light*. Cambridge university press, 1999.

[43] Morales Andrea. "High resolution imaging and production of thin barriers for ultra cold 6Li Fermi gases, master thesis". In: (2013).

[44] G Reinaudi et al. "Strong saturation absorption imaging of dense clouds of ultracold atoms." In: *Optics letters* 32.21 (2007), pp. 3143–3145. ISSN: 0146-9592. DOI: 10.1364/OL.32.003143. arXiv: 0707.2930.

[45] Alexander L Fetter and John Dirk Walecka. *Quantum theory of many-particle systems*. Courier Corporation, 2003.

[46] Erich Beth and George E Uhlenbeck. "The quantum theory of the non-ideal gas. II. Behaviour at low temperatures". In: *Physica* 4.10 (1937), pp. 915–924.

[47] Michael Tinkham. *Introduction to superconductivity*. Courier Corporation, 2012.

[48] Evgeni Burovski et al. "Critical temperature and thermodynamics of attractive fermions at unitarity". In: *Physical Review Letters* 96.16 (2006), pp. 1–4. ISSN: 00319007. DOI: 10.1103/PhysRevLett.96.160402. arXiv: 0602224 [cond-mat].

[49] Sylvain Nascimbène et al. "The equation of state of ultracold Bose and Fermi gases: A few examples". In: *New Journal of Physics* 12 (2010). ISSN: 13672630. DOI: 10.1088/1367-2630/12/10/103026. arXiv: 1006.4052.

[50] Víctor Romero-Rochín. "Equation of state of an interacting bose gas confined by a harmonic trap: The role of the "harmonic" pressure". In: *Physical Review Letters* 94.13 (2005), pp. 8–11. ISSN: 00319007. DOI: 10.1103/PhysRevLett.94.130601.

[51] R F Shiozaki et al. "Measuring The Heat Capacity in a Bose-Einstein Condensation using Global Variables". In: 043640 (2014), p. 9. ISSN: 10941622. DOI: 10.1103/PhysRevA.90.043640. arXiv: 1408.5852. URL: http://arxiv.org/abs/1408.5852.

[52] Karsten Ahnert and Markus Abel. "Numerical differentiation of experimental data: local versus global methods". In: *Computer Physics Communications* 177.10 (Nov. 2007), pp. 764–774. ISSN: 00104655. DOI: 10.1016/j.cpc.2007.03.009. URL: http://linkinghub.elsevier.com/retrieve/pii/S0010465507003116.